

**THERMOELECTRIC PROPERTIES OF
DYSPROSIUM INCORPORATED ZnO
MATERIALS**

Thesis submitted to the University of Calicut
in partial fulfillment of the requirements for the award of the Degree of

Doctor of Philosophy in Physics

Under the Faculty of Science

by

ANJU PAULSON



Under the guidance of
Dr. P.P.Pradyumnan
Professor

**DEPARTMENT OF PHYSICS
UNIVERSITY OF CALICUT
KERALA 673635-INDIA**

October 2019

DEPARTMENT OF PHYSICS
UNIVERSITY OF CALICUT
KERALA 673635 - INDIA

Dr.P.P.PRADYUMNAN
Professor



Grams: UNICAL
91-494-2401144,415,416
e-mail: drpradyumnan@gmail.com
Kerala-673635; India.

CERTIFICATION OF SUPERVISOR

This is to certify that all the corrections/suggestions from the adjudicators have been incorporated in this thesis.

Calicut University
June 2020

Dr. P.P.Pradyumnan

DEPARTMENT OF PHYSICS
UNIVERSITY OF CALICUT
KERALA 673635 - INDIA

Dr.P.P.PRADYUMNAN
Professor



Grams: UNICAL
91-494-2401144,415,416
e-mail: drpradyumnan@gmail.com
Kerala-673635; India.

CERTIFICATE

Certified that the work presented in this thesis entitled “**Thermoelectric Properties of Dysprosium Incorporated ZnO Materials**” is submitted to the University of Calicut in partial fulfillment of the requirements for the award of degree of Doctor of Philosophy in Physics is a record of original research work done by **Ms. ANJU PAULSON** during the period 2016 - 2019 under my guidance in the Department of Physics, University of Calicut. The thesis has not formed the basis for the award of any Degree/Diploma and has undergone plagiarism check using URKUND software at CHMK Library, University of Calicut and the similarity index is found within the permissible limit.

Calicut University
October 2019

Dr. P.P.Pradyumnan

DECLARATION

I, ANJU PAULSON, hereby declared that this thesis work entitled “**Thermoelectric Properties of Dysprosium Incorporated ZnO Materials**” submitted to the Department of Physics, University of Calicut is a record of the original work done by me under the guidance of Dr. P.P. Pradyumnan, Professor, Department of Physics, University of Calicut and this work has not been included in any other thesis submitted previously for the award of any degree.

Date:

ANJU PAULSON

ACKNOWLEDGEMENT

I owe my profound gratitude to great many people who help and support me during this research work to make this thesis possible.

I deeply indebted to my supervising guide Dr. P.P.Pradyumnan, Professor, Department of Physics, University of Calicut, who took keen interest on my research work and guided me all along, till the completion of my work by providing all the necessary information for achieving a good result. His dedication and hard work to research always became a pathfinder for me during my research. He gave immense freedom in my work, willing to hear me and acknowledge my sincere efforts. I deeply acknowledge the inspiration and support that he provided to me during my tough times and during the critical reading of the thesis.

I would like to extend my sincere thanks to Dr.A.M Vinodkumar, Head of the department of Physics and all the former HODs include Dr.Antony Joseph,Dr M.M Musthafa for providing the facilities in the department to carry out my research work. With pleasure I thank all the faculty members especially Dr. Libu K Alexander for his critical advice and the friendly talks that we made during this research period. Thanks to Dr. Shahin Thayil and Dr.C.D. Ravikumar for their support during this research period. Thanks to all non-teaching staffs of the Department of Physics for their help throughout the course of this work.

I deeply acknowledge KSCSTE for the financial assistance they provide in the form of JRF and SRF research fellowship. I also acknowledge DST SERB, Govt of India for the financial assistance in the form of major research project entitled “Studies on oxide materials for thermoelectric generation” (No.SB/EMEQ 002/2013 dated 5/7/2013).

Words are insufficient to express my gratitude to Muhammed Sabeer N.A

and Jummanath E.C for their constant help, support and guidance throughout the entire course of my research work. I deeply acknowledge the generous and whole hearted help that they provide me during this entire research period.

I acknowledge my gratitude to my seniors, especially Mrs.Jaya, Mrs. Divya, Mrs.Soumya, Mrs Vidya and Mrs Shabeeba for their valuable advice and motivation. I deeply acknowledge my co researches Nabeela, Vineetha teacher, Shyni teacher, Parvathy and Midhun Sha for their support that they provide during my research work. I acknowledge Vineetha teacher and Nabeela for thier mental support that they provide me during my tough times. Thanks to all research scholars in the Department of Physics for their valuable advice and support that they provide during the entire course of my research work. Great thanks to my loving parents papa and mummy, my younger brothers Aji and Ajo, Appachan and amma and all well wishers for their inspiration, whole hearted support and prayers. Great thanks to my husband Eljo Francis P for his motivation and inspiration provided to me during my work. He was always eager to hear me and provide a constant support during my tough times and during the writing of my thesis.

I humbly bow my head before ‘The Almighty God’ for blessing me to complete this venture.

ANJU PAULSON

**Dedicated to
My
Parents**

PREFACE

The increased demand for new energy resources and the existing environmental problems forced the scientists and researchers to explore for environment-friendly non conventional energy sources for power generation. Thermoelectric power generators offer a promising green technology through waste heat recovery which can be treated as one of the best ways to solve energy problems. Waste heat energy can be utilized for power generation by means of thermoelectric materials which are capable of converting thermal energy to electricity. Since the conventional thermoelectric generators possess abundant toxicity and can be applied at low temperature, the search for new novel thermal electric generators lead to oxide materials with high temperature compatibility and chemical stability. Thermoelectric materials are solid state devices which convert heat directly into electrical energy with electrons as the working fluid. It has no moving components and doesn't emit greenhouse gases.

The thesis entitled "Thermoelectric Properties of Dysprosium Incorporated ZnO Materials" presents a detailed study on the structural and thermoelectric properties of Dysprosium incorporated ZnO bulk microstructures, nanomaterials and thin films. The thesis is divided into seven chapters,

Chapter 1 presents a general introduction to thermoelectricity and thermoelectric materials. The basic properties of TE materials, motivation and objectives of the present work is to be included. The objectives include the synthesis of TE materials and the method to enhance the efficiency. It briefly explains the thermoelectric effects, efficiency parameters and the way by which TE efficiency can be improved. It also put forward the strategies and criteria for the fabrication of suitable TE materials. Doping, nanostructuring, band filling and band renormalization were also discussed to improve the TE efficiency.

Chapter 2 enclose the material processing and the characterisation techniques

used in this study. The experimental procedure to synthesis bulk polycrystalline, nanomaterials and thin films were clearly explained. The synthesis condition by solid state reaction and hydrothermal methods were depicted. The deposition parameters for fabricating thin films using radio frequency magnetron sputtering was also mentioned. A brief description regarding the characterisation techniques used to study the structural, morphological, compositional and TE properties were also mentioned.

Chapter 3 deals with the microstructures for thermoelectric application. It includes the synthesis of a series of bulk polycrystalline pellets of nominal composition $\text{Zn}_{1-x}\text{Dy}_x\text{O}$ at high temperature using the solid state reaction mechanism. Structural characterisation was performed using XRD and Raman analysis. The XRD confirms the synthesis samples are phase pure and the structural integrity was ensured. The solubility limit of Dy ions in the ZnO host lattice through doping was also obtained. Morphological and compositional analysis were performed using the SEM and EDAX analysis. The electronic properties such as carrier concentration, mobility, conductivity was measured using the Hall measurement at room temperature. Optical band gap analysis ensured the widening of the band gap and the doped samples are found to be degenerate semiconductors. Dy incorporation enhance the TE efficiency and the doping can be considered as a good criteria for TE enhancement.

Chapter 4 discuss the introduction of nanostructures in thermoelectric materials. Nanomaterials were fabricated using hydrothermal synthesis mechanism with Zinc acetate, Dysprosium chloride (DyCl_3) and KOH as the initial precursors. Structural and morphological studies ensured the grown crystallites possess hexagonal symmetry and their grain boundaries are in nano regime. Compositional analysis using energy dispersive X-ray spectroscopy (EDAX) ensured the presence of Dy ions in the matrix. Electronic measurements using Hall analysis ensured the increment in carrier concentration

and mobility. Porosity analysis using the Barrer-Joyner-Halenda (BJH) techniques ensured the presence of inhomogeneous pores in the medium. Thermoelectric properties were determined and the reduction in thermal conductivity for the nanostructured samples were confirmed. Thus doping along with nanostructuring imparts to be a good method for TE enhancement.

Chapter 5 discuss the fabrication of TE materials using RF magnetron sputtering. Along with the enhancement in TE efficiency, its transparent conducting properties where also analyzed. Thus multifunctionality of the Dy doped ZnO thin films were studied. Sputtering conditions were optimized and the Dy doped ZnO home made targets were used as sputtering cathode. XRD confirms the orientation of planes in the lattice. SEM micrographs ensured the presence of strain energy with the reduction in crystallite size. AFM analysis determines the roughness of the coated samples. Core level XPS spectra calibrated by C 1s provides the important information regarding the composition and oxidation state of the elements present. Dy substitution in ZnO enhance the opto-electrical characteristics and was confirmed using UV and Hall measurement. A large increase in carrier concentration lead to the non parabolicity in band structure and causes deterioration in mobility due to heavier effective mass. Solution to this problem was discussed in chapter 6.

Chapter 6 mention the decoupling of contradicting parameters such as effective mass and mobility by reconstructing the band structure. The band gets renormalized due to band filling by the carriers with concentration greater than critical value called the Mott's limit. Ga and Dy doped ZnO thin films were fabricated using the RF magnetron sputtering with the optimized sputtering conditions. XRD analysis confirmed the preferred orientation along c axis due to the strain energy. Hall measurement substantiates the increase in carrier concentration above the Mott's critical limit. It also ensured that even though the carrier concentration increases it doesn't drastically decrease the mobility of the charge carriers. Thus electrical conductivity get preserved

in the the sample. UV band gap analysis confirmed the reconstruction of valence and conduction band. TE properties of the samples were also studied.

Final chapter provides a general conclusion and scope for future research work. It comprise of summarized results from the research work and it conclude that strategies such as doping, nanostructuring along with quantum confinement arose as a good criteria for fabricating TE materials. Renormalization of bands should be done to decouple the effective mass and mobility of charge carriers to an extent. The results obtained from this research depicts that the objectives are satisfactorily obtained and experimentally confirmed. Future studies include temperature dependent Hall measurements, fabrication of TE modules for device application and the determination of spin Seebeck measurements for the enhancement of TE efficiency.

Abbreviations

- * AFM: Atomic Force Microscopy
- * DOS: Density of States
- * EDAX : Energy dispersive X-ray spectroscopy
- * ICDD: International Centre for Diffraction Data
- * LTC: Lattice Thermal Conductivity
- * RF:Radio Frequency
- * SEM: Scanning Electron microscope
- * SSR: Solid State Reaction
- * TE: Thermoelectricity
- * UV-DRS:Ultra Violet Diffuse Reflectance Spectroscopy
- * XRD: X-ray Diffraction
- * XPS : X-ray Photoelectron Spectroscopy

Journal Publications

1. **Anju Paulson**, Muhammed Sabeer, N. A. & Pradyumnan, P. P.
A synergetic approach of band gap engineering and reduced lattice thermal conductivity for the enhanced thermoelectric property in Dy ion doped ZnO. *J. Alloys Compd.* 786 (2019) 581-587.
2. **Anju Paulson**, N.A.M. Sabeer, P.P.Pradyumnan, Enhanced thermoelectric property of Oxygen deficient nickel doped SnO₂ for high temperature thermoelectric application, *Mater. Res. Express* 5 (2018) 045511.
3. P.P. Pradyumnan, **A. Paulson**, N.A. Muhammed Sabeer, N. Deepthy, Enhanced power factor in Ho³⁺ doped ZnO: A new material for TE application, *AIP Conf. Proc.* 1832 (2017) 110055.
4. N.A.M. Sabeer, **A. Paulson**, P.P. Pradyumnan, Doubling the thermoelectric power factor of earth abundant tin nitride thin films through tuned (311) orientation by magnetron sputtering, *J. Appl. Phys.* 124 (2018).
5. P.Maneesha, **Anju Paulson**, N.A Muhammed Sabeer, P.P.Pradyumnan, Thermoelectric measurement of nano crystalline Cobalt doped Copper sulphide for energy generation, *Materials Letters* 225 (2018) 57–61.
6. Muhammed Sabeer N.A, **Anju Paulson**, P.P.Pradyumnan, An experimental approach of decoupling Seebeck coefficient and electrical resistivity, *AIP Conf. Proc.* 1942 (2018) 110054 .

Journal Paper Communicated

1. Anju Paulson, Muhammed Sabeer, N. A. & Pradyumnan, P. P;
Enhancement of optical and thermoelectric properties in Dysprosium doped ZnO thin films as an impact of non-parabolic band structure(Under review).

Important Scientific events participated

1. International Conference on Optoelectronic and Nano Materials for Advanced Technology (iCONMAT 2019) during 3-5th January 2019 held at Cochin University of Science and Technology, Kochi.
2. Attended INUP, Hands on training programme on Nano fabrication techniques at IISC Bangalore during 3rd-13th April 2018.
3. 30th Kerala Science Congress held at Govt. Brennen College Thaleserry during 28- 30th January 2018.
4. International conference on Thin Films (ICTF) held at CSIR-National Physical Laboratory New Delhi during 14 to 17th November 2017.
5. National Symposium on Nano Science & Technology (NSNST 2017) conducted by Centre for Nano Science and Engineering, IISC Bangalore during 2nd to 4th July 2017.
6. National seminar on recent advancements in Photonics (NSAP) held at Vimala College, Thrissur during 13th to 15th February 2017.
7. 61st Solid state symposium conducted by UGC DAE at KIIT University, Bhubaneswar, Orissa on 26 -30th December 2016.
8. Second International conference on Material Science and Technology (ICMST) held at Pala, ST. Thomas College on 5 -8th June 2016.

Awards

- * Best oral presentation in ICMST held at Pala, ST. Thomas College on 5-8th June 2016 on 'Effect of sintering temperature on the enhancement of thermoelectric properties of Ni doped SnO₂'.
- * Best oral presentation in NSAP held at Vimala College, Thrissur during 13th to 15th February 2017 on 'Enhanced Power factor in Ho³⁺ doped ZnO for thermoelectric application'.

Contents

1	Introduction to Thermoelectricity	1
1.1	Introduction	1
1.2	Thermoelectric effects	2
1.2.1	Seebeck effect	3
1.2.2	Peltier effect	6
1.2.3	Thomson effect	6
1.3	Efficiency of thermoelectric material	8
1.3.1	Thermal conductivity	11
1.3.2	Electrical conductivity	13
1.4	Transport effects in metals and semiconductors	16
1.5	Thermoelectric properties in metals and semiconductors	19
1.6	Strategies and criteria for the enhancement of figure of merit .	20
1.7	Thermoelectric materials	23
1.7.1	Skutterudites	24
1.7.2	Clathrates	25
1.7.3	Silicides	26
1.7.4	Half-Heussler compounds	26
1.7.5	Oxides	26
1.8	Zinc oxide (ZnO)	28
1.8.1	Thermoelectric properties of pure ZnO	28
1.8.2	Thermoelectric properties of non-stoichiometric and doped ZnO	29

1.9	Motivation and Objectives	30
	References	31
2	Experimental Techniques and Characterization Tools	36
2.1	Introduction	37
2.2	Solid state reaction (SSR)	37
2.2.1	Mixing of raw materials	38
2.2.2	Calcination	38
2.2.3	Grinding and pelletization	39
2.2.4	Sintering	40
2.3	Hydrothermal synthesis	40
2.3.1	Design aspects of an autoclave	41
2.3.2	Synthesis mechanism	41
2.3.3	Advantages of hydrothermal synthesis	42
2.4	Sputtering	42
2.4.1	RF magnetron sputtering	43
2.5	Structural characterization	46
2.5.1	X-Ray diffraction	46
2.5.2	Raman spectroscopy	49
2.6	Morphological analysis	52
2.6.1	Scanning electron microscopy	52
2.6.2	Atomic force microscopy	54
2.7	Chemical analysis	57
2.7.1	X-ray photoelectron spectroscopy (XPS)	57
2.7.2	Energy dispersive X-ray spectroscopy (EDAX)	58
2.8	Optical spectroscopy	59
2.8.1	UV-Visible spectroscopy	59
2.9	Electronic property	62
2.9.1	Hall measurement	62
2.10	Thermoelectric properties	65
2.10.1	Electrical conductivity and Seebeck coefficient	65
2.10.2	Thermal conductivity measurement	67

References	69
3 Thermoelectric Property of	
Dy ion Doped ZnO Microstructures	72
3.1 Introduction	73
3.2 Synthesis of microstructures	75
3.3 Results and discussion	75
3.3.1 XRD analysis	75
3.3.2 Raman analysis	78
3.3.3 Morphological analysis	81
3.3.4 Optical studies	81
3.3.5 Electrical properties	83
3.3.6 Thermoelectric properties	85
3.3.7 Figure of merit	91
3.4 Conclusions	92
References	94
4 Nanomaterials for Thermoelectricity	96
4.1 Introduction	97
4.2 Synthesis of nanomaterials	99
4.3 Results and discussion	100
4.3.1 XRD analysis	100
4.3.2 Raman analysis	101
4.3.3 Morphological analysis	104
4.3.4 Optical studies	104
4.3.5 Electrical properties	106
4.3.6 Porosity analysis	108
4.3.7 Thermoelectric properties	110
4.3.8 Figure of merit	115
4.4 Conclusions	115
References	117

5	Studies on Dy Doped ZnO Thin Films for Thermoelectric Application	119
5.1	Introduction	120
5.2	Thin film fabrication	122
5.3	Results and discussion	123
5.3.1	XPS analysis	123
5.3.2	EDAX analysis	126
5.3.3	XRD analysis	127
5.3.4	SEM analysis	129
5.3.5	AFM analysis	132
5.3.6	Optical properties	133
5.3.7	Electrical properties	137
5.3.8	Thermoelectric measurement	138
5.4	Conclusions	140
	References	142
6	Studies on Dual Doped (Dy,Ga) ZnO for Thermoelectric Applications	146
6.1	Introduction	147
6.2	Thin film fabrication	148
6.3	Results and discussion	150
6.3.1	EDAX analysis	150
6.3.2	XRD analysis	151
6.3.3	SEM analysis	152
6.3.4	AFM analysis	154
6.3.5	Optical properties	155
6.3.6	Electrical properties	157
6.3.7	Thermoelectric properties	159
6.4	Conclusions	161
	References	166

7	General conclusion and Future scope	168
7.1	Summary of the thesis	168
7.1.1	Doping	169
7.1.2	Nanostructuring and Quantum confinement effect . . .	170
7.2	Future scopes	173

List of Figures

1.1	Representation of Seebeck effect.	4
1.2	Fermi distribution at the hot and cold end [13].	5
1.3	Demonstration of Peltier effect.	6
1.4	Demonstration of Thomson effect [17].	7
1.5	Thermoelectric Module [19].	8
1.6	Dependence of carrier concentration on thermoelectric parameters [21].	10
1.7	Variation of lattice thermal conductivity with temperature due to different scattering mechanism [25].	12
1.8	Thermal conductivity in materials [26].	13
1.9	Energy band diagram for a)metal, b)insulator, c)semiconductor, d)semimetal [28].	14
1.10	Energy band diagram of a doped semiconductor [29].	16
1.11	Density of states for different dimensions [32].	21
1.12	General representation of MX_3 [37]	25
1.13	Crystal structure of type-I clathrate compounds with general formula $\text{A}_x\text{B}_y\text{C}_{46-y}$ [39].	25
1.14	Crystal structure of NaCo_2O_4 [44].	28
1.15	Wurtzite structure of ZnO [50].	29
2.1	Dye and pelletizer for fabricating circular pellets.	39
2.2	Schematic representation of sputtering system.	43
2.3	Schematic representation of X-ray Diffraction [7].	47

2.4	X-Ray Diffractometer: Rigaku Miniflex 600 with Bragg-Brentano geometry.	49
2.5	Schematic representation of Raman scattering.	51
2.6	Schematic representation of SEM instrument [13].	53
2.7	Emission of various electron and electromagnetic waves from the specimen [13].	54
2.8	Schematic representation of the photoelectron emission.	58
2.9	Schematic representation of EDAX analysis.	59
2.10	Cross sectional diagram of a powder layer.	60
2.11	Illustration of Hall effect.	63
2.12	Hall voltage measurement using van der Pauw configuration.	63
2.13	Thermoelectric measurement system ULVAC ZEM-3 M8.	65
2.14	Schematic representation of measurement in ULVAC-ZEM 3 M8 system.	66
2.15	Schematic representation of divided bar method to determine the thermal conductivity.	68
2.16	Temperature Vs distance from the heating end.	68
3.1	XRD pattern corresponding to pure and Dy doped ZnO.	76
3.2	Shift observed for the peak corresponding to (101) plane.	77
3.3	Raman spectra for the pure and Dy doped ZnO.	79
3.4	Raman spectrum representing the A_1 and E_1 LO modes.	80
3.5	SEM and EDAX corresponding to pure and Dy doped ZnO.	83
3.6	Kubelka Munk function Vs $h\nu$ for pure and Dy doped ZnO.	84
3.7	Variation of electrical conductivity with temperature for pure and Dy doped ZnO.	86
3.8	Variation of Seebeck coefficient with temperature for the pure and Dy doped ZnO.	89
3.9	Variation in power factor with temperature for pure and Dy doped ZnO.	90
3.10	Variation of thermal conductivity with temperature for pure and Dy doped ZnO.	91

3.11	Variation of ZT value with temperature for pure and Dy doped ZnO.	92
4.1	The XRD patterns corresponding to Dy doped ZnO samples.	101
4.2	Room temperature micro Raman spectra for Dy doped ZnO samples.	103
4.3	SEM and EDAX corresponding to different Dy concentration in ZnO.	106
4.4	Kubelka Munk function Vs $h\nu$ for different Dy concentration in ZnO.	107
4.5	BJH pore size distribution.	111
4.6	Variation of Seebeck coefficient with temperature for Dy doped ZnO samples.	112
4.7	Variation of electrical conductivity for the Dy doped ZnO samples.	113
4.8	Variation of power factor with temperature for Dy doped ZnO samples.	114
4.9	Variation of thermal conductivity with temperature for Dy doped ZnO samples.	115
4.10	Variation of ZT with temperature for Dy doped ZnO samples.	116
5.1	XPS full scan spectrum of F ₄ sample.	124
5.2	Deconvoluted XPS peak corresponding to Zn 2p for the F ₄ sample.	126
5.3	XPS spectrum corresponding to O 1s peak for a) F ₁ b) F ₄ sample.	126
5.4	XPS spectrum of 4d _{5/2} peak corresponding to F ₄ sample.	127
5.5	XRD pattern for the pure and Dy doped ZnO.	129
5.6	Shift observed for the peak corresponding to (002) plane.	130
5.7	SEM micrographs of a) F ₁ , b) F ₂ , c) F ₃ , d) F ₄	131
5.8	3D AFM images of a) F ₁ , b) F ₂ , c) F ₃ , d) F ₄ sample.	133
5.9	Transmission spectrum for Dy doped ZnO thin films.	134

5.10	Variation of optical band gap for Dy doped ZnO thin films. . .	135
5.11	Variation of Seebeck coefficient with temperature for Dy doped ZnO.	139
5.12	Variation of electrical conductivity with temperature for Dy doped ZnO.	140
5.13	Variation of power factor with temperature for Dy doped ZnO.	141
6.1	X-ray diffraction corresponding to dual doped ZnO thin films.	152
6.2	X-ray diffraction corresponding to dual doped ZnO thin films.	153
6.3	Shift in (002) plane for the dual doped ZnO thin films.	154
6.4	SEM micrographs corresponding to pure and Dy doped ZnO samples.	155
6.5	SEM micrographs corresponding to Dy and Ga doped ZnO samples.	156
6.6	AFM 3D images of the pure and Dy doped ZnO thin films. . .	157
6.7	AFM 3D images of the dual doped ZnO thin films.	159
6.8	Transmittance spectrum of dual doped ZnO.	160
6.9	Band gap energy for the pure and Dy doped ZnO.	161
6.10	Band gap energy for the dual doped ZnO samples.	162
6.11	Variation of Seebeck coefficient with temperature for the dual doped ZnO.	163
6.12	Variation of Electrical conductivity with temperature for the dual doped ZnO.	164
6.13	Variation of thermoelectric power factor with temperature for the dual doped ZnO.	165

List of Tables

3.1	The crystallite size and micro strain corresponding to (101) plane with varying the Dy concentration in ZnO	78
3.2	Variation of electrical characteristics for pure and Dy doped ZnO	84
3.3	Difference in Fermi energy with the conduction band edge . . .	88
4.1	Variation of crystallite size and lattice parameters for different Dy concentration	102
4.2	Raman vibrational frequency for different symmetry elements	102
4.3	Bandgap energy for different Dy concentration in ZnO	105
4.4	Electrical characteristics of Dy doped ZnO samples	107
4.5	Surface parameter for Dy doped ZnO samples	110
5.1	Optimized deposition parameters for pure and doped ZnO thin films	123
5.2	Data obtained from XPS spectrum for the F ₄ sample	125
5.3	Deconvoluted peak position corresponding to Zn, O and Dy . .	125
5.4	Elemental composition for Dy doped ZnO	128
5.5	Determination of particle size and roughness of the coated thin film	132
5.6	Electrical properties for different Dy concentration in ZnO . .	137
6.1	Optimized deposition parameters for the RF sputtering	149
6.2	Elemental composition for Dy and Ga doped ZnO	150

6.3	Variation of lattice parameter and strain in the lattice by dual doping in ZnO thin films	153
6.4	Determination of particle size and roughness of the coated thin film	155
6.5	Electrical properties for different Dy and Ga concentration . .	158

Chapter 1

Introduction to Thermoelectricity

Objectives

The objective of this chapter is to introduce the basic idea behind thermoelectricity and thermoelectric materials. Criteria and strategies for the optimization of thermoelectric figure of merit was also discussed.

1.1 Introduction

Harnessing energy for the use of mankind in an ever increasing rate is one of the world's biggest need. The quest for energy and energy resources had a long past from the time of evolution of man kind. Civilization had historically came around energy sources that are sufficient for finite energy production. Global energy consumption demand for new energy sources for power generation due to its increase over the years and it was reported that it continue to increase by 30 - 40 % in next 20 years [1]. Diminishing of fossil fuel sources always become a major problem to overcome, even though alternative energy sources such as nuclear, geothermal etc provide solution to this [2]. However, in most cases the major part of the produced energy is lost in the form of waste heat. This heat energy can be either used directly in a process or can be converted to useful mechanical based thermodynamic process. An efficient way of utilizing this heat energy is by the use of solid state energy converter [3].

Thermoelectric (TE) materials are solid state energy converters, which are capable of converting a thermal gradient into electric energy by using electrons/holes as working fluid. They are compact, responsive and feasible for miniaturization with out the requirement of any moving components or green house gas emission [4]. They are capable of direct and efficient conversion of abundant solar and geothermal heat [5]. However, the development in the field of thermoelectricity requires effective, sustainable and cost efficient materials. TE power generators are particularly used for deep space application where solar energy is inadequate to control the power generation. The temperature gradient between the heat produced by the radioisotope decay and the temperature of the outer space provide enough temperature gradient to power the space station [6]. The automotive application of a TE generator is limited by its smaller temperature gradient. The best known TE materials belongs to Bi_2Te_3 family which have the low thermal stability($T_{max} = 586^\circ\text{C}$) and a maximum TE performance at 150°C [7]. The scarcity of Te in earth's crust and their toxicity become a major problem for

large scale production. The search for novel TE materials with high thermal stability ($T_{max} > 650^{\circ}C$) and durability is in progress. The materials that are known to fulfill such requirements include skutterides, clathrates, silicides, half Heusler compounds, oxides and other non oxide materials. Among these, the class of material oxides are one of the most promising TE material due to their chemical and thermal stability in air at high temperature and they are regarded as a suitable candidates for high temperature thermoelectric applications.

Thermoelectric conversion devices are not able to replace the current primary power generation system. However, they can provide supplemental conversion to improve the efficiency of the overall system. The low conversion efficiency of thermoelectric material become a major challenge among the material researches for its implementation for power generation. In this scenario, the thesis focused on the enhancement of TE efficiency of ZnO oxide materials through the following methods,

1. Doping: Synergistic approach of optimization of semiconducting band edge (by the introduction of donor/acceptor ions) and modulating lattice thermal conductivity.
2. Nanostructuring: Presence of nano grain boundaries and inhomogeneous pores in the nanostructure lead to the increased phonon scattering and reduced thermal conductivity.
3. Quantum confinement: Nanostructured thin films have enhanced density of states and thereby cause improvement in thermopower and TE efficiency.

1.2 Thermoelectric effects

Electrons which are the elementary particle in a solid under thermal equilibrium able to carry heat and entropy from hotter side to colder region as a

result of temperature gradient. This caused for the development of electric current. The interplay between the thermal and electrical counterparts pay the way to certain thermoelectric effects.

1.2.1 Seebeck effect

In 1821 Thomas Johannan Seebeck found that when a circuit made from two dissimilar metals, with junctions at different temperature would deflect a compass needle. He realized that an ‘electromotive force’ will induce an electric current, which by Ampere’s law deflects the needle. More specifically temperature difference will induce an electric potential which can drive an electric current through the circuit defined as Seebeck effect [8]. Seebeck effect opens a new platform connecting relation between heat and electricity. It is the development of an electromotive force (EMF) across the material in response to the imposition of a temperature differential and the coefficient gauges its magnitude. The net Seebeck voltage thus developed can be measured using the thermocouple [9]. When a material is heated at one end and the other end get cooled or remained in the same environment, the electrons in the hot region will acquire higher velocity than those in the cold region. As a result there will be a net diffusion of electrons from the hot end towards the cold region leaving behind the positive metal ions in the hot region and accumulates electron in the cold region. Diffusion of electrons continue until the electric field developed between the positive ions in the hot region and excess electrons in the cold region prevents the further motion of electrons to the cold end [10]. By this convention, Seebeck effect can be mathematically defined as

$$S = \frac{V_{cold} - V_{hot}}{T_{hot} - T_{cold}} = \frac{\Delta V}{\Delta T} \quad (1.1)$$

where the sign of S represents the potential at the cold end with respect to the hot end [11]. The circuit with two dissimilar metals placed at temperature T_1 and T_2 creating a potential gradient ΔV .

Seebeck coefficient is a material property which depends on temperature

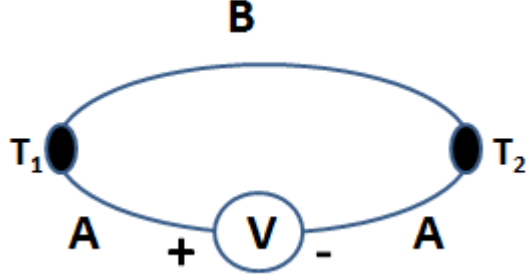


Figure 1.1: Representation of Seebeck effect.

given by

$$\Delta V = \int_T^{T_0} S dT \quad (1.2)$$

The voltage developed across each metal depends on its Seebeck coefficient so the potential difference developed between the two wires will depend on $S_A - S_B$. Thus the emf between two wires is given by the equation

$$V_{AB} = \int_{T_1}^{T_2} (S_A - S_B) dT = \int_{T_1}^{T_2} S_{AB} dT \quad (1.3)$$

If the electrons diffuse from hot end to the cold end, the cold end is negative with respect to the hot region and the Seebeck coefficient is negative then the material is termed to be n type. In a p type semiconductor the carriers are holes and thus the cold end will be positive with respect to the hot region which would make the S to be positive [12]. The current I flowing through the material can be expressed as

$$I = \frac{\int d\varepsilon g(\varepsilon)(f_1 - f_2)}{q} \quad (1.4)$$

where f_1 and f_2 are the Fermi distribution function of the cold and hot ends respectively. $g(\varepsilon)$ represents the density of states between energy ε and $\varepsilon + d\varepsilon$. The Fermi distribution function can be expressed as the function of chemical potential μ and temperature T,

$$f = \frac{1}{e^{(\varepsilon - \mu)/k_B T} + 1} \quad (1.5)$$

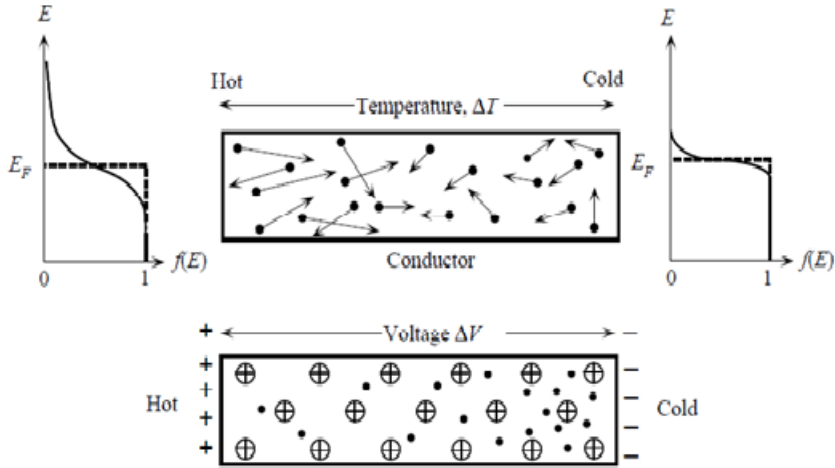


Figure 1.2: Fermi distribution at the hot and cold end [13].

For the same material, if there is no external voltage the chemical potential at both ends of the material will be the same and thus Fermi distribution depends only on the temperature at the ends. The materials temperature, crystal structure and impurities are the factors influencing the value of thermoelectric coefficients and it is a fundamental electronic transport property which measures the entropy transported with charge carriers as they move. For a bulk material kept at elevated temperature, hotter side of the material have high energy level which have a higher carrier occupation per state and lower energy level have lower occupation per state. The high-energy carriers diffuse away from the hot end, and produce entropy by drifting towards the cold end of the device. However, there is a competing process: low-energy carriers are drawn back towards the hot end of the device. Though these processes both generate entropy, they work against each other in terms of charge current and a net current occurs only if one of these drifts is stronger than the other. The thermoelectric coefficient S depends literally on the way by which the high energy carriers are conductive compared to low-energy carri-

ers. The distinction may be due to difference in rate of scattering, difference in speed, difference in density of states or a combination of these states [14].

1.2.2 Peltier effect

In 1834 Peltier discovered that passing an electric current at a constant temperature through two dissimilar materials produces heating or cooling at their junction known as “Peltier effect” and later used to make refrigerator [15]. The magnitude of this heat current is given by $\Pi \times \mathbf{I}$, where Π is the Peltier coefficient defined as $(\Pi_A - \Pi_B) = \frac{1}{I} \frac{dQ}{dt}$ and \mathbf{I} is the current passing through dissimilar conductors in the circuit. Depending on the direction of current, heat can be absorbed or released at the junction of two dissimilar conductors as shown in Fig: 1.3. If the Fermi energy level of the material ‘A’ is larger than that of ‘B’, then heat is released at the junction or else heat is absorbed. Peltier effect explains the principle behind thermoelectric cooling. Peltier elements can be connected in series to construct Peltier modules which have greater cooling capabilities.

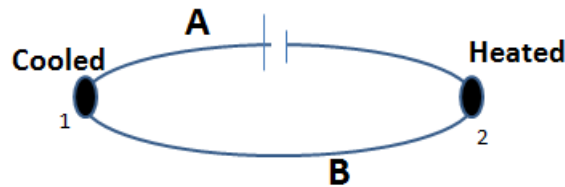


Figure 1.3: Demonstration of Peltier effect.

1.2.3 Thomson effect

In 1851 William Thomson, found that the Seebeck and Peltier effects are related, indicating that any thermoelectric material can be used either to generate power in a temperature gradient or pump heat with an applied current [16]. Thomson effect defines the rate of generation of reversible heat q which results from the passage of current along a portion of a single conductor

along which there is a temperature difference ΔT . Providing the temperature difference is small, $q = \beta I \Delta T$ where β is the Thomson coefficient.

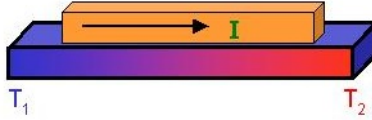


Figure 1.4: Demonstration of Thomson effect [17].

In 1854 Lord Kelvin found relationship between the three thermoelectric effects. They are actually the different manifestation of one effect uniquely characterized as Seebeck coefficient and the three coefficients are related by first Thomson relation [18],

$$\beta = \frac{d\Pi}{dT} - S \quad (1.6)$$

The second Thomson relation express a subtle and fundamental relation between Peltier and Seebeck effect given by

$$\Pi = TS \quad (1.7)$$

Thus the first Thomson relation becomes

$$\beta = T \frac{dS}{dT} \quad (1.8)$$

It is important that second Thomson relation can be used only for time reversal symmetry operation. The Thomson coefficient can be determined for the individual materials which made it unique among the three main thermoelectric coefficients. The Peltier and Seebeck coefficients can be easily determined for pairs of materials and hence, it is difficult to find absolute values for Seebeck or Peltier coefficients for an individual material rather it can be used for pairs of materials. If the Thomson coefficient of a material is measured over a wide temperature range, it can be integrated using the Thomson relations to determine the absolute values for the Peltier and Seebeck coefficients.

1.3 Efficiency of thermoelectric material

Thermoelectric generators are solid state devices that can convert heat in to electricity and can be considered as a heat engine which can obey the laws of thermodynamics. Thermoelectric generator or module can be constructed by connecting an electron conducting (n-type) and hole conducting (p-type) materials electrically in series and thermally in parallel as shown in Fig: 1.5. This will results for a net voltage that can be driven through a load. The

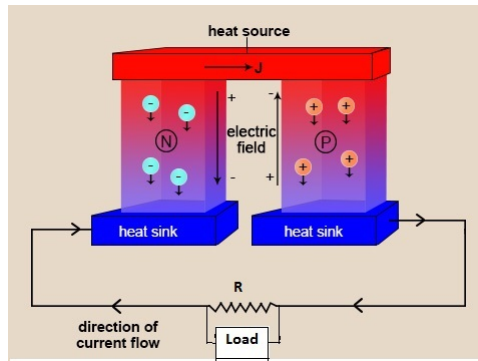


Figure 1.5: Thermoelectric Module [19].

efficiency of a generator can be defined as

$$\eta = \frac{\text{Work done by the engine}}{\text{Heat flow through the engine}} = \frac{W}{dQ/dt} \quad (1.9)$$

It is assumed that the electrical conductivity σ , thermal conductivity κ , and Seebeck coefficient S of the n and p type materials are constant within an arm, and that the contact resistances at the hot and cold junctions are negligible compared with the sum of the arm resistance. The work done by the device is the contribution from the Seebeck voltage subtracted by Joule heating term:

$$W = IV_{tot} = I\Delta V_{Seebeck} - I\Delta V_R = IS\Delta T - I^2R \quad (1.10)$$

The expression for heat flow due to the thermal conductance of the material, Q_κ , the Peltier effect Q_Π are cumulative, opposed by the Joule heating effect.

That is,

$$\frac{dQ}{dt} = \kappa\Delta T + IST - I^2R \quad (1.11)$$

Thus, the efficiency can be expressed as

$$\eta = \frac{IS\Delta T - I^2R}{\kappa\Delta T + IST - I^2R} \quad (1.12)$$

where κ is the thermal conductance of material in parallel and R is the series resistance.

The electrical conductivity (σ), thermal conductivity (κ), and Seebeck coefficient(S) changes with temperature during power generation and cooling. The maximum current through the load can be obtained by equating the first derivative of η equal to zero and solving for I_{max} .

$$I_{max} = \frac{S\Delta T}{R[\sqrt{1 + (\frac{S^2}{R\kappa})T} + 1]} \quad (1.13)$$

where the figure of merit, $Z = \frac{S^2}{R\kappa}$, which is found in the denominator. It is obvious that Z will be maximum when $R\kappa$ will have minimum value and this will occur when

$$\frac{A_p/l_p}{A_n/l_n} = \sqrt{\frac{\sigma_n\kappa_n}{\sigma_p\kappa_p}} \quad (1.14)$$

where A and l are the area and length of the ‘n’ and ‘p’ type material. Substituting equation 1.13 in 1.12 to yield the efficiency of thermoelectric generator $\eta(Z)$

$$\eta = \frac{T_H - T_C}{T_H} \frac{\sqrt{1 + ZT} - 1}{\sqrt{1 + ZT} + T_c/T_H} \quad (1.15)$$

The efficiency of the TE generator depends on the intrinsic property of the material through the parameter figure of merit. As Z tends to ∞ , the efficiency approaches the Carnot limit. Thus figure of merit is an important parameter used to characterize the ability of a material to convert heat into electrical energy. It is usually represented as Z and to make it dimensionless it is denoted as ZT. For a material, figure of merit is defined as

$$ZT = \frac{S^2\sigma}{\kappa}T \quad (1.16)$$

where T is the temperature, S is the Seebeck coefficient or thermo power, σ is the electrical conductivity and κ is the total thermal conductance. The energy conversion efficiency of a thermoelectric material depends on the value of ZT . In order to have a material with good ZT it should have a high thermopower, high electrical conductivity and a low thermal conductivity. Power factor is defined as the ability of a material to produce useful electrical power at a given temperature difference. For a thermoelectric material powerfactor is stated as $S^2\sigma$. High electrical conductivity is necessary in order to minimize Joule heating, while a low thermal conductivity helps to retain heat at the junctions and maintain a large temperature gradient [20]. These three parameters are considered to be the reflection of charge carrier concentration. Electrical and thermal conductivity of the material increases with carrier concentration while the Seebeck coefficient decreases. Achiev-

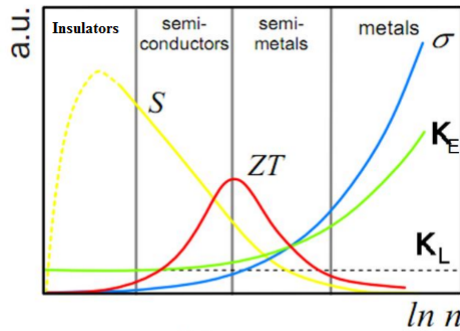


Figure 1.6: Dependence of carrier concentration on thermoelectric parameters [21].

ing these three parameters in favour of high figure of merit in a material is the main challenge faced by the researchers. From the Fig: 1.6 it is clear that semiconductors are the best candidate for thermoelectric applications because there is an inherent optimization parameter to obtain reasonable power factor. Even though there is no theoretical limit for the value of ZT , there are some practical limitations to achieve high value.

1.3.1 Thermal conductivity

Thermal conductivity is a material property describing the ability to conduct heat or determines how the atoms composing the system interact. It is defined as the quantity of heat transmitted through a unit thickness of a material in a direction normal to a surface of unit area due to a unit temperature gradient under steady state conditions. As atoms vibrate more energetically one part of a solid transfer that energy to less energetic neighbouring atoms. Thus thermal conductivity can be defined as:

$$\kappa = \frac{\Delta Q}{\Delta t} \times \frac{1}{A} \times \frac{x}{\Delta T} \quad (1.17)$$

where $\frac{\Delta Q}{\Delta t}$ is the rate of heat flow, $\frac{\Delta T}{x}$ is the temperature gradient, Δt is the time for which heat flow occur, A is the area of cross section of the thermoelectric material with thickness x . Heat conduction in a crystal depends on the thermal vibration of the crystal lattice due to phonons and free charge carriers. The total thermal conductivity can be expressed as

$$\kappa = \kappa_{el} + \kappa_{ph} \quad (1.18)$$

Electronic contribution to the thermal conductivity κ_{el} is generally a function of carrier concentration. As the carrier concentration increases both the electrical and electronic thermal conductivity increases as stated by the Wiedemann-Franz Law [22].

$$L = \frac{\kappa_e}{\sigma T} \quad (1.19)$$

where the L represents the Lorentz number.

From Kinetic theory, it can be demonstrated that

$$\kappa_{ph} = 1/3 C_v v l \quad (1.20)$$

where C_v is the specific heat, v is the speed of sound and l gives the mean free path of the phonon. Since the electronic part of thermal conductivity is directly proportional to its electrical conductivity, this part has to be preserved. Approach of reducing total thermal conductivity thus primarily focuses on the reduction of phonon mean free path. Thermal resistivity

arises mainly from phonon scattering mechanisms such as phonon-phonon scattering, scattering by the crystal lattice and phonon electron scattering [23]. Due to the anharmonicity within the crystal potential, the phonons in the crystal get scattered. Phonon-phonon scattering are of two types: Normal(N-processes) or Umklapp (U-processes). N-processes do not change the net phonon momentum and contribute few to the thermal resistance. On the contrary, U-processes result in the creation of third phonon due to phonon-phonon interaction and the net phonon momentum changes contribute to thermal resistance. At moderately high temperature U-process are the primary phonon scattering mechanism and contribute towards the lattice thermal conductivity as follows; $\kappa_{ph} \propto 1/T$. At low temperature, the number of phonon contribution is relatively small and the phonon scattering at the grain boundaries will be prominent and κ_{ph} follows as $\kappa_{ph} \propto T^3$. In the intermediate temperature range both combination of grain boundary scattering and point defect scattering will be present [24]. Fig: 1.7 represents the thermal conductivity of highly ordered crystal structure at low to intermediate temperature whereas flattening of the peak indicates the increased disorder in the crystal lattice. Due to this scattering mechanism thermal

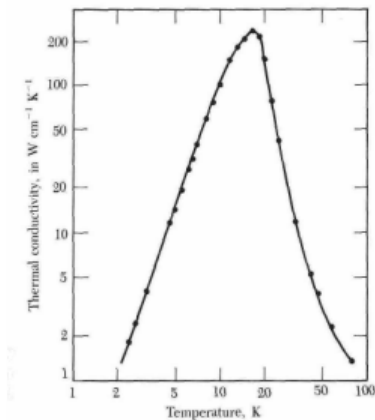


Figure 1.7: Variation of lattice thermal conductivity with temperature due to different scattering mechanism [25].

conductivity of the material get reduced. The reduction in thermal conduc-

tivity will enhance the figure of merit of the sample. Thus enhancement of figure of merit mainly depends on the reduction in thermal conductivity due to phonon scattering. From the Fig: 1.8 it is clear that total thermal conductivity is moderate for semiconductors compared to metals and insulators which ensured semiconductors were the best candidate for thermoelectric application. It also pictures out lattice thermal conductivity is independent of carrier concentration.

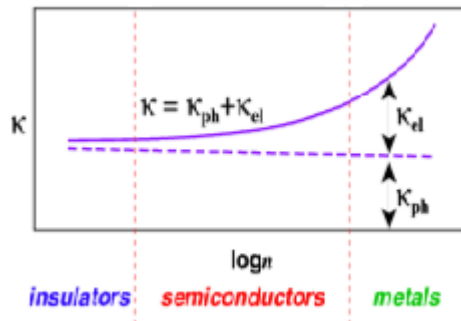


Figure 1.8: Thermal conductivity in materials [26].

1.3.2 Electrical conductivity

Drude and Lorentz proposed the idea of conduction of electrons in solids using classical physics. The current density 'J' of the material is defined as $J = nev$ and $J = \sigma E$; combining these two equations we have

$$\sigma = ne\mu \quad (1.21)$$

where σ is the electrical conductivity, n gives the carrier concentration and μ defines the mobility of the free charge carriers. Sommerfeld [27] put forward the free electron theory and was able to explain the difference between the metallic conductors and insulators. When individual atoms are brought together in a solid, their interatomic spacing decreases and the interaction

of electrons in the crystal lattice with the periodic potential resulted in the formation of discrete bands that are separated by forbidden regions or energy gap. According to the Fermi distribution function, the probability of an electron to occupy in an energy level E ,

$$f_0(E) = [\exp(\frac{E - E_F}{k_B T}) + 1]^{-1} \quad (1.22)$$

where E_F depends on the total number of electrons that can be occupied and k_B is the Boltzmann's constant. The number of permitted electron states in the energy range between E and $E + dE$ is represented by

$$n = \int_0^\infty f_0(E)g(E)dE \quad (1.23)$$

where $g(E)$ represents the density of states. Fig: 1.9 represents the band diagram for metals, semiconductors, semimetal and insulator. Figure clearly points out that the conduction will take place in partially filled band structure rather than the empty conduction band and fully occupied valence band. At absolute zero temperature (0 K) the electrons fill up the lowest possible energy levels termed as valence band and the conduction band is completely empty. Because of that no electronic conduction take place in an insulator and semiconductor in an applied field. When the temperature is increased,

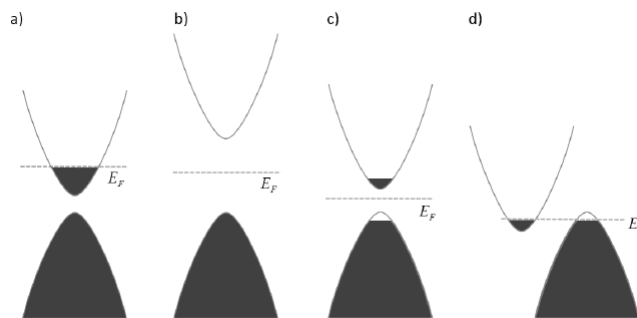


Figure 1.9: Energy band diagram for a)metal, b)insulator, c)semiconductor, d)semimetal [28].

electrons in the valence band are excited across the forbidden energy gap

to the conduction band termed as intrinsic ionization. Intrinsic ionization results in conduction mechanism and thus produces pairs of electrons and holes. The intrinsic ionization energy for the insulator is very high and thus conduction will not take place.

According to classical statistics, the concentrations of electrons and holes in an intrinsic semiconductor are equal, and thus

$$n = p = K_i^{1/2} = (N_c N_v)^{1/2} \exp(-E_g/2kT) \quad (1.24)$$

where K_i is the equilibrium constant for the intrinsic ionization, E_g is the band gap, $E_g = E_c - E_v$ and it can be considered as the enthalpy of the intrinsic ionization. In most of the semiconductor oxides the conductivity increases with increase in temperature and due to the increment in the number of electronic defects. Thus the electronic conductivity, σ_{el} , of a semiconducting oxide is given by

$$\sigma_{el} = \sigma_n + \sigma_p = en\mu_n + ep\mu_p \quad (1.25)$$

Where σ_n and σ_p are the electron and hole conductivity, μ_n and μ_p are the carrier (or drift) mobility of electrons and holes. Thus electrical conductivity can be defined as

$$\sigma = e(N_c N_v)^{1/2} (\mu_n + \mu_p) \exp(-E_g/kT) \quad (1.26)$$

N_c and N_v represent the density of states or the number of available states per unit volume in the conduction and valence bands. The parameter E_F is termed as the Fermi level of the intrinsic material. Effect of impurities or defects contribute additional localized energy levels in the crystal and they fall within the forbidden gap. When the imperfection introduces an energy level which is located below the lower edge of the conduction band E_c , electrons can be thermally excited to the conduction band and results for conduction. Correspondingly, imperfections with energy levels just above the upper edge of the valence band (E_v) are termed as acceptor level and electrons in the valence band may be excited to the acceptor level cause

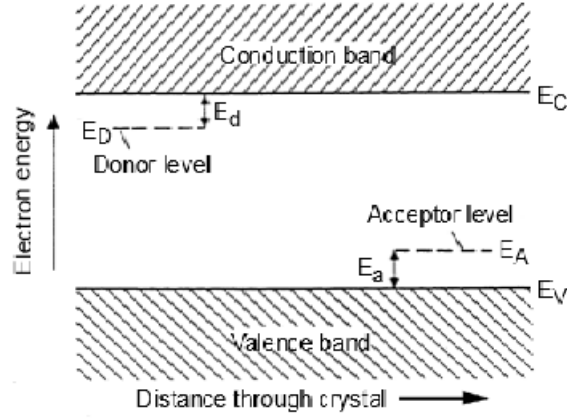


Figure 1.10: Energy band diagram of a doped semiconductor [29].

conduction mechanism. Thus equilibrium constant for the acceptor level and donor level can be defined as

$$K_A = N_v \exp(-E_a/k_B T) \quad (1.27)$$

where $E_a = E_A - E_V$ is called the ionization energy of the acceptor.

$$K_D = N_c \exp(-E_d/k_B T) \quad (1.28)$$

where $E_d = E_C - E_D$ E_A is the energy level of the acceptor and E_D denotes the energy level of the donor.

1.4 Transport effects in metals and semiconductors

If the distribution function f , is disturbed from its equilibrium value f_0 ; the rate of change of f can be according to the relation

$$\frac{df(E)}{dt} = -\frac{f(E) - f_0(E)}{\tau_e} \quad (1.29)$$

As an approximation τ_e defines the relaxation time expressed in the form of $\tau_e = \tau_0 E^r$ where τ_0 and r are constants for given scattering cross section. The parameter r is equal to $-1/2$ if the scattering of charge carriers is predominant by the acoustic - mode lattice vibration and it is equal to $3/2$ if the scattering is predominated by the ionised impurities. Transport parameters were defined on the basis of Boltzmann equation which relates the effect of applied field and scattering of charge carriers. If the disturbance to the distribution is small it can be defined as

$$\frac{f(E) - f_0(E)}{\tau_e} = u \frac{df_0(E)}{dE} \left(\frac{dE_F}{dx} + \frac{(E - E_F)}{T} \frac{dT}{dx} \right) \quad (1.30)$$

u is the velocity of carriers in the x direction and E_F is Fermi energy. The equation for the electric current density is

$$i = \mp \int_0^\infty e u f(E) g(E) dE \quad (1.31)$$

where e is the magnitude of electronic charge. The heat flux density is

$$j = \int_0^\infty u (E - E_F) f(E) g(E) dE \quad (1.32)$$

where $(E - E_F)$ is the energy transported by the carrier. Transport coefficients can be determined using equation 1.31 and 1.32 by replacing f by $(f - f_0)$ since there is no flow of any kind when $f = f_0$. Since the drift velocity of the carriers is a small part of the total velocity, it is well to replace u by $2E/3m^*$. The current density and heat flux can be defined by,

$$i = \mp \frac{2e}{3m^*} \int_0^\infty g(E) \tau_e E \frac{df_0(E)}{dE} \left(\frac{dE_F}{dx} + \frac{(E - E_F)}{T} \frac{dT}{dx} \right) dE \quad (1.33)$$

$$j = \pm \frac{E_F}{e} i + \frac{2}{3m^*} \int_0^\infty g(E) \tau_e E^2 \frac{df_0(E)}{dE} \left(\frac{dE_F}{dx} + \frac{(E - E_F)}{T} \frac{dT}{dx} \right) dE \quad (1.34)$$

By applying appropriate boundary conditions, we can determine the transport parameter electrical conductivity which is the ratio of i to the electric field when the temperature gradient $\frac{dT}{dx}$ is zero

$$\sigma = - \frac{2e^2}{3m^*} \int_0^\infty g(E) \tau_e \frac{df_0(E)}{dE} dE \quad (1.35)$$

The electronic contribution κ_e towards the thermal conductivity can be given by the ratio of j to $-dT/dx$ when the electric current is zero.

$$\kappa_e = \frac{2}{3m^*T} < \left[\frac{\int_0^\infty g(E)\tau_e E^2 \frac{df_0(E)}{dE} dE}{\int_0^\infty g(E)\tau_e \frac{df_0(E)}{dE} dE} \right]^2 - \int_0^\infty g(E)\tau_e E^3 \frac{df_0(E)}{dE} dE > \quad (1.36)$$

Seebeck coefficient is equal to the ratio of electric field to the temperature gradient under the same condition.

$$S = \pm \frac{1}{eT} \left[E_F - \frac{\int_0^\infty g(E)\tau_e E^2 \frac{df_0(E)}{dE} dE}{\int_0^\infty g(E)\tau_e \frac{df_0(E)}{dE} dE} \right] \quad (1.37)$$

It is easier to express these transport coefficient in the form of an integral K_s ;

$$K_s = \frac{-2T}{3m^*} \int_0^\infty g(E)\tau_e E^{s+1} \frac{df_0(E)}{dE} dE \quad (1.38)$$

It is able to eliminate g and τ_e in favour of m^* , r and τ_0 . Thus K_s can be represented as

$$K_s = \frac{8\pi}{3} \left(\frac{2}{h^2}\right)^{3/2} (m^*)^{1/2} T \tau_0 (s+r+3/2) (kT)^{s+r+3/2} F_{s+r+1/2} \quad (1.39)$$

where F_n represents the Fermi-Dirac integral and r corresponds to the scattering variable. The expression for the transport coefficient in terms of integral K_S ;

$$\sigma = \frac{e^2}{T} K_1 \quad (1.40)$$

$$\kappa_e = \frac{1}{T^2} \left(K_2 - \frac{K_1^2}{K_0} \right) \quad (1.41)$$

$$S = \pm \frac{1}{eT} \left(E_F - \frac{K_1}{K_0} \right) \quad (1.42)$$

The equations 1.39-1.41 relates the figure of merit of a thermoelectric device with that of Fermi energy, scattering parameter and the effective mass of the charge carriers.

1.5 Thermoelectric properties in metals and semiconductors

In order to evaluate the transport parameters for the metals and semiconductors different approximations have to be done for evaluating the Fermi Dirac integral. When the Fermi energy $E_F \gg k_B T$, the conductor is a metal and the degenerate approximation can be performed. Thus Fermi Dirac integral can be defined as

$$F_n(\eta) = \frac{\eta^{n+1}}{n+1} + n\eta^{n-1}\frac{\pi^2}{6} + n(n-1)(n-2)\eta^{n-3}\frac{7\pi^4}{360} + \dots \quad (1.43)$$

The series converges rapidly and for the evaluation of electrical conductivity, only the first term in the series is required.

$$\sigma = \frac{8\pi}{3} \left(\frac{2}{h^2}\right)^{3/2} e^2 (m^*)^{1/2} \tau_0 E_F^{r+3/2} \quad (1.44)$$

Thus Lorentz number which is the ratio of electronic contribution of thermal conductivity to the electrical conductivity is given by

$$L = \frac{\pi^2}{3} \left(\frac{k_B}{e}\right)^2 \quad (1.45)$$

The Seebeck coefficient requires two terms from the approximated series and defined as

$$S = \mp \frac{\pi^2 k_B}{3 e} \frac{(r+3/2)}{\eta} \quad (1.46)$$

For the case of non degenerate approximation that can be applied to extrinsic semiconductor with $E_F < 2k_B T$

$$F_n(\eta) = \exp(\eta) \Gamma(n+1) \quad (1.47)$$

Then the integral K_s can be defined as,

$$K_s = \frac{8\pi}{3} \left(\frac{2}{h^2}\right)^{3/2} (m^*)^{1/2} T \tau_0 (k_B T)^{s+r+3/2} \Gamma(s+r+5/2) \exp(\eta) \quad (1.48)$$

The expression for electrical conductivity for the non degenerate material

$$\sigma = \frac{8\pi}{3} \left(\frac{2}{h^2}\right)^{3/2} e^2 (m^*)^{1/2} \tau_0 (k_B T)^{r+3/2} \Gamma(r+5/2) \exp(\eta) \quad (1.49)$$

According to Drude model $\sigma = ne\mu$ where n and μ represents the carrier concentration and mobility of the free charge carriers. Deducing from equation 1.48 we have

$$n = 2\left(\frac{2\pi m^* k_B T}{h^2}\right)^{3/2} \exp(\eta) \quad (1.50)$$

$$\mu = \frac{4}{3\sqrt{\pi}} \left[(r + 5/2) \frac{e\tau_0 (k_B T)^r}{m^*} \right] \quad (1.51)$$

The Seebeck coefficient for the non degenerate semiconductors can be expressed using the reduced energy relation

$$S = \mp \frac{k_B}{e} (\eta - (r + 5/2)) \quad (1.52)$$

In a typical extrinsic semiconductor the value of η is greater than unity and the Seebeck coefficient will be several hundred micro volts per degree. Although the value of Seebeck coefficient differed for metals and semiconductors, the Lorentz number for the non degenerate material is given by

$$L = \left(\frac{k_B}{e}\right)^2 (r + 5/2) \quad (1.53)$$

For the case of non degenerate semiconductor the electronic component of the thermal conductivity is much smaller and the lattice component gets dominated. Thus the increase in thermopower for the non degenerate semiconductor must be balanced against a decrease in ratio of electrical to thermal conductivity. However, it turns out that most of the materials that can be used for thermoelectric applications are semiconductors in which the Fermi energy lies close to the edge of conduction or valence band. This idea has motivated the material researchers for the thermopower enhancement without significant variation in the electronic conductivity [18].

1.6 Strategies and criteria for the enhancement of figure of merit

Thermoelectric research is in the path of ground breaking progress over the past 10-20 years. The enhancement of figure of merit ZT , a measure

of competition between electronic transport (ie; power factor) and thermal transport (total thermal conductivity) has long surpassed and able to achieve unity while the researches are targeting a $ZT > 2$ as the new goal. The criteria and strategies for this goal include:

1. Thermopower enhancement: The idea towards the improvement of Seebeck coefficient was theoretically put forward by Hick and Dresselhaus using quantum confinement concept in low dimensional structures [30]. For a system of independent electrons containing static scatters the thermoelectric power S defined by the Mott's formula [31],

$$S = \frac{\pi^2 k_B^2 T}{3 e} \left(\frac{d}{dE} \ln \sigma(E) \right) \quad (1.54)$$

$$S = \frac{\pi^2 k_B^2 T}{3 e} \left(\frac{1}{n} \frac{d}{dE} g(E) f(E) + \frac{1}{\mu} \frac{d\mu}{dE} \right)_{E=E_F} \quad (1.55)$$

It was found that sharp variation in the electron density of states are required to increase $\frac{dg(E)}{dE}$ and thereby enhance the Seebeck coefficient. As the system size decreases and approaches to nanometer length scales, it is possible to vary S quasi independently. It is known that heavier

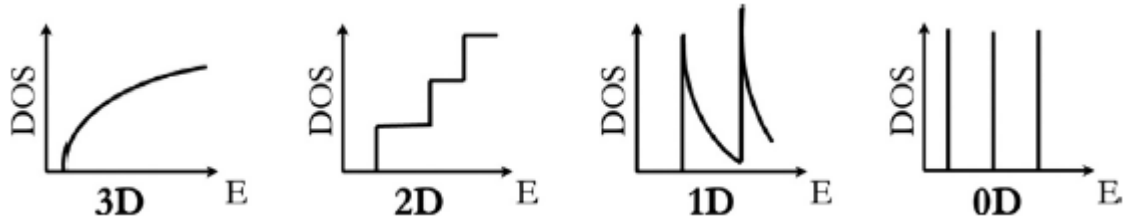


Figure 1.11: Density of states for different dimensions [32].

effective mass material will have larger Seebeck coefficient and they are desirable for thermoelectric application. As the density of states increases, the bands distorted and there occurs an enhancement in the effective mass. Depending on the effective mass the mobility of free charge carriers get varied as per the relation $\mu = \frac{e\tau}{m^*}$. The increase in the effective mass diversely affect the mobility and the net thermopower

decreases. This can be compensated by the formation of multivalley in semiconductors with moderate inertial mass to increase the density of states without sacrificing the mobility. It was Mahan [34] proposed the idea of multivalley semiconductors with small inertial mass would have the largest value of μ provided the intervalley scattering is minimized. Effective mass with multivalley is given by $N_v^{2/3}(m_1m_2m_3)^{1/3}$, where N_v is the number of equivalent valley and m_1, m_2, m_3 are inertial masses at each direction. For fixed E_F , multivalley band structure yields the same Fermi velocity with higher density of states. This lead to larger carrier density $n(E)$, along with the same Seebeck coefficient. Thus thermoelectric power factor get maximizes through optimization of Seebeck coefficient over the single valley counterpart.

2. Enhancement of electrical conductivity: The high level of doping is required to provide the high density of charge carriers for conduction. However, at the same time the ionized impurities serve as scattering centers and hinder the carrier mobility to disturb the conduction mechanism. Through modulation-doping all the dopants are allowed to concentrate in a thin doping layer, which is away from the main transport channel and thus to reduce the ionized impurity scattering. Modulation doping is most significant at low temperature where ionized impurity scattering dominates whereas at higher temperature phonon scattering has least effect on the doping mechanism. Preferentially aligning the crystallites (grains) along the same transport direction in thin films can also be opted for good thermoelectrics.
3. Reduction of thermal conductivity: According to Widemann-Franz law the thermal conductivity has contribution from two parts. 1) Electronic thermal conductivity (κ_{el}) due to the flow of electrons, which is proportional to electrical conductivity. 2) Lattice thermal conductivity (κ_{ph}) due to the transfer of phonons by the lattice vibrations. Based on the electron crystal concept electronic thermal conductivity should be pre-

served and the ultimate aim of reducing the thermal conductivity lies on the decrement in the lattice part. There are mainly four ways for the reduction of lattice thermal conductivity (LTC).

- Nanostructuring : Nanostructured grains become an efficient way of lowering the lattice thermal conductivity (LTC). Electrons which have a shorter wavelength will be scattered during its motion whereas the phonons are not affected by the micro grains. Nano grain boundaries hinders the path of phonons and get scattered which cause for the reduction of LTC. This concept was feasible only at low temperature, owing to the increase in grain size at higher temperature.
- Insertion of point defects and the rattling of ions : This concept will be effective when an atom with considerable size difference was introduced in the lattice. Moreover, the filling atom comprises rare earth elements which as expensive.
- Formation of secondary phases : Precipitation of secondary phases in the matrix for the scattering of phonons with the fine grains of the secondary phase. On the other hand secondary phases normally affects the high frequency phonons whereas low frequency acoustic waves are not affected by this mechanism.
- Formation of inhomogeneous pores : Randomly oriented pores are effective for the scattering of phonons at the pore boundary. Homogeneous macro pores will make the material less dense. Thus inhomogeneous pores act as good centers for scattering phonons at different wavelength.

1.7 Thermoelectric materials

Slack in 1856 proposed general rules for new thermoelectric materials which focus on the increase of ZT value [35]. General rule should point out the increase in power factor $S^2\sigma$ and decrement in thermal conductivity. it can be obtained by

1. Higher carrier concentration and mobility.
2. Reduction in lattice thermal conductivity.
3. Increased density of states which alters the value of m^* .
4. Mobility, resistivity, effective mass should vary independent of charge carrier concentration.

These characteristics point towards a material as Phonon glass electron crystal (PGEC). These are materials with low lattice thermal conductivity having the property of amorphous materials, but still have electric properties like a crystalline material. Another way to decouple σ and κ is to introduce nanostructures. Reduction of lattice thermal conductivity by scattering of phonons at the nano grain boundaries is the main criteria behind this development [39].

1.7.1 Skutterudites

Higher ZT value of 1.7 at 850 K was obtained for the multiple filled skutterudites by separately optimizing electrical, thermal transport and they can be considered to be a promising TE material. The general formula of MX_3 where M belongs to transition metal and X represents a non metallic atom.

The inherent void formed between the octahedron form the lattice site for the foreign element which will act as rattler atom and a dopant as shown in Fig: 1.12. The group velocity of the phonon and thereby lattice thermal conductivity get decreased due to the foreign impurity. However, optimum filler concentration donates free electron and enhances the electrical conductivity. The sublimation temperature for the skutterudites are above 380°C and for the most promising skutterudite CoSb_3 the sublimation temperature is about 550°C which limits its application [38]. To avoid degradation these materials should ideally be coated or kept at inert atmosphere.

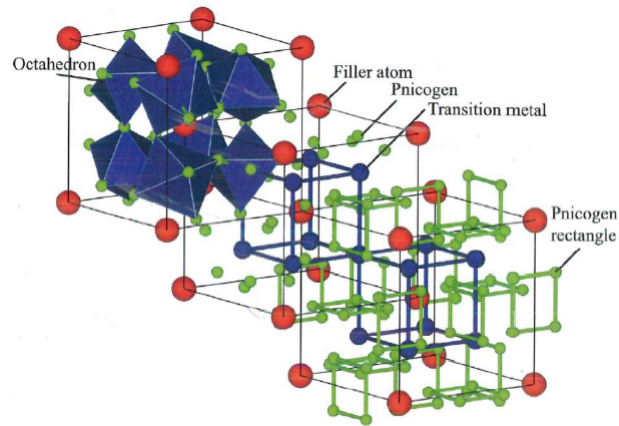


Figure 1.12: General representation of MX₃ [37]

1.7.2 Clathrates

Clathrates are good example for PGEC material. The general formula is $A_xB_yC_{46-y}$. As seen in Fig:1.13, B and C form a tetrahedrally bonded rigid frame work of cages which enclose the guest metal atom A. The guest atom A

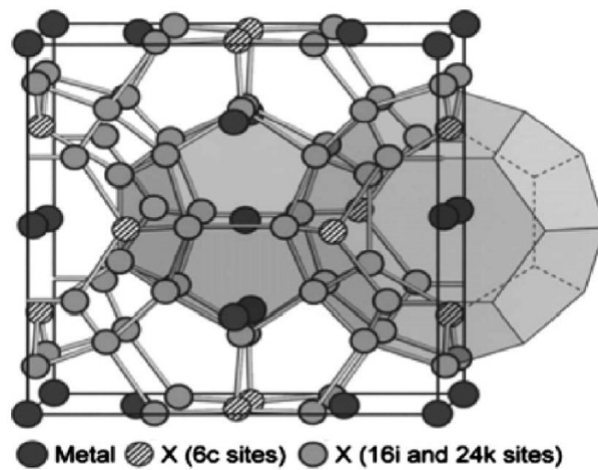


Figure 1.13: Crystal structure of type-I clathrate compounds with general formula $A_xB_yC_{46-y}$ [39].

in the void will act as a barrier for phonon transport and cause disturbance in the lattice and thereby reduce the lattice thermal conductivity. Huge

amount of compounds are required for the production of clathrates and the correct stoichiometry cannot be preserved during the synthesis process [40]. This hinders the mass production of the material.

1.7.3 Silicides

Silicides are a promising class of thermoelectric material as they possess good TE property along with good mechanical and chemical stability [41]. MnSi_x ($x=1.7-1.77$) is the most promising among this group. It has a complex and large crystal structure which offers the amorphous behavior of the lattice part of thermal conductivity. Other types of silicides include chromium disilicide (CrSi_2) with a ZT value of ≈ 0.3 . The others are FeSi_2 , Ru_2Si_3 and CoSi .

1.7.4 Half-Heussler compounds

These are compounds with chemical formula ABX. The simple rock salt structure formed by A, X and filled with B. These compounds are similar to that of the PbTe family. They have a high Seebeck coefficient and electrical conductivity but also possess quite high thermal conductivity. This can be overcome by introducing a heavier filler atom to increase the phonon scattering at the boundaries. They possess relatively higher temperature stability. MgAgAs , ZrNiSn belongs to this group and a ZT value of 1.5 had been reported [42].

1.7.5 Oxides

High thermal stability and oxidation resistance at high temperature along with low thermal conductivity are the most important benefits of oxide TE material. Due to its low electrical conductivity the oxides were discarded for TE application. The way of maximising ZT is to obtain materials with optimal charge carriers ('n') and to increase their mobility to obtain high σ at a fixed 'n' and to decrease κ_{ph} in κ . Conventional thermoelectrics developed in

1990 include intermetallic compounds and alloys due to the covalent bonding character (higher mobility) and consist of heavy metals (such as Bi, Te) to lower the κ_{ph} . However, these materials are not able to achieve wide commercialization because of poor durability at high temperature, low abundance and high toxicity and cost.

Metal oxides are ionic compounds consisting of metal cation and oxygen anion bond together by the coulombic attraction. Since the metal-oxygen bonds are largely polarized the conduction electrons have the tendency to localized on '+' charge metal cation and thereby reduces the mobility. Moreover large bonding energies of ionic bond and small atomic mass of oxygen give a high velocity of elastic waves to propagate through the lattice yielding a high lattice thermal conductivity. These inherent characters within the metal oxides are obviously against the working principle of TE materials to obtain higher ZT and thus they have been completely disregarded from TE class of materials.

In mid 1990s however the new guiding principle in TE materials include oxides for thermoelectric application due to its high durability at high temperature in air, non toxic, low cost and minimal environmental impact. High mobility oxides were introduced with an aim of increasing the electrical conductivity and for the reduction of thermal conductivity. In ionic crystals such as oxides, conductive electrons polarize the surrounding crystal lattice by strong electron lattice interaction, localizing themselves on the lattice points which is termed to be polarons. These polarons are responsible for inducing lattice distortion and the hopping of charge carriers induce mobility thereby enhancing the electrical conductivity [43]. The layered NaCo_2O_4 showed promising thermoelectric property with a ZT value of 0.8, which activated the research on oxide thermoelectric. Nano block crystal structure of NaCo_2O_4 form alternating layers of ordered CoO_2 and disordered Na atoms. The CoO_2 layer act effectively as good electron conductor and the disordered Na layer disturbs the phonon transport along the matrix [44]. Layered oxides thus form a promising candidate for thermoelectric application. CaMnO_3

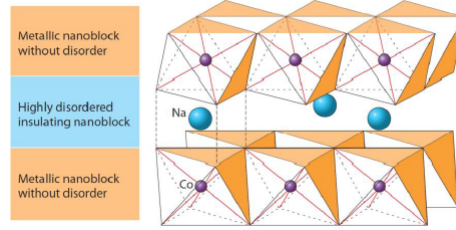


Figure 1.14: Crystal structure of NaCo_2O_4 [44].

based perovskites, Al doped ZnO [45], layered $\text{Ca}_3\text{Co}_4\text{O}_9$ [46] and SrTiO_3 [47] emerged as good thermoelectric material.

1.8 Zinc oxide (ZnO)

ZnO is the most important thermoelectric material among oxides used for high temperature energy conversion. Zinc oxide is well known as n type conductive oxide with a wide band gap of 3.36 eV. The conduction band of ZnO mainly constitutes the lowest unoccupied 4s and 2p orbital's which results for the higher mobility of conduction electrons [48]. The fairly large electronegativity of Zn, small ionicity and strong preference for the sp^3 hybridization of the Zn–O bond appear to be promising that their covalent character would result in the higher carrier conduction mechanism [49]. It can show either a hexagonal wurtzite, cubic Zinc blende or rarely rock salt structure (formed only at high pressure). The hexagonal wurtzite structure with $P6_3mc$ space group, is the most stable polymorph of ZnO . In wurtzite structure, every Zn atom is surrounded by tetrahedrally bonded oxygen atom. Zinc blende structure will be formed if ZnO is grown on cubic substrates.

1.8.1 Thermoelectric properties of pure ZnO

ZnO can be considered as a promising TE material only at high temperature. At ambient temperature pure ZnO shows a power factor of $\approx 800 \mu\text{W}/\text{mK}^2$ however due to its high thermal conductivity of about $40 \text{W}/\text{mK}$ it cannot

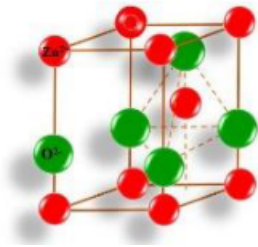


Figure 1.15: Wurtzite structure of ZnO [50].

be used for TE application [51]. At higher temperature of about 1000 K the thermal conductivity reduces to 5 W/mK due to the increased phonon scattering caused by the anisotropic thermal expansion. Nanostructuring arose as a vibrant approach for the enhancement of ZT value. From the literature review it was pointed out that nano grain boundaries at room temperature possess a lower κ value of about 2-3 W/mK and these structures exhibit an enhanced ZT value. For the sputtered ZnO thin film the power factor was found to be $1000\mu W/mK^2$ at 700 K. The increased density of states by quantum confinement results the enhanced Seebeck coefficient and thus the ZT value increases.

1.8.2 Thermoelectric properties of non-stoichiometric and doped ZnO

Non-stoichiometric or doped ZnO is found to possess much improved TE property. Recently ZnO based TE oxides such as Al-doped ZnO [52], Ga doped ZnO [53] and Ni doped ZnO [54] have received extensive attention in high temperature TE power generation system. Modification in the ZnO lattice can be achieved using several ways; for instance it was recently reported by Toshiki Tsubota et.al with the increase in carrier concentration the ZT value approaches 0.3 for 2 atomic % of Al doping in ZnO at 1000 K [45]. Masaki Kazeoka et.al reported the partial substitution of Yttrium as scattering center for indium in $(ZnO)_5(In_2)O_3$ and found to have a ZT value of 1.1-1.3 at 1000 K [55]. Toshiki Tsubota et.al also reported the enhancement

in the ZT value for In and Ga doped ZnO by reducing the lattice thermal conductivity [56]. Xin Liang reported the enhancement in thermoelectric figure of merit with Fe content in nano ZnO lattice, due to the reduced thermal conductivity by point defect scattering of phonons and enhanced electrical transport through doping [57].

1.9 Motivation and Objectives

Over a couple of years there occurs a dramatic improvement in the field of thermoelectrics. The waste heat released can be effectively and efficiently used by thermoelectric modules for power generation in order to reduce our dependence on conventional energy sources. The development and use of bulk, nano materials and super lattices for the fabrication of TE modules become wide spread and it is in the path of progress. However, the enhancement of efficiency of a TE material found to be difficult among the material researches and the current issue lies in the fact of maximizing ZT .

The objective of this work is to synthesis efficient thermoelectric material and to determine the factors contributing for the enhancement of TE efficiency. ZnO was taken as the base compound since it posses good electrical conductivity and excellent thermal stability at higher temperature. Larger ionic radii, rare earth element Dysprosium was choosen to be the trivalent dopant for modulating the ZnO lattice. It is expected that the additional free charge carriers enhance the electrical conductivity and the distortion in the lattice due to Dy incorporation reduce the thermal conductivity. Stratergies such as doping, quantum confinement and introduction of micro-meso pore structure at the nano grain boundary is expected to be the different possibilities for the augmentation of TE efficiency. Thus oxide material can be emerged as a potential candidate for high temperature thermoelectric application.

References

- [1] G.J. Kolb, C.K. Ho, T.R. Mancini, J.A. Gary, US Energy Inf. Adm. 14 (2013) 5–7.
- [2] T.M. Tritt, ed., SEMICONDUCT SEMIMET, 69 (2000) 188.
- [3] Rowe D. M., Int.J. Innov. Energy Syst. Power. 1 (2006) 13.
- [4] Rowe, D.M., CRC Handbook of Thermoelectrics, (1995), CRC Press.
- [5] L. E. Bell, Science, 321 (2008) 1457-1461.
- [6] G.L.Bennett, Space Nuclear Power– Opening the Final Frontier, (2006) 26-29.
- [7] H.J. Goldsmid, Introduction to Thermoelectricity, Springer Berlin Heidelberg, Berlin, Heidelberg, (2010).
- [8] Seebeck, T J Magnetic polarization of metals and minerals, (1822) 289.
- [9] Jeffrey Snyder G, Eric S. Toberer, Complex thermoelectric materials, (2008).
- [10] Kasap S O, Thermoelectric effects in metals: thermocouples (2001).
- [11] M. Ohtaki, D. Ogura, K. Eguchi, and H. Arai, J. Mater. Chem. 4 (1994) 653.

- [12] Koumoto K, Terasaki I, Funahashi R, MRS Bull. 31 (2006) 206.
- [13] D. Berardan, E. Guilmeau, A. Maignan, and B. Raveau, Solid State Commun. 146 (2008) 97.
- [14] Uemura K, Journal of Thermoelectricity, 3 (2002) 7.
- [15] Yuri G.Gurevich, Jesus Enrique Velazquez-Perez, Peltier Effect in Semiconductors, John Wiley and Sons, (2014).
- [16] Terasaki, Sasago Y and Uchinokura, K., Phys. Rev. B. 56 (1997) 12685.
- [17] [http : //farm4.static.flickr.com/3624/3482625739_97739eb98.jpg](http://farm4.static.flickr.com/3624/3482625739_97739eb98.jpg)
- [18] Goldsmid H J, Applications of Thermoelectricity ed.Worsnop B L, (1960).
- [19] P. Y. Yu and M. Cardona, Fundamentals of Semiconductors (Springer, Heidelberg), (1996).
- [20] G.S. Nolas, J. Sharp, and H.J. Goldsmid. Thermoelectrics: Basic Principles and New Materials Developments. Springer, Berlin, (2001).
- [21] S. Ohta, T. Nomura, H. Ohta, M. Hirano, H. Hosono, and K. Koumoto, Appl. Phys. Lett. 092108 (2005) 092108.
- [22] A. Bejan, A. D: Allan, Heat Transfer Handbook Wiley, New York, (2003) 1338.
- [23] R. Berman, Sci. Progr. 55 (1967) 857.
- [24] P. G.Klemens, Phys. Rev. 119 (1960) 507.

- [25] J. Yang, Theory of Thermal Conductivity, In Thermal Conductivity: Theory, Properties and Applications, ed. T.M. Tritt, (2004) 1-20.
- [26] C. Wood, Rep. Prog. Phys. 51 (1988) 459.
- [27] A. Sommerfeld, Z. Phys. 47 (1928) 43.
- [28] D.N. Sheng, Zheng-Cheng Gu, Kai Sun, and L. Sheng, Nat. Commun. 2 (2011) 389.
- [29] O. Madelung, Semiconductors-Basic Data, Springer, Berlin, (1996).
- [30] L. D. Hicks, T. C. Harman, M. S. Dresselhaus, Appl. Phys. Lett. 63 (1993) 3230.
- [31] M. Jonson and G. D. Mahan, Phys.Rev.B. 21 (1980) 10.
- [32] By Mildred S. Dresselhaus, Gang Chen, Ming Y. Tang, Ronggui Yang, Hohyun Lee, Dezhi Wang, Zhifeng Ren, Jean-Pierre Fleurial, and Pawan Gogna, Adv. Mater. 19 (2007) 1043–1053.
- [33] M.S. Dresselhaus, et al. in: M.G. Kanatzidis, T.P. Hogan, S.D. Mahanti (Eds.), Chemistry, Physics and Materials Science of Thermoelectric Materials: Beyond Bismuth Telluride, (2003).
- [34] G.D. Mahan, Solid State Sciences. 51 (1997) 82–157.
- [35] Slack, G.A., CRC Handbook of Thermoelectrics, D.M. Rowe, Editor. 1995, CRC Press, Tylor and Francis group: Boca Raton, Florida.
- [36] Shi, X., et al., J. Am. Chem. Soc. 133 (2011) 7837-7846.
- [37] X. Shi, W. Zhang, L. D. Chen, and J. Yang., Phys. Rev. Lett. 95 (2005) 185503.

- [38] Sales B C, Mandrus D, Chakoumakos B C, Keppens V, Thompson J R, Phys. Rev. B. 56 (1997) 15081.
- [39] Alam, H. and S. Ramakrishna, Nano Energy, 2 (2013) 190-212.
- [40] Nolas, G.S., Structure, Thermoelectrics Handbook, Macro to Nano, D.M. Rowe, Editor, CRC Press, Tylor and Francis group: Boca Raton, Florida (2006) .
- [41] Fedorov, M.I., Journal of Thermoelectricity, 2 (2009) 51-60.
- [42] Sakurada, S. and N. Shutoh, Appl. Phys. Lett. 86 (2005).
- [43] M. Ohtaki, T. Tsubota, K. Eguchi, and H. Arai, J. Appl. Phys., 79, (1996) 1816.
- [44] Li, J.-F., et al., High-performance nanostructured thermoelectric materials. NPG Asia Mater, 2 (2010) 2152-158.
- [45] T. Tsubota, M. Ohtaki, K. Eguchi, H. Arai, J. Mater. Chem. 7 (1997) 85–90.
- [46] Mikio Ito , Daisuke Furumoto ; J. Alloys Compd. 450 (2008) 517–520.
- [47] Shingo Ohta, Takashi Nomura, Hiromichi Ohta and Kunihiro Koumoto, J. Appl. Phys. 97 (2005) 034106.
- [48] Frank Maldonada and Arvids Stashans, J. Phys. Chem.Solids. 71 (2005) 784-787.
- [49] Xiurong Qua, Wen Wang , Shuchen Lv , Dechang Jia, Solid State Commun. 151 (2011) 332-336.
- [50] Barf, J., T. Walther, and W. Mader, Interface Science, 12 (2004) 213-226.

- [51] Ohtaki, M., Tsubota, T., Eguchi, K., Arai, H., *J. Appl. Phys.* 79 (1996) 1816-1818.
- [52] P. Jood, R.J.Mehta, Y.LZhang, G.Peleckis, X.LWang, R.W.Siegel, T. Borca Tasciuc, S.X.Dou, G.Ramanath, *Nano.Lett.* 11 (2011) 4337–4342.
- [53] K.H. Jung, K.H.Lee, W.S.Seo, S.M.Choi, *Appl.Phys.Lett.* 100 (2012) 253902.
- [54] H. Colder, E.Guilmeau, C.Harnois, S.Marinel, R.Retoux, E.Savary, *J.Eur. Ceram.Soc.* 31 (2011) 2957–2963.
- [55] M. Kazeoka, H. Hiramatsu, W.S. Seo, K. Koumoto, *J. Mater. Res.* 13 (1998) 523–526.
- [56] T. Tsubota, M. Ohtaki, K. Eguchi, H. Arai, *Proceedings of the 16th International conference on Thermoelectrics*, (1997) 240-243.
- [57] X. Liang, *ACS Appl. Mater. Interfaces.* 15 (2015) 7927-7937.

Chapter 2

Experimental Techniques and Characterization Tools

Objectives

This chapter presents a brief outline of description regarding various material processing methods. It comprises of different characterization techniques adopted for the study of physical and thermoelectric properties.

2.1 Introduction

This chapter deals with the experimental methods used for the synthesis of bulk, nano and thin films for thermoelectric applications. Bulk polycrystalline TE materials were synthesized using the solid state reaction method. Bulk nanograined metal oxides by the hydrothermal method and thin films by radio frequency(RF) magnetron sputtering. A detailed procedures for the preparation were given. Along with the different characterization techniques, their working principles were included. The instrument used for measuring the TE properties was also clearly explained.

2.2 Solid state reaction (SSR)

Solid state reactions are solventless processes in which reaction between or within solid reactants to yield a solid product. This is the most widely used method for the synthesis of polycrystalline bulk materials [1]. In SSR method there will be large range of selection of precursor materials like oxides, carbonates etc.. Considering both thermodynamic and kinetic factor this method requires high temperature which is required to produce significant amount of energy to overcome the lattice energy for the inter diffusion of cation or anion with different lattice site. Three important factors that influence the rate of reaction in SSR method.

1. Area of contact between the reacting solids which depends on the total surface area. Surface area greatly increases with decrease in particle size.
2. Rate of nucleation: Nucleation aided by structural similarity between the product and any one of the reactant.
3. Rate of diffusion: Diffusion can be enhanced by the presence of crystal defects such as vacancies.

For the synthesis of bulk TE material, the raw materials used are of high purity (99.9%) ZnO and Dy₂O₃ purchased from Sigma Aldrich. The synthesis of bulk materials were carried out in high temperature PID controlled furnace. Different steps involved in SSR method as follows.

2.2.1 Mixing of raw materials

Stoichiometric proportion of initial precursors were weighed using an electronic balance. The purity of the raw materials should be greater than 99.9% in order to have phase pure compound. The presence of impurities in the raw materials affects the reactivity as well as thermoelectric property of fired ceramics. After the reagents were weighed out in required amounts, they are mixed together with the aid of ethylene glycol for one hour. Ethylene glycol was added in order to obtain a uniform heat distribution. Point to point contact between the particles can be achieved by this process. Mixing can be done through various methods like hand mixing, ball milling etc. Hand mixing of raw materials can be done using agate mortar and pestle. The hand mixed composition was dried for one hour and again powder the sample. During this process particle size can be reduced and lead to pores free compound. The grinding process introduces dislocation and defects in the crystal which enhance the diffusion of ions and accelerate the formation of solid solution.

2.2.2 Calcination

Calcination is a thermal treatment process under controlled temperature in a moderate oxygen atmosphere. It is used to remove the volatile fraction of materials exist in the compound. The calcination process mainly takes place at a temperature much below the melting point of the product material. The process of calcination derives its name from the Latin word ‘calcinare’ (to burn lime) due to its most common application. Calcination causes the constituents to interact by inter diffusion of their ions and hence reduce the

extend of diffusion that must occur during sintering.

2.2.3 Grinding and pelletization

Grinding of the calcined powder helps to homogenize the compositional variations that may still exist or that may arise due to calcination. If grinding was poor, ceramic powder will form large intergranular voids with low density. Poly vinyl alcohol (PVA) will act as the suitable binder for pelletizing the sample. Pelletizing is a measure of structure integrity. In addition, the binder was called upon to contribute and convey numerous properties that were necessary for the effective performance of the fabric. Binder addition can focus the material property such as porosity, density and micro hardness of the product. About 3 mL of PVA was added in to the mixture and allowed to dry. The most advantage of this process is the removal of the binder from the compact without any disruptive effect. Shaping of the powder by dye pressing using hydraulic pelletizer was shown in Fig: 2.1. Pelletizing will increase the surface area of heat contact. Moreover the number of crystallites in contact may be increased by pelletizing the powder sample.



Figure 2.1: Dye and pelletizer for fabricating circular pellets.

2.2.4 Sintering

Sintering is the process of forming a solid mass of material by heat and pressure without melting it. It is a thermal treatment for bonding particles to form solid mass. Sintering process reduces the porosity, increase the strength, ductility and enhance the material property such as electrical, thermal conductivity etc. [2]. After addition of PVA (binder) the powder was allowed to form small pellet which is to be sintered. The main aim of the sintering process is to achieve the density of the compound up to a desired percentage of the theoretical density. During sintering process atoms in the materials diffuse across the boundaries of the particles, fusing the particles together and creating one solid piece.

2.3 Hydrothermal synthesis

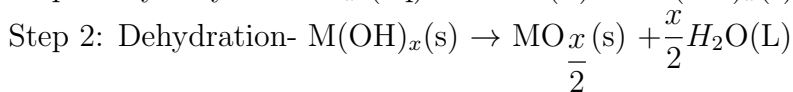
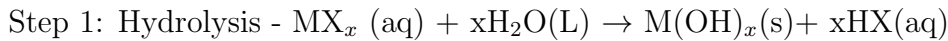
Hydrothermal synthesis is a heterogeneous reaction that crystallize substances in the presence of an aqueous solution under high vapour pressure and temperature [3]. The principle behind this method is that an insoluble material at ambient temperature above the solvent boiling point and at a pressure above 1 bar is allowed to crystallize. The medium used in the solvothermal synthesis include water (hydrothermal), ammonia (ammonothermal), an alcohol, or any organic or inorganic solvent. For the synthesis of inorganic compounds the precursor is often aqueous solutions of simple salts such as metal chlorides, nitrates, or acetates. Depending on the specific synthesis, these can be precipitate to the corresponding metal hydroxides using a base (often NaOH, KOH or NH_4OH). Other additives for pH control, reduction or oxidation, coating etc. can be added desirably prior to the hydrothermal treatment.

2.3.1 Design aspects of an autoclave

The crystal growth is performed in an apparatus consisting of steel pressure vessel called an autoclave in which initial precursors are supplied along with water in a teflon liner. The teflon liner is placed inside the autoclave and tightly sealed. The autoclave should be made out of steel or high temperature alloy vessel whose strength is great enough to sustain pressure-temperature conditions. The material should possess high strength characteristics and corrosion resistance against alkaline and acidic solution. The vessel should be easily assembled and disassembled.

2.3.2 Synthesis mechanism

In 1992 Adschiri et al. suggested the two step formation mechanism for the synthesis of metal oxide particles from a simple metal salt [4].



Here, M denotes the metal and X represents the cation. A temperature gradient is maintained between opposite ends of the growth chamber. The lower dissolving section is isothermally hotter than the upper growth region which is also maintained isothermal. The solution expands and compressed until the pressure inside it reaches very high. Under these high temperature and pressure the material in the lower compartment of the autoclave dissolves in the solution to become a saturated solution. This saturated solution rises due to the convection caused by the temperature difference between the upper and lower compartments of the autoclave. When the solution reaches the upper compartment of the autoclave, it becomes supersaturated and the forward reaction took place resulting in the formation of metal oxide. The intermediate compound M(OH)_x is hard to characterize as the second reaction happens quickly as the hydroxide formed. The intermediate compound is often amorphous and nano sized and it crystallizes depending on the degree of temperature difference.

2.3.3 Advantages of hydrothermal synthesis

1. Compounds with high melting points can be grown at lower temperatures.
2. Materials with a high vapour pressure near their melting points can be grown by the hydrothermal method.
3. Growth of large good-quality crystals while maintaining control over their composition.

2.4 Sputtering

Evaporation caused by absorption of thermal energy is not the only way to induce atoms to leave a liquid or solid surface. Atoms can also be ejected or sputtered from solids at room temperature by bombarding their surfaces with energetic ions. The emitted atoms traverse along a reduced pressure ambient and deposit uniformly on a substrate to form a film. Physical means are primarily involved in producing films and are known as physical vapour deposition (PVD) processes.

Fig: 2.2 depicts a simplified sputtering system capable of depositing films. Inside is a pair of parallel metal electrodes, one of which is the cathode or target of the metal oxide to be deposited. Facing the cathode is the substrate or anode which may be grounded, biased positively or negatively, heated or cooled. After the evacuation of chamber, a working gas typically argon, is introduced and serves as the medium in which an electric discharge is initiated and sustained. Gas pressures usually range from a few to milli bar. After the flow of argon, a visible glow discharge is maintained between the electrodes. It is observed that a current flows, and metal ions from the cathode deposit on the substrate. Microscopically, positive gas ions in the discharge strike the cathode and physically eject or sputter target atoms through momentum transfer to them. These atoms enter and pass through the discharge region to eventually deposit on the growing film. In addition,

other particles (secondary electrons, desorbed gases, and negative ions) as well as radiation (X-rays and photons) are emitted from the target. The electric field accelerates electrons and negatively charged ions move towards the anode substrate where they impinge on the growing film. An ionized gas or plasma, active electrodes that participate in the deposition process, and low temperature processing are the features of sputtering from other PVD process such as evaporation.

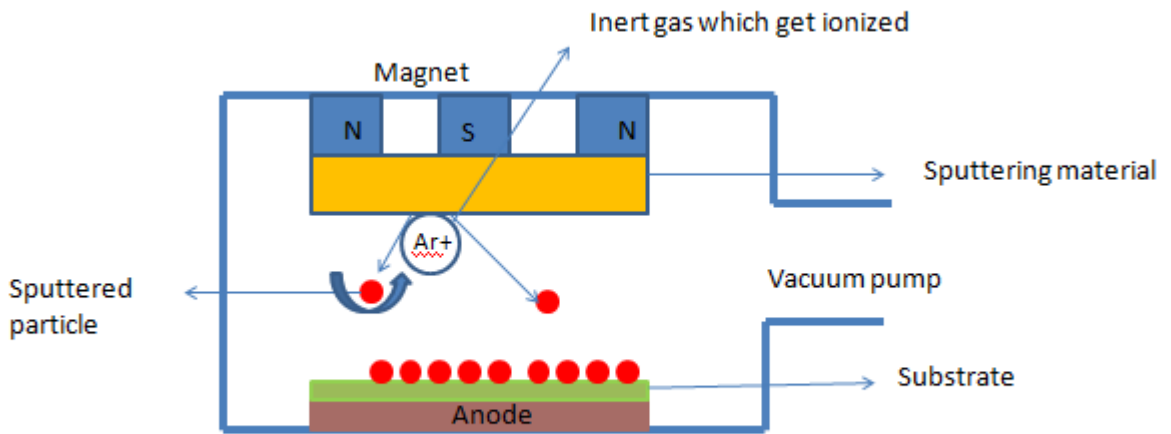


Figure 2.2: Schematic representation of sputtering system.

2.4.1 RF magnetron sputtering

RF magnetron sputtering is a high rate vacuum coating technique for depositing metals, alloys and dielectric materials. Most commonly it is used for coating dielectric materials. The magnetron uses the principle of applying a magnetic field to the cathode surface which form electron traps so that $E \times B$ drift currents close in on themselves. Ionization efficiency of the gas atoms vastly increases and lead to increase in ion current density. Thus the plasma impedance gets lowers and the magnetron source operates at much

lower voltage (500-600 V). When RF power is applied to a target it may capacitively coupled by forming a DC covering over the sputtering cathode. At high frequency ($\approx 13.56\text{MHz}$) ions and electrons have different mobilities in the fluctuating field. An excess electron current is produced due to the difference in mobility and the cathode surface get negatively biased. Due to this reason the sputtering cathode need not be a conductor and can be an insulating material such as ceramic or polymer.

Formation of plasma

A plasma may be broadly defined as quasineutral gas that exhibits a collective behavior in the presence of applied electromagnetic fields. Plasma consist of weakly ionized gases with a collection of electrons, ions, and neutral atomic and molecular species. The process of plasma formation begins when stray of electrons near the cathode carrying an intial current is accelerated towards the anode by the applied electric field. After gaining sufficient energy the electron collides with a neutral gas atom (A) converting it into a positively charged ion. During this impact ionization process, charge conservation indicates that two electrons are released,i.e.,



These electrons are accelerated and bombard with two additional neutral gas atoms, generating more ions and electrons. Meanwhile, the electric field drives ions towards the cathode and results in charge multiplication. The effect snowballs until a sufficiently large avalanche current ultimately causes the gas to breakdown.

A sequence of events took place when an energetic ion reaches the surface. Electron exchange was carried out when they are at angstrom apart. When the ion-solid encounter distance further decreases, the separate atoms of atomic number Z_1 (ion) and Z_2 (surface) evolve into molecular orbits of an unstable quasi molecule and finally into the atomic orbitals of an unstable but united atoms of atomic number $Z_1 + Z_2$. As the encounter distance

shrinks more, electronic repulsion and the Pauli exclusion principle begin to dominate, resulting in atomic separation and collisional reionization of neutrals. This may be viewed as the momentum of collision. During this step several processes are possible depending on the impact and energy of collision. Collision may result for the dissociation of the target molecule, reflection of incoming ions from the target surface and also for the adsorption of low energy ions on the surface [5].

Formation of thin film

Soon after the exposure of the substrate to the incident vapour, a uniform distribution of small but highly mobile clusters or islands was observed. After the continues exposure the island nuclei further incorporate impinging atoms and sub critical clusters are grown in size. The next stage involves merging of the islands by a coalescence phenomenon. The coalescence behaves like liquid at higher substrate temperature. Coalescence decreases the island density resulting in local covering of the substrate where the further nucleation can occur. Crystallographic facets and orientations are frequently preserved on islands and at interfaces between initially disoriented, coalesced particles. Continued coalescence results in the development of a connected network with unfilled channels in between. With further deposition, the channels fill in and shrink leaving isolated voids behind. Finally, voids fill completely and the film is said to be continuous. This sequence of events occurs during the early stages of deposition, typically accounting for the first few hundred angstrom of film thickness. Film formation have pointed to three basic growth modes:(1) Island, (2) Layer (3) Stranski-Krastanov (S-K). Island growth occurs when the stable clusters nucleate on the substrate and grow in three dimensions. This happens when atoms or molecules that are deposited more strongly bound to each other than to the substrate. Metals and semiconductor films deposited on oxide substrates initially form such islands. The opposite characteristics are displayed during the 'layer' growth. During the 'layer' growth, smallest stable nucleus occur in two dimension re-

sulting in the formation of planar sheets. In this growth mode the atoms are more strongly bound to the substrate than to each other. The first complete mono layer is then covered with less tightly bound second layer. The ‘layer’ combined with ‘island’ or Stranski-Krastanov (S-K) growth mechanism is an intermediate combination of the preceding two modes. In this case after forming one or more mono layer, subsequent layer growth becomes unfavorable and islands form. Film growth by the S-K mode is fairly common and has been observed in metal-metal and metal-semiconductors systems.

2.5 Structural characterization

Structural characterization studies were done by X-ray diffraction (XRD) and Raman analysis. Diffraction techniques using electrons, X-rays or neutrons produce information about crystal structure and are used to understand the bravais lattice of bulk materials. Raman analysis helps to determine the vibrational modes present in the molecule.

2.5.1 X-Ray diffraction

X-ray diffraction is an important tool used to reveal the information regarding the crystallinity of the material, nature of the phase present and crystallite size. When X-rays interact with crystalline materials, diffraction pattern will be obtained which is considered to be the fingerprint of that material. The powder diffraction method is thus ideally suited for characterization and identification of polycrystalline phases and it gives an idea about the atomic arrangement within the crystal. The main use of powder diffraction is to identify components in a sample by a search/match procedure. Spacing of planes in a crystal lattice will act as diffraction grating for X-ray wavelength. Diffraction occurs when light is scattered by a periodic array of atoms with long-range order, producing constructive interference at specific angle. Hence, a diffracted beam may be described as a beam composed of a large number of scattered rays mutually reinforcing one another. A beam of

X-rays directed at a crystal interact with the electrons of the atoms in the crystal. The electrons oscillate under the influence of the incoming X-rays and become secondary sources of electromagnetic radiation, which extend to all directions. The waves emitted by the electrons have the same frequency as that of the incoming radiation. The emission can undergo constructive or destructive interference. The strength with which an atom scatters light is proportional to the number of electrons around the atom. Intensity corresponding to each plane thus gives the concentration of atoms or electrons along that plane. There will be X-ray reflections from a series of parallel planes inside the crystal. The orientation and interplanar spacing of these planes are defined by the three integers h, k, l called Miller indices [6]. If

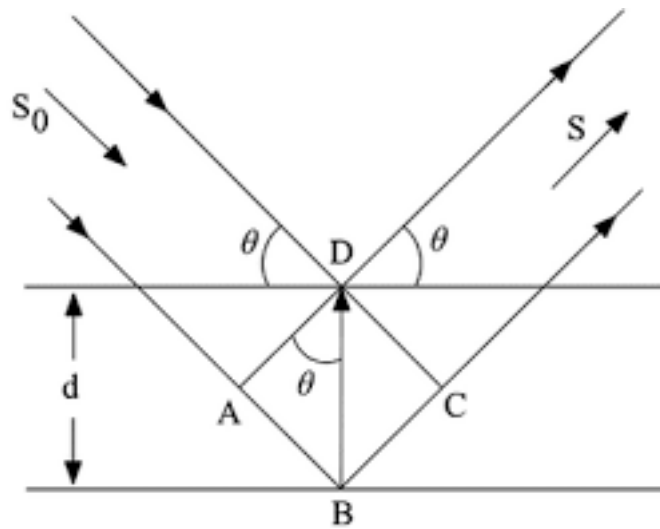


Figure 2.3: Schematic representation of X-ray Diffraction [7].

beams diffracted by two different layers are in phase, constructive interference occurs and the path difference between the two waves should be an integral multiple of wavelength. Bragg's condition for constructive interference can be stated as

$$n\lambda = 2d\sin\theta \quad (2.2)$$

where θ is the angle of incidence, 'n' is an integer which represents the order of the plane, λ is the wavelength and d is the spacing between atomic layers. Since a highly regular structure is needed for diffraction to occur, only crystalline solids will diffract; amorphous materials will not show a definite diffraction pattern.

Instrumentation

A powder X-ray diffractometer consists of an X-ray source, a sample holder, and a detector. X-rays are produced in the cathode ray tube by heating a filament to produce electrons. These electrons were accelerated towards the target by applying a voltage and allowed to bombard with it. When the incident electrons have the sufficient energy to remove the inner most electrons from the target, characteristic X-ray spectra are produced. Copper is the most common target material for single-crystal diffraction which produce Cu-K α radiation with a wavelength 1.54 Å. These X-rays are collimated and directed onto the sample. As the sample and detector gets rotate, the intensity of the diffracted X-rays is recorded. The X-ray is focused on the sample at some angle θ , while the detector opposite to the source reads the intensity of the X-ray at an angle 2θ away from the source path. The average size of the particle can be calculated using the Scherrer equation. Scherrer formula relates the size of submicrometer particle or crystallites in a solid to the broadening of the peak in a diffraction pattern.

$$D = \frac{k\lambda}{\beta \cos\theta} \quad (2.3)$$

where λ is the wavelength, β is the full width at half maximum expressed in radians, θ is the Bragg angle, 'k' is a dimensionless shape factor with value close to unity.

In this work, XRD analysis were performed using Rigaku Miniflex 600 X-ray diffractometer with Cu-K α radiation with a wavelength of 1.54Å from the Department of Physics, University of Calicut. The room temperature XRD measurements were carried out within the 2θ range from 20-80°. The

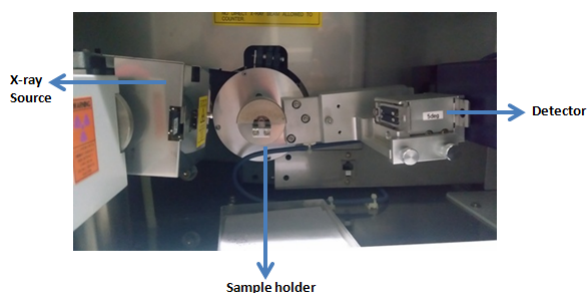


Figure 2.4: X-Ray Diffractometer: Rigaku Miniflex 600 with Bragg-Brentano geometry.

analysis of the XRD pattern was done using PDXL software. The obtained diffraction patterns of the sample are compared with the ICDD (International Centre for Diffraction Data) data base.

2.5.2 Raman spectroscopy

Raman spectroscopy is based on the interaction of photons with molecules that can cause changes in rotational, vibrational, electronic energy states of matter. When photon strike a solid or collection of molecules, most of them

are scattered elastically which is termed to be Rayleigh scattered. Whereas a few undergoes inelastic scattering and that photons will have frequency lower or higher than that of the incident radiation. This phenomenon predicted in 1923 by Smekel and observed by Sir.C.V. Raman in 1928 is referred to as Raman scattering [8].

Theory behind Raman spectrum

Raman spectrum is a spectroscopic technique used to observe vibrational, rotational, and other low-frequency modes in a system. The Raman effect occur when light impinges on a molecule and interacts with the electron cloud and the bonds of that molecule. For the spontaneous Raman Effect, which is a form of light scattering, a photon excites the molecule from the ground state to a virtual energy state. When the molecule relaxes it emits a photon and it returns to a different rotational or vibrational state. The difference in energy between the original state and this new state leads to a shift in the emitted photon's frequency away from the excitation wavelength [9]. If the final vibrational state of the molecule is more energetic than the initial state, the emitted photon will be shifted to a lower frequency for the total energy of the system to remain balanced. This shift in frequency is designated as a Stokes shift in which the molecule absorb energy. If the final vibrational state is less energetic than the initial state, then the emitted photon will be shifted to a higher frequency, and this is designated as an anti-Stokes shift in which the molecule imparts energy to the exciting radiation. Raman scattering is an example of inelastic scattering because of the energy transfer between the photons and the molecules during their interaction. The Raman effect arises when a photon strikes on a molecule and interacts with the electric dipole of the molecule. The dipole moment P , induced in a molecule by an external electric field E , is proportional to the field $P = \alpha E$. If the electric field is oscillating (photon) the dipole moment defined as $P = \alpha E_0 \cos(2\pi\nu_0 t)$. The proportionality constant α termed to be the polarizability of the molecule and ν_0 is the oscillation frequency. The polarizability measures the amount

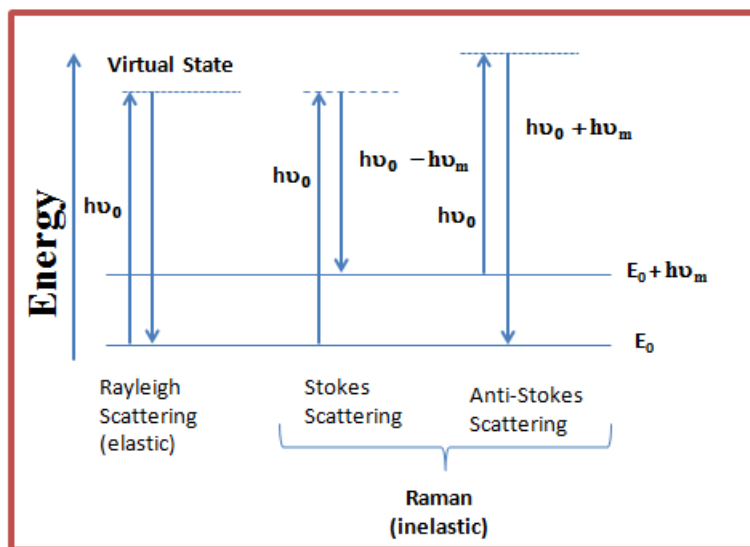


Figure 2.5: Schematic representation of Raman scattering.

at which electron cloud around a molecule can be distorted. If this distortion is anisotropic with the direction, then the polarizability ellipsoid changes and this results in the formation of Raman spectrum. The induced dipole will scatter light at the optical frequency of the incident light wave. Mathematically defined as; $\frac{d\alpha}{dQ} \neq 0$, where Q is the normal coordinate of the vibration [10]. If the molecule possess center of symmertry the change in dipole moment will be zero and the molecule found to be IR inactive whereas due to the change in the polarizability ellipsoid the molecule become Raman active [11]. If the polarizability is isotropic the reradiated incident frequency will be Rayleigh scattered. For anisotropic polarizability the molecule should under goes rotational and vibrational motions and results in the formation of Stoke's and antistoke's line. The scattering intensity is proportional to the square of induced dipole moment i.e., square of polarizability derivative. Quantum mechanical selection rule for Raman spectroscopy can be represented as $\langle v_f | x | v_i \rangle \neq 0; v_f - v_i = \pm 1$ where v_f and v_i represents the final and initial vibrational states during the excitation. The greater the polarizability ellipsoid changes, more intense the Raman scattering.

In this work, Raman measurements were performed on powder samples

using JASCO NRS 4100 employing Nd-Yag laser of wavelength 532 nm. The measured resolution of the spectrometer is 2 cm^{-1} .

2.6 Morphological analysis

In this section the morphology of the samples was analysed using SEM and AFM analysis. SEM employs electrons for imaging the sample surface where as in AFM the force between the tip of the cantilever and the sample surface produce the image.

2.6.1 Scanning electron microscopy

A scanning electron microscope (SEM) is a versatile mode of electron microscope which produce the focused beam of electron for scanning the surface to obtain the 3D image of the specimen. It is most widely used for thin film characterization. In SEM, only a small portion of the total image is probed at any instant and the image builds up serially by scanning the probe. Electrons thermionically emitted from tungsten or LaB_6 (cathode) filament at high temperature (2800 K) are drawn towards the anode by applying a positive voltage (1 to 30 kV). The emitted electrons were focussed by two successive condenser lenses in to a beam with a fine spot size that is typically 10\AA in diameter. Pairs of scanning coils located at the objective lens deflect the beam either linearly or in raster fashion over a rectangular area of specimen surface as shown in Fig: 2.6 [12]. When the accelerated primary electron strikes the sample, it decelerate by losing the energy inelastically to other atomic electrons and to the lattice producing secondary electrons, backscattered electrons and X-rays. Through continuous random scattering events the primary beam effectively spreads and fills a tear drop-shaped interaction volume with a multitude of electronic excitations. This results for the collection of electrons which manage to leave the specimen with a continuos energy [14].

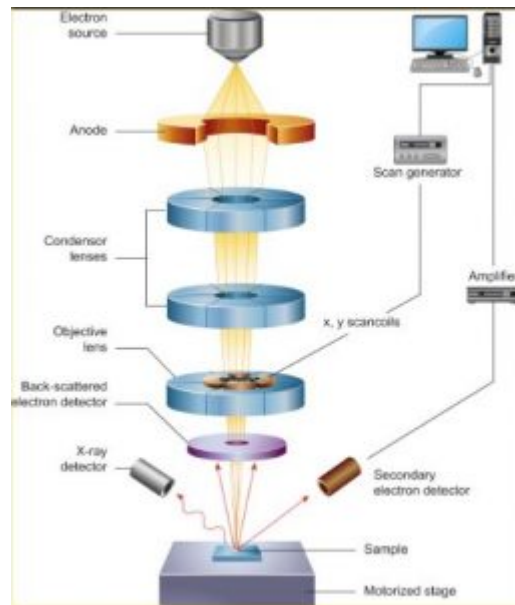


Figure 2.6: Schematic representation of SEM instrument [13].

Secondary electron

The most common imaging mode relies on detection of the lowest portion of the emitted energy distribution. Low energy means they were originate from subsurface depth of several angstroms. The secondary electrons thus produced where collected by the positive charged electron detector consisting of a scintillator/photomultiplier combination. The output serves to modulate the intensity of a CRT which is rastered in synchronism with the raster scanned primary beam. Great depth of focus enables images of beautiful 3-D quality to be obtained from non planar surfaces. These secondary electrons can also be collected using an inlense detector (inside the SEM coloum) other than the photomultiplier.

Backscattered electron

These are the high energy electrons which are elastically scattered and essentially possess the same energy as the incident electron. The probability

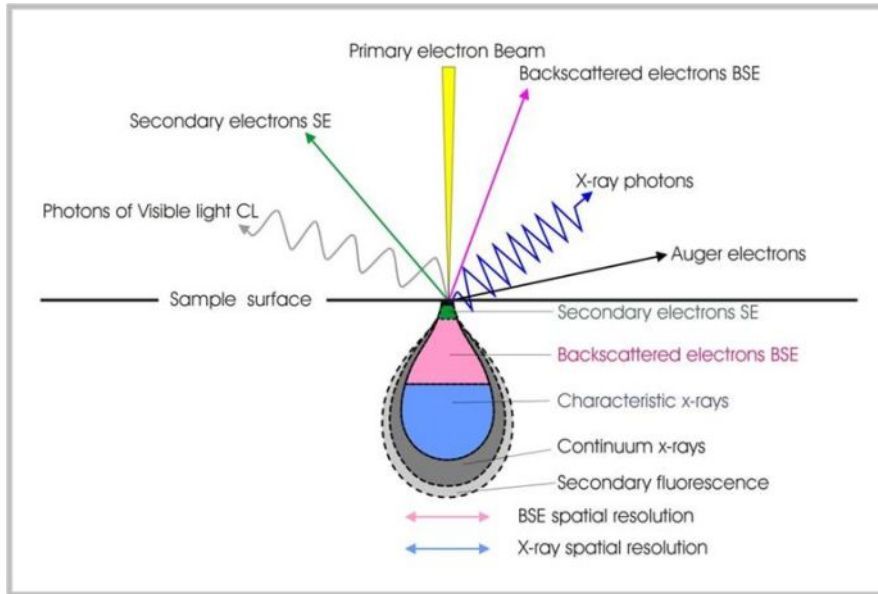


Figure 2.7: Emission of various electron and electromagnetic waves from the specimen [13].

of backscattering increases with the atomic number Z of the sample material. Since the backscattered fraction is not very strong function of Z ($0.05Z^{1/2}$), elemental identification is not feasible. Since the specimen interaction depth for the high energy backscattered electron is much low compared to secondary electrons there will be less topological contrast in the images.

In this work, the surface morphology of the prepared samples was analyzed using FEG Zeiss Supara 55 scanning electron microscope equipped with energy dispersive X-ray analysis (EDAX) technique.

2.6.2 Atomic force microscopy

Atomic force microscopy (AFM) is the most versatile technique for the surface analysis of thin films. AFM employs the force rather than current to image a surface so that all kinds of material surfaces including metals, semi-conductors and insulators are imageable. AFM produce topological features of the surface at extremely high magnification even better than electronic mi-

roscope. The cantilever spring constant K must be smaller than the spring constant K_a that effectively exist between the atoms [15]. When the tip and specimen are widely separated, van der Waals force cause them to weakly attract. But when they are brought too closely, their electron cloud overlap and electrostatic repulsive force physically push them apart. In AFM, probe is allowed to laterally scan across the sample, which interacts through atomic forces depending on the structural features on the surface. The interaction get translated by an optical lever system in which, a laser beam is allowed to focused on one end of the cantilever and reflected on to a photodiode detector. As the cantilever moves in response to the sample topography, the angle of reflection of laser beam on to the photodiode detector changes which is split into four quadrants. The vertical and horizontal deflections on the photodiode were measured using the split photodiode detector and able to produce 3 dimensional images. The displacement of the cantilever along the three directions were obtained using a piezo-electrodes for X,Y and Z directions in a single piezoelectric scanner [16].

Contact mode

The contact mode also known as repulsive mode, the tip actually makes physical contact with the surface, and have forces in the range of 10^{-6} to 10^{-8} N are typically generated. In this mode, the microscope have two modes of operation; either in the constant height mode or in deflection mode. In the constant height mode, the height of the cantilever is kept constant by the means of an electronic feed back mechanism relative to the tip. The system monitors the changes in piezo height. While in deflection mode, the Z-piezo height remains stationary and the variation in the height of the cantilever was obtained from the laser deflection depending on its interaction with the surface. Images produced in the deflection mode are not quantifiable in Z direction, but it can reflect the rapid change in the topography [17].

Tapping mode

This mode is used to image the sample surface which can be easily oxidized or loosely bound to the substrate. The tip slightly touches the sample surface at the end of each swing with a constant oscillation amplitude. To maintain a constant oscillation amplitude a constant oscillation signal should be given according to the signal obtained from the photodiode detector. The scanner have to change its vertical position at each time depending on the topography such that a constant amplitude of oscillation should be produced. The vertical position of the scanner is noted and the image topography can be obtained.

Non-contact mode

In the non-contact mode the cantilever is located tens to hundred angstrom from the specimen surface. To prevent surface contacts a stiff cantilever is used resulting in low-tip specimen forces of $\approx 10^{-12}$ N. Since it is difficult to detect small forces the cantilever is vibrated, typically at 100 to 400 kHz. In NC-AFM, as the tip approaches the sample surface depending on the van der Waals attractive force the position and vibration of cantilever changes. Changes in the vibrational amplitude or resonant frequency are then detected by sensitive AC method, converted to tip-sample spacings and ultimately recorded as surface image [18].

AFM provides a number of advantages over the other microscopic techniques. The surface imaging by an AFM can be made in 3 dimensions; the horizontal X-Y plane and the vertical Z dimension by measuring the force between a sharp probe (10 nm) and surface at different distance magnitude. Resolution/magnification along Z-direction is normally higher than X-Y direction thus enabling valuable information of its topological features at 3 dimension. AFM doesnot need vacuum condition nor any special sample preparation, and they can be used either in an ambient atmosphere or in liquid environment.

2.7 Chemical analysis

In this section, the chemical characterization of the samples was studied using XPS and EDAX analysis. This include identification and composition of elements present in the compound using the electrons or X-rays emitted from the inner shell.

2.7.1 X-ray photoelectron spectroscopy (XPS)

XPS is a photoemission process and a quantitative spectroscopic technique that deals with atomic core electron. It form the basis for the identification of elemental composition, chemical state and electronic state of the elements that exist within the material [19]. Soft X-rays produced from Aluminium ($h\nu_{Al} = 1487eV$) and Magnesium ($h\nu_{Mg} = 1254 eV$) sources are allowed to impinge on the material surface for the creation of a hole or electron vacancy in the inner most shell. This ejected electrons are trapped by detectors and depending upon their binding energy the identification of the elements took place. They are capable of detecting almost all elements in the periodic table. The emitted electron binding energy can be determined by measuring the kinetic energy (E_{KE}) of the electron by employing the photoelectric equation

$$E_b = h\nu - E_{KE} - E_\phi \quad (2.4)$$

where $h\nu$ is the incoming photon energy and E_ϕ is the spectroscopy threshold energy.

A graph representing binding energy versus number of electrons detected where plotted. Corresponding to each binding energy there exist an unique peak corresponding to the elements in the material. Number of electrons that escape from ≈ 0.1 mm of the material being analysed and is directly related to the amount of elements within the area irradiated. The detection limit of XPS ranges about ≈ 0.1 to 1 atomic %. The lateral spatial resolution of ≈ 0.1 mm over which analyses was performed. XPS is capable of readily providing information on the nature of chemical bonding and valence states

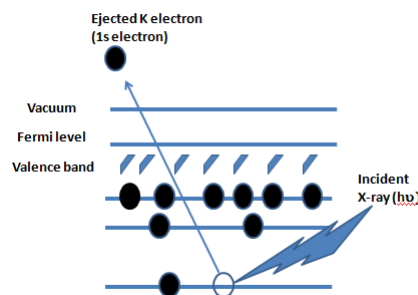


Figure 2.8: Schematic representation of the photoelectron emission.

[20].

X-ray photoelectron core level spectra were measured from IISC, Bangalore using Kratos AXIS ULTRA spectrometer which employs a monochromatic Al-K α X-ray source ($h\nu=1486.58$ eV) which was used at 150W (10mA,15kV). XPS spectra was calibrated by taking the binding energy corresponding to C 1s peak at 285.4 ± 1 eV. Peak fitting was done using Gaussian Lorentzian curve fitting. A reduced “chi square” value below one was obtained for all the peaks which ensured the accuracy of XPS peak fitting. Peaks can be deconvoluted to obtain the information about binding energy, peak areas, full width at half maximum(FWHM), and the atomic concentration.

2.7.2 Energy dispersive X-ray spectroscopy (EDAX)

EDAX is an analytical technique used for the elemental analysis or to determine the chemical characterization of the sample. In EDX, an electron from the outer shell lowers its energy by filling the hole and the remaining energy can be emitted as X-rays. The creation of hole in the inner shell may be due to the excitation caused by the high energy electrons. If the electron transition occurs between L and K shells, K α X-rays are produced. The energy of the emitted X-rays depends on the energy difference between the electron transition. Moreover, the emitted X-rays are the characteristic of the particular atom in the periodic table and it exhibits a unique set of spectral

line. EDX spectrum displayed in a digitized form with x-axis representing the energy of X-rays and the y axis gives the number of counts per channel (intensity). Depending on the line intensity concentration of elements present in the sample can be determined. EDX detect elements with atomic number $Z > 4(\text{Be})$ to $Z < 92 (\text{U})$, not all instruments are equipped with detection of light elements ($Z < 11$). The detection limit of EDX ranging from 0.1 to 1 atomic % and the lateral resolution lies $\approx 1 \mu\text{m}$. EDX equipment is normally occupied with in the SEM instrument. Separate sample preparation is not needed for EDAX analysis [21].

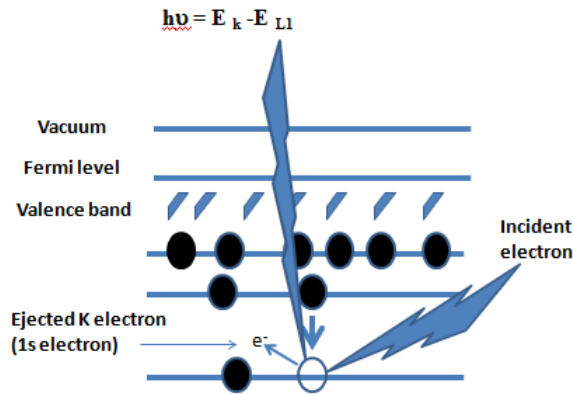


Figure 2.9: Schematic representation of EDAX analysis.

2.8 Optical spectroscopy

2.8.1 UV-Visible spectroscopy

UV-Visible spectroscopy refers to absorption spectroscopy is used to characterize materials by measuring the attenuation of light energy. When a beam of light passes through the sample, it undergoes absorption, transmittance and reflection ($A+T+R = 1$) in the ultraviolet and visible region of the electromagnetic spectrum. It is used to characterize thin films by measuring

the transmittance and absorption of photon whereas, diffuse reflectance was measured for the bulk powder sample.

Diffuse reflectance spectroscopy (DRS)

A part of incident light passes through all angles into the hemisphere of sample surface undergoing refraction, reflection, diffraction and absorption. They oriented in all direction is termed to be diffuse (or volume) reflection and it is in contrast with regular (or directional) reflection from a plane phase boundary. In 1931 Kubelka and Munk proposed a theory assuming that plane-parallel layer of thickness X capable of both scattering and absorbing radiation with a diffuse monochromatic radiation flux I [22]. The layer of thickness X can be split in to infinitesimal layer of thickness dx . The diffuse radiation flux in the negative and positive x directions are designated as I and J respectively as shown in Fig: 2.10. When the beam of light passing through

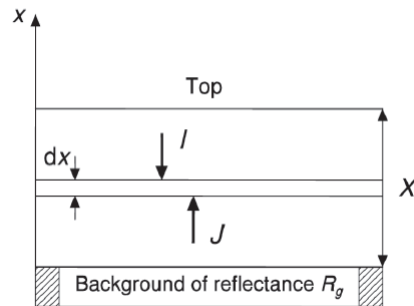


Figure 2.10: Cross sectional diagram of a powder layer.

dx , the downward flux I is decreased by an amount $KI dx$ by absorption and increased by an amount $SI dx$ by scattering. The upward flux can also be defined by the similar argument and thus following differential equation can be given as:

$$-\frac{dI}{dx} = (K - S)I + SJ \quad (2.5)$$

$$\frac{dJ}{dx} = (-K + S)J + SI \quad (2.6)$$

where K and S are absorption and scattering coefficient. By solving this differential equation, a hyperbolic solution can be obtained by introducing a new parameter defined as R which defines the reflectance of the layer over a background of reflectance R_g . Under these condition the reflectance R given by:

$$\frac{K}{S} = \frac{(1 - R)^2}{2R} = F(R) \quad (2.7)$$

where $F(R)$ is usually termed as remission or the Kubelka Munk function [23]. The fundamental absorption, which leads to the generation of electron hole pairs as a result of optical excitation of electrons from the valence band to the conduction band usually occurs in the visible and near ultraviolet spectral region as the band gap energy of most of the semiconductors is in the range of 2-4 eV. For the fundamental absorption to occurs the energy and momentum should be conserved. It is evident that absorption of a photon of visible light doesn't change the momentum of an electron. For the conservation of energy the absorption coefficient α can be defined by

$$\alpha = A \frac{(h\nu - E_g)^n}{h\nu} \quad (2.8)$$

where the E_g represents the band gap energy of the semiconductor and the $h\nu$ represents the energy of incoming radiation. 'A' is a constant independent of wavelength and n has value $1/2$ for direct band gap semiconductor and $n=2$ for the indirect band gap semiconductor.

For the bulk powder sample assuming scattering of photon along the surface is negligible the absorption coefficient α can be obtained from the Kubelka Munk function. The spectral dependence of absorption coefficient must linearize in Tauc coordinates $(\alpha h\nu)^2 - h\nu$ for direct band transition. It is evident that point of intersection with the abscissa axis determines the band gap (E_g) value of the semiconductor.

Transmission spectroscopy

Optical characterization of thin films were studied using the transmission and absorption of incident photon. A beam of light impinging on a flat

polished surface the radiant flux is absorbed according to the well known Lambert absorption law:

$$I = I_0 \exp(-K_T x) \quad (2.9)$$

where I is the radiation flux transmitted when an incident flux I_0 passes through a sample of thickness x with an absorption coefficient K_T measured during transmission. The absorbance can be related to transmittance by the relation:

$$A = -\log(\%T) \quad (2.10)$$

By determining the absorption coefficient from the transmittance spectra the band gap energy E_g can be determined from the Tauc plot relation.

2.9 Electronic property

2.9.1 Hall measurement

Hall effect measurements have been valuable tool for material characterization by determining the electronic properties which was discovered by Edwin Hall in 1879. This potential technique is used to describe the electronic transport properties of a material yielding information on the conductivity/resistivity of materials, type of charge carriers, charge carrier concentration and their mobility. The basic physical principle underlying the Hall effect is the Lorentz force. The combined effect of magnetic field and current through the sample along its length will create an electrical current perpendicular to both the magnetic field and the current. This current in turn creates a transverse voltage termed as Hall voltage. Hall effect measurements are primarily used to determine the Hall voltage (V_H). From the Hall voltage measurements carrier mobility, concentration, resistivity, Hall coefficient and the type of conductivity (n or p type) can be determined.

For the determination of carrier mobility, Hall voltage and the resistivity should be measured. The resistivity can be determined either by four probe



Figure 2.11: Illustration of Hall effect.

terminal method or van der Pauw measurement technique. The measurement configuration for both the measurements is similar, forcing a current through two terminals and determining the voltage across the other two terminals. In the case of Hall voltage there will be a magnetic field perpendicular to the direction of current flow. Fig: 3.2 demonstrate the measurement configuration for these measurements. For van der Pauw resistivity measurements,

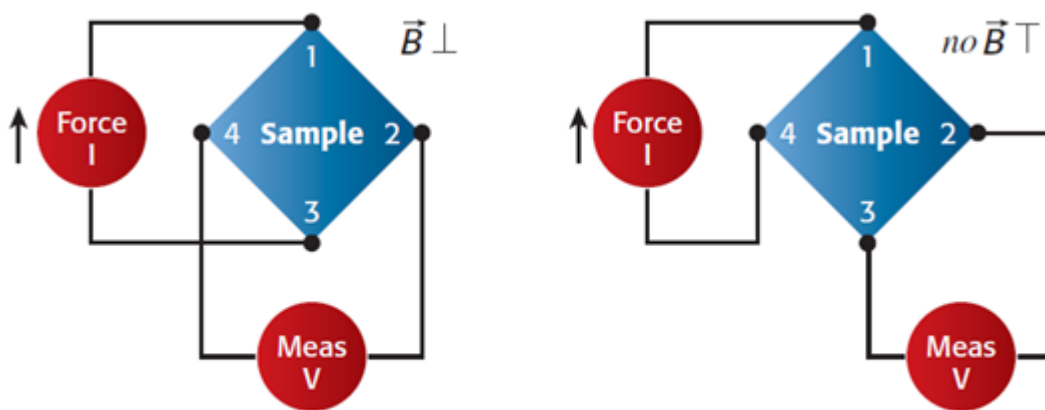


Figure 2.12: Hall voltage measurement using van der Pauw configuration.

the current is forced on adjacent nodes and then the voltage is measured

from opposite adjacent nodes so that everything is being forced and measurements are from the nearest points; in that case, the voltages can be well above 20 millivolts. The voltage range vary from millivolts for low resistivity materials to 100 volts for very high resistivity insulating materials. For van der Pauw measurement magnetic field is not required, whereas for the Hall measurement a transverse magnetic field is applied. The DC electrical properties of both bulk materials and thin film samples were determined by this method. In semiconductors, conductivity is determined by the amount of charge carriers and their mobility. For the resistivity measurements using the van der Pauw geometry the current is send through adjacent contact. This give rise to resistivities $R_{14,23}$ and $R_{12,34}$, which can be expressed as

$$R_{14,23} = \frac{V_{23}}{I_{14}} \quad (2.11)$$

$$R_{12,34} = \frac{V_{34}}{I_{12}} \quad (2.12)$$

and the resistivity is given by the relation,

$$\rho = \frac{\pi t}{\ln(2)} \frac{(R_{14,23} + R_{12,34})}{2} \quad (2.13)$$

The Hall coefficient for electron,

$$R_H = \frac{V_H t}{IB} \quad (2.14)$$

From the Hall coefficient, the carrier concentration can be determined and defined as

$$R_H = \frac{-1}{ne} \quad (2.15)$$

And the carrier mobility as follows

$$\mu = \frac{-\sigma_n V_H t}{IB} \quad (2.16)$$

Here V_H defines the Hall voltage, through a sample of thickness t by passing a current I in an applied magnetic field B . The conductivity σ_n can be obtained from measuring the resistivity ρ . The room temperature Hall measurements for the bulk and the thin film samples were performed using Ecopia HMS-3000 with a constant magnetic field of 0.55 Tesla with varying current.

2.10 Thermoelectric properties

2.10.1 Electrical conductivity and Seebeck coefficient

ULVAC ZEM-3 M8 system is used for the simultaneous measurement of electrical conductivity and Seebeck coefficient of thermo electric materials. The system has an Infrared Gold Image Heating Furnace with excellent temperature control from room temperature to 800⁰C and a microheater for maintaining a temperature gradient. The sample is sandwiched between two electrodes mounted on the upper and lower blocks through which the temperature is applied. The temperature gradient is maintained between the two ends of the sample using the microheater at one end. The measuring thermocouple probes are situated at the lateral side of the sample which is made up of platinum rods. The sample is kept in helium atmosphere at low pressure of 10⁻³ Torr to avoid the oxidation of the sample. Seebeck coefficient



Figure 2.13: Thermoelectric measurement system ULVAC ZEM-3 M8.

is obtained by measuring the induced voltage generated in a material due to a temperature gradient. A square or cylindrical sample is set in a vertical position between the upper and lower blocks in the heating furnace. While the sample is heated and held at a specified temperature, it is further heated by the micro heater at the lower block to provide a temperature gradient. Temperature gradient corresponding to 10, 20, 30⁰C at different base tem-

perature were measured. The sample temperature is stabilized each time to measure Seebeck coefficient and specific resistance value. Before taking the measurement, the samples were preheated from RT to 700 °C for 2 cycles by using the helium purged infrared furnace. The determination of resistance value after each heating cycle indicates the stability of the measuring parameters. Seebeck coefficient is determined by measuring thermal electromotive force (dE) between the thermocouple corresponding to a temperature gradient at a constant temperature. A schematic diagram of the thermoelectric measurement system (ULVAC-ZEM3) is shown in Fig: 2.14.

The Seebeck coefficient S defined as;

$$S = \frac{dE}{T_2 - T_1} \quad (2.17)$$

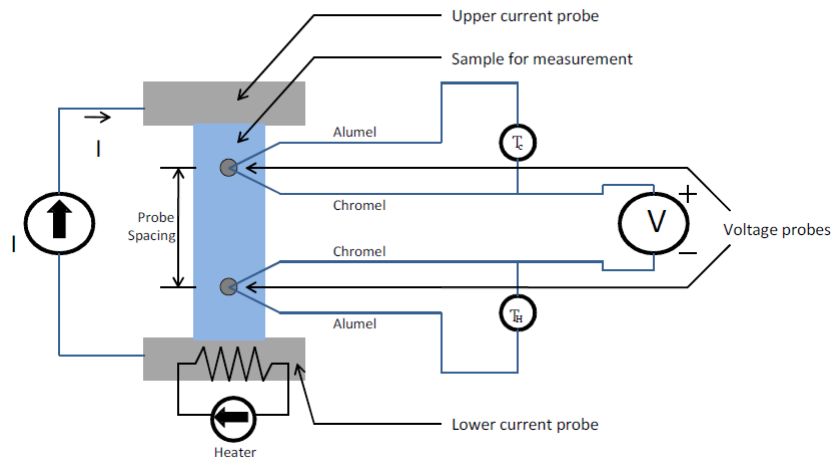


Figure 2.14: Schematic representation of measurement in ULVAC-ZEM 3 M8 system.

Electric resistance is measured by the dc four terminal method, in which a constant current I is applied to both ends of the sample. To measure and to determine voltage drop dV between the wires of the thermocouple by subtracting the thermo-electromotive force between leads and the resistance

defined as:

$$R = \frac{dV}{I} \quad (2.18)$$

V-I plot measurement is made to judge whether there is a proper contact between the probe and the sample. Measurements are computer controlled and performed per temperature difference at the specified temperatures which eliminates dark electromotive force and allows automatic measurements.

2.10.2 Thermal conductivity measurement

Thermal conductivity is an important parameter of thermoelectric material which affects the value of figure of merit defined as $ZT = (S^2 * \sigma / \kappa) T$, where S is the Seebeck coefficient, σ is the electrical conductivity and κ is the thermal conductivity. Thermal Conductivity (κ) is the property of materials ability to conduct heat. It predicts the rate of energy loss through a material and it is usually measured in $\text{Wm}^{-1}\text{K}^{-1}$. For the transport of heat, carriers are necessary. In gases and liquids the molecules themselves are carriers where as in solids the carriers are phonons and electrons [24]. The thermal conductivity of the material was measured by divided bar method (steady state) using rectangular bar shaped pellets ($10 \times 3 \times 1 \text{ mm}^3$) made under high pressure and measured in an inert atmosphere. The temperature gradient is maintained in the sample and the temperature is recorded using the standard copper constantan thermocouple. In this method the sample is sandwiched between two metal blocks and the cross section of the sample should be the same as the area of the metal block which it holds. Heat provided from one end of the block passes through the sample and reaches the other end of the second block. Conditions are controlled until a steady state is attained. The temperature at A,B,C,D are to be measured as shown in Fig: 2.15. Extrapolation of the lines AB and DC to the crystal metal interfaces allows us to determine the thermal gradient in the sample as shown in Fig: 2.16. The entire apparatus should be kept in a chamber and heat lost by radiation

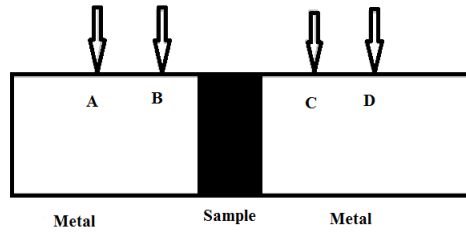


Figure 2.15: Schematic representation of divided bar method to determine the thermal conductivity.

is assumed to be negligible, then

$$\kappa_m A \left(\frac{dT}{dx} \right)_m = \kappa_s A \left(\frac{dT}{dx} \right)_s \quad (2.19)$$

$$\kappa_s = \kappa_m (dT/dx)_m / (dT/dx)_s \quad (2.20)$$

where κ_m and κ_s represents the thermal conductivity of the metal and

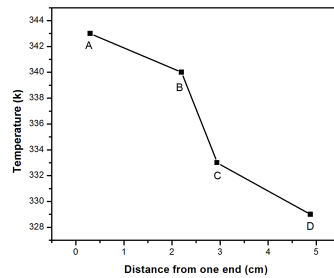


Figure 2.16: Temperature Vs distance from the heating end.

sample respectively. 'A' is the area of the sample and $(dT/dx)_s$ represents the temperature gradient developed between the sample or measured between B and C points in the graph.

References

- [1] G. W. Cave, C. L. Raston, J. L. Scott, Chem. Commun. (2001) 2159.
- [2] M. Braginsky, INT J SOLIDS STRUCT , 42 (2004) 621-636.
- [3] Yoshimura M, Byrappa K, J. Mater. Sci. 43 (2008) 2085-2103.
- [4] Adschiri, T, Kanzawa, K., Arai, K., J.Am. Ceram. Soc. 75 (1992) 1019-1022.
- [5] Milton Ohring, Materials Science of Thin films Deposition and structure, Academic Press (2002).
- [6] B.D Cullity, Elements of X-ray Diffraction, (1956).
- [7] JI Langford, AJC Wilson, J. Appl. Crystllogr, 11 (1978) 102-113.
- [8] Molecular structure and spectroscopy, G Aruldas, (2007).
- [9] Harris, D.C., Bertolucci, M.D., Symmetry and spectroscopy:An introduction to vibrational and electronic spectroscopy, Oxford University Press (1978).
- [10] Carey, P.R., Biochemical Applications of Raman and Resonance Raman Spectroscopies, Academic Press (1982).

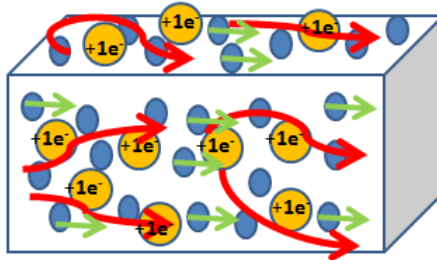
- [11] Herzberg, G, *Molecular Spectra and Molecular Structure II: Infrared and Raman Spectra of Polyatomic Molecules*, Krieger Publishing (1991).
- [12] M. Watt, *The principle and practise of electron microscopy*. Cambridge Uni. Press, Cambridge,(1997).
- [13] Hofmann & Andreas, *Principles and Techniques of Biochemistry and Molecular Biology*, Cambridge University Press, (2010).
- [14] D. K.Schroder, *Semiconductor material and device characterization*. Wiley Interscience, New York, (1998).
- [15] G. Binnig, C. F. Quate, and C. Gerber, *Phys. Rev. Lett.* 56 (1986) 930.
- [16] F. Giessibl, “Advances in atomic force microscopy” , *Reviews of Modern Physics*, 75 (2003) 949-983.
- [17] Y.Martin and H.K Wickramasinghe, *Appl. Phys. Lett.* 50 (1987) 1455.
- [18] S. Kitamura and M. Iwatsuki, *Jpn. J. Appl. Phys.* 34 (1995) L145.
- [19] L. C. Feldman and J. W. Mayer, *Fundamentals of Surface and Thin-Film Analysis*. North-Holland, New York, (1986).
- [20] D. Briggs and M. P. Seah, eds., *Practical Surface Analysis by Auger and X-Ray Photoelectron Spectroscopy*. J. Wiley & Sons, Chichester, U.K. (1983).
- [21] J. B. Wachtman, *Characterization of Materials*. Butterworth—Heinemann, Boston, (1993).
- [22] Kubelka, P., Part I. *J. Opt.Soc. Am.* 38 (1948) 448–460.

- [23] Wyszecki, G., and W.S. Stiles., Color science: Concepts and methods, quantitative data and formulae. 2nd ed. John Wiley & Sons, New York (1982).
- [24] G. Mahan, B. Sales, and J. Sharp, Phys. Today. 50 (1997) 42.

Chapter 3

Thermoelectric Property of Dy ion Doped ZnO Microstructures

Objectives



This chapter presents a brief outline about the thermoelectric properties of Dysprosium (Dy) ion doped Zinc oxide (ZnO). Introduction of donor ion, increases the carrier concentration and reduces the lattice thermal conductivity which leads to the improved TE efficiency.

3.1 Introduction

In this chapter we are dealing with bulk micro structures for thermoelectric application. The existing global scenario demand for the energy production, conservation and management and this intensify the use of thermoelectric(TE) materials, which emerge as an alternative tool for primary power generation and energy conservation (ie; waste heat harvesting). During the infant stage of TE progress the layered micro structures were largely examined for high temperature applications. The question of how thermoelectric materials quench the energy thirst depends on the efficiency of thermoelectric module. Thermoelectric modules are solid state device that can directly convert a temperature gradient to electric energy. For power generation the efficiency of a TE material relay on the following relation:

$$\eta = \frac{\Delta T}{T_{hot}} \frac{\sqrt{1 + ZT_{avg}} - 1}{\sqrt{1 + ZT_{avg}} + T_{cold}/T_{hot}} \quad (3.1)$$

where ΔT is the temperature gradient created by the T_{hot} and T_{cold} part of the TE module and the value of ZT_{avg} varies with the value of T_{avg} [1]. The efficiency directly depends on how large the temperature gradient created between the source and the sink and also on the thermoelectric figure of merit ZT . The risk of obtaining high ZT value lies in the regime of material parameters such as Seebeck coefficient S (Thermopower), electrical conductivity σ and thermal conductivity κ . The possible two approaches for upgrading the ZT value is either the power factor ($S^2\sigma$) ought to be maximized or the thermal conductivity should be reduced. The power factor can be intensified through various mechanisms including i) increment in carrier concentration ii) boost of density of states near the Fermi level and by iii) energy filtering. Seebeck coefficient and electrical conductivity depends on the electronic density of states near the Fermi level, carrier concentration and band structure. Thermal conductivity varies by energy filtering and these transport properties are interdependent and not independently controllable [2]. Through this chapter we are focusing on the enhancement of ZT through increase in carrier concentration and by energy filtering. The classical kinetic theory provides

a good approximation for the lattice thermal conductivity defined as:

$$\kappa_{ph} = 1/3C_vvl \quad (3.2)$$

where C_v is the specific heat at constant volume, l gives the mean free path for phonon and electron and v defines the velocity of sound in the crystalline material. Above Debye temperature, C_v approaches the classical value of $3R$ and κ_{ph} ultimately depend on the value of l which is determined by the phonon-phonon, phonon-electron and phonon-impurity scattering. At higher temperature, the introduction of point defects and impurity ions in the host lattice predominate phonon-electron scattering and can be chosen as a best way for thermal conductivity reduction. Among the oxide materials ZnO arose as a promising n type thermoelectric material having a large exciton binding energy of 60 meV made it useful for optoelectronic applications [3]. The strong correlation between the electrical and thermal conductivity limits oxides for the application of good TE material. However, possibility of tuned band gap and freedom for electrons to move along the empty 4s and 2p orbital's of Zn and O made it a valuable candidate for TE application [4]. With the increase in doping concentration the band filling occurs and the Fermi level lifts towards the lower portion of the conduction band by remodeling the apparent band gap in the material. The effective mass related to the curvature of the bands gets modified due to the distortion in the lattice structure and the band gets flattened. Band flattening contribute for the increase in density of states in the vicinity of Fermi level [5]. In this chapter, the emphasis given to the thermoelectric performance of Lanthanide Dy^{3+} ion doped ZnO matrix with an aim of improving the electrical conductivity using donor electrons. Dy ions can bring about various local lattice distortions in the host matrix; i) due to their larger size ($r_a=0.235$ nm) than Zn($r_a = 0.139$ nm) and the ii) localized magnetic moment [6] which act as an impurity site for scattering of phonons and thereby cause a reduction in the lattice thermal conductivity.

3.2 Synthesis of microstructures

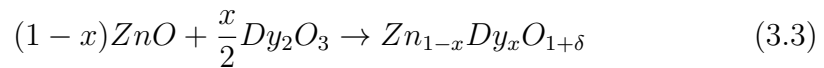
Solid state reaction method was followed for the synthesis of microstructures. Atomic concentration of 0, 0.1, 0.2 and 0.3 % Dy doped ZnO samples were prepared using single oxide powder of ZnO and Dy₂O₃ (Sigma Aldrich) having 99.9% purity and named as S₁, S₂, S₃ and S₄ respectively. The mixed powder was ball milled for 5 hrs at a rpm of 350 and the obtained solid solution was calcined at 500⁰C for 2 hrs in order to remove the volatile impurities. The resultant powder was pressed in to circular pellets of 10 mm diameter with 1 mm thickness using hydraulic pelletizer with a pressure of about 100 bar. The fabricated pellets were sintered at 1300 ⁰C in a programmable sintering furnace for 5 hrs with a heating rate of 10⁰C/min. The compacted pellets were further annealed at 700⁰C in the helium atmosphere in order to homogenize the measuring condition. These pellets and powder were used for the structural and TE characterization.

3.3 Results and discussion

3.3.1 XRD analysis

The XRD patterns of sintered Dy doped ZnO samples at room temperature were shown in Fig: 3.1.

The solid state reaction corresponding to the synthesis can be represented as:



The XRD characterization was performed using Cu-K α radiation of wavelength 1.54 Å at 40 kV and 15 mA with a scanning speed of 10⁰/min having a step size of 0.02⁰ collected in a range 20 to 80⁰ at 2 θ angle. The diffracted X-rays from different planes were indexed according to the standard XRD patterns of the bulk ZnO using ICDD Card No: 00-005-0664 and no impurity peaks were detected in the sintered sample. The XRD peaks revealed the crystallinity of the ZnO samples having hexagonal wurtzite structure with

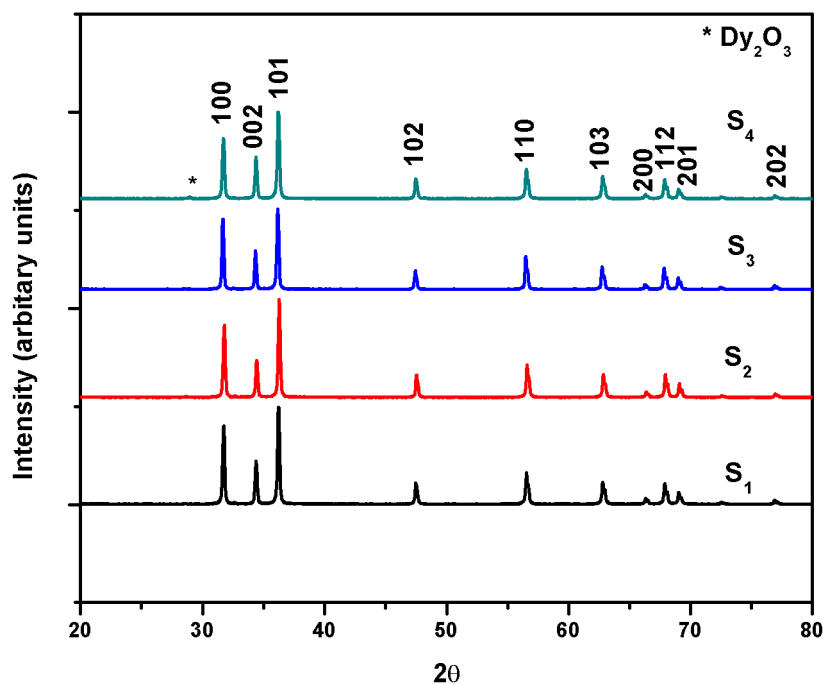


Figure 3.1: XRD pattern corresponding to pure and Dy doped ZnO.

$P6_3mc$ space group. Shift in the peak position towards higher 2θ ensured the presence of Dy ions and the micro lattice strain in residual host matrix. As the doping concentration increases the average crystallite size decreases due to the strain induced in the lattice up to a solubility limit of 0.2 atomic %. Further incorporation of Dy ion results in the formation of (222) plane at 28.91° corresponding to the segregation of Dy_2O_3 at the grain boundaries and leads to the relaxation of lattice planes. Among the lanthanide series Dy ion hold a smaller radius due to lanthanide contraction and similar reports corresponding to lanthanide doping were published in various literature. N.K Divya et al. reported the decrement in the particle size with Nd doping in ZnO lattice and also reported the shift in 2θ due to the strain imposed in the lattice [7]. Bhatia S et al. pointed out the incorporation of Er in ZnO lattice with a modified cell volume and a small shift in 2θ to higher angle depicts the variation in lattice parameters [8]. Fig: 3.2 represents shift in the XRD peak corresponding to 101 plane by the incorporation of Dy ion in Zn

atomic site. Peak shifted towards the higher angle side indicates the increase in lattice strain due to the higher electron affinity of Dy ion. Variation in crystallite size and strain in the lattice were given in Table: 3.1. At the optimum incorporation of dopants, the peak shifts towards the lower angle representing the relaxation of the lattice. Using the Williamson-Hall plot

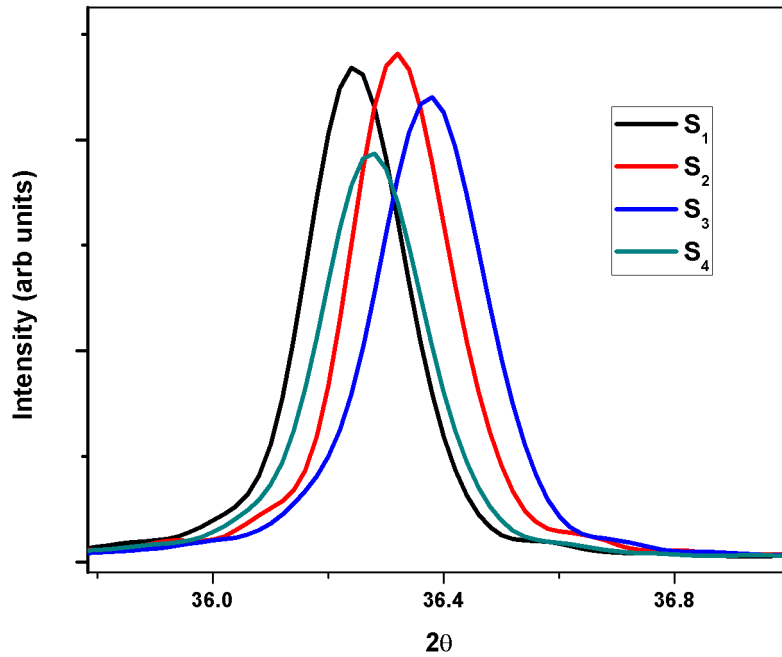


Figure 3.2: Shift observed for the peak corresponding to (101) plane.

analysis as depicted in equation: 3.4 the peak broadening can be explained as:

$$\beta \cos \theta = 4 \varepsilon \sin \theta + \frac{K \lambda}{L} \quad (3.4)$$

where β represents the integral width of the XRD peak corresponding to different planes. The peak broadening arose due to the presence of micro strain ε in the lattice and by the crystallite size L . K represents the dimensionless shape parameter and the λ corresponds to the wavelength of Cu-K α radiation that raster over the lattice through a diffracting angle θ . The residual lattice micro strain induced by the dopants and the average crystallite size were extracted from the slope and y intercept of the straight line fit represented in

Table 3.1: The crystallite size and micro strain corresponding to (101) plane with varying the Dy concentration in ZnO

Sample	Crystallite size L (nm)	Strain ε (10^{-4})
S ₁	51.333 \pm 0.003	-1.12
S ₂	50.580 \pm 0.004	-1.91
S ₃	39.600 \pm 0.004	-3.30
S ₄	49.141 \pm 0.002	-0.40

equation: 3.4. The negative slope in W-H plot depicts the compressive nature of the bonds. Compressive strain shortens the bond distance and leads to lattice contraction which pays the way for reduced cell volume [9].

3.3.2 Raman analysis

The Raman spectra analysis was performed in order to determine the vibrational modes present in pure and Dy ion doped ZnO. Raman spectrum was obtained using Jasco NRS 4100 equipment employing Nd-Yag laser of wavelength 532 nm with a resolution of 2 cm^{-1} . The wurtzite ZnO belongs to $P6_3mc$ space group with two formula units in the primitive cell and all the atoms occupy the C_{3V} sites having the symmetry elements E , C_3 and σ_V . Four atoms in the primitive cell of ZnO lead to 12 phonon branches with 9 optical and 3 acoustic modes. At the center of the Brillouin zone (Γ) the group theory predicts the following lattice optical phonons with irreducible representation [10]:

$$\Gamma_{opt} = 1A_1 + 2B_1 + 1E_1 + 2E_2 \quad (3.5)$$

The phonons of the A_1 and E_1 symmetry are polar and hence exhibit different frequencies for the transverse (TO) and longitudinal optical (LO). They are both infrared and Raman active, while the E_2 mode is nonpolar and they are Raman active only. Non polar phonon modes with symmetry E_2 have

two frequencies, E_2 (high) is associated with oxygen atoms and E_2 (low) is associated with the motion of Zn sub lattice respectively. B_1 mode is optically inactive. Fig: 3.3 represents the room temperature Raman spectrum.

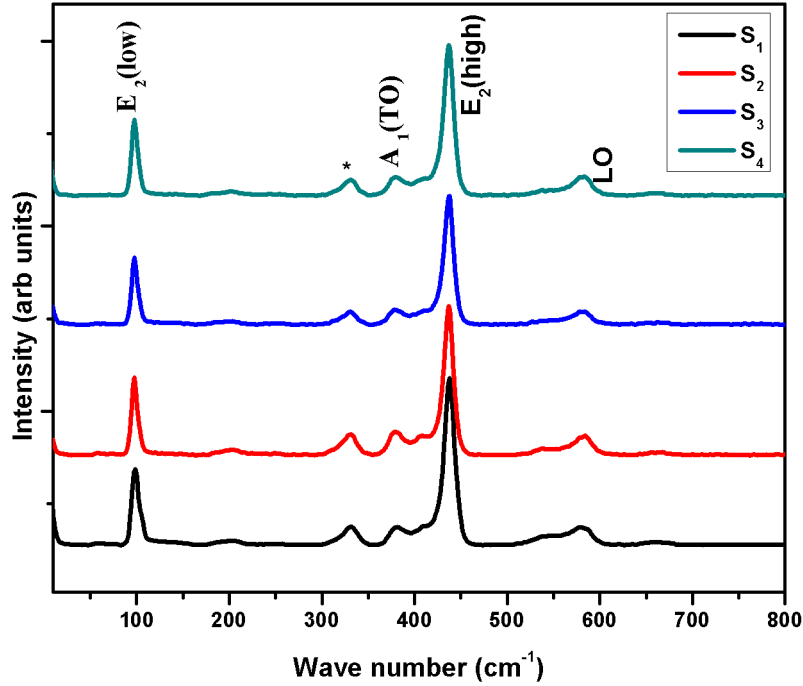


Figure 3.3: Raman spectra for the pure and Dy doped ZnO.

The characteristic Raman peaks at 99 cm^{-1} and 437 cm^{-1} corresponds to the $E_2(\text{low})$ and $E_2(\text{high})$ phonon modes. If the direction of incident and scattered light is perpendicular to the ZnO c axis, transverse optical modes are allowed. The A_1 (TO) mode at 378 cm^{-1} and E_1 (TO) mode occurs at 410 cm^{-1} . Peak arose at 332 cm^{-1} can be assigned due to the second order Raman process and can be obtained from the difference of E_2 (high)- $E_2(\text{low})$ phonon mode considering the symmetry and temperature dependent intensity analysis [11]. The most obvious difference between the spectra for the defect induced crystal and pure ZnO spectrum occurs between $500\text{-}600 \text{ cm}^{-1}$. In this region due to high phonon density, the LO phonon mode intensity strongly depends on the presence of impurities and intrinsic defects [12]. The band is therefore attributed to disorder-induced Raman bands, resulting in

intensity enhanced LO phonon modes especially $E_1(\text{LO})$, due to the disorder induced Raman scattering. Dy ions in the host lattice act as an impurity site for the scattering of phonons and thus phonon contribution arose outside the brillioun zone center. As shown in Fig: 3.4 for the Dy doped ZnO sample a shoulder peak arise near the $A_1(\text{LO})$ which can be assigned to $E_1(\text{LO})$ phonon mode. $E_1(\text{LO})$ mode at 584 cm^{-1} corresponds to the disorder induced band which corresponds to the reduction of crystal symmetry. Distinct $A_1(\text{LO})$ and $E_1(\text{LO})$ modes at 578 and 584 cm^{-1} was observed for the Dy doped ZnO matrix where as for the pure ZnO, combined phonon mode at 579 cm^{-1} was observed.

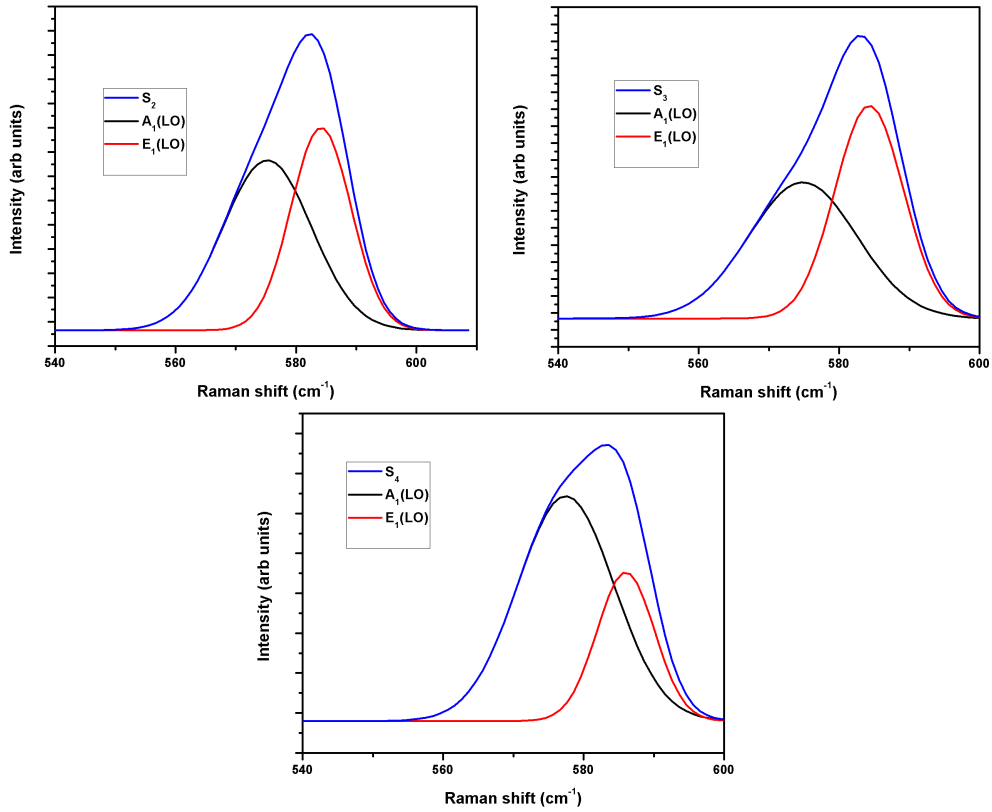


Figure 3.4: Raman spectrum representing the A_1 and E_1 LO modes.

3.3.3 Morphological analysis

The surface morphology and the chemical composition of the samples were determined using SEM and EADX technique. The samples were coated with Au ion in order to produce proper electrical conduction. EDAX analysis confirmed the presence of Dy ion in the sample and the composition was ensured. The final products of each prepared composition resulted in the formation of larger grains since they are formed at high temperature. Fig: 3.5 shows the SEM micrographs with energy dispersive spectra along with it. As expected, larger micro structured grains are formed with irregular size, shape and distribution. The size of the particles varies from 3 μm to 6 μm . The presence of larger grains in the lattice results in the easy conduction of heat waves and there will not have a noticeable reduction in the lattice thermal conductivity. The reduction of lattice thermal conductivity for the doped samples compared to the pristine ZnO is due to the scattering of phonon modes at the impurity site. EDS analysis confirms the presence of constituents in the compound and confirmed the absence of other impurity phases. The EDS results are in agreement with the amount of components in the composition with the stiochiometric proportion used for the synthesis of the compounds.

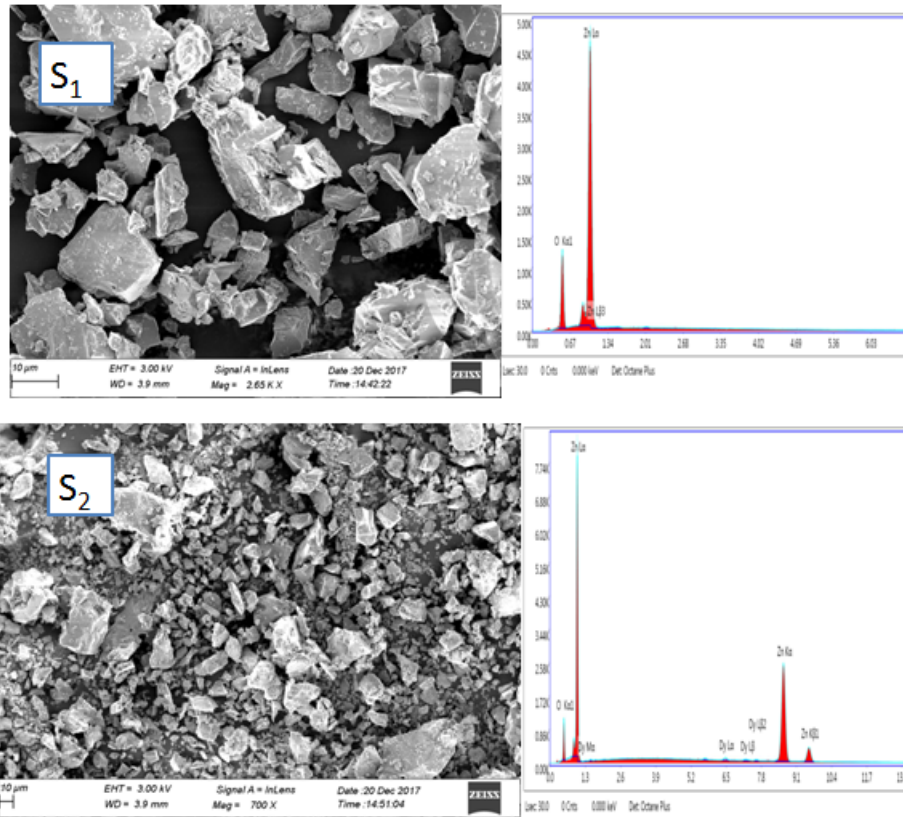
3.3.4 Optical studies

UV-Visible spectroscopy

The UV-Visible spectroscopy studies were performed in order to determine the apparent optical band gap of the material. The optical band gap energy of Dy doped ZnO is determined using the Tauc plot relation:

$$\alpha = \frac{C(h\nu - E_g)^{1/2}}{h\nu} \quad (3.6)$$

where $h\nu$ is the photon energy (eV), E_g is the optical band gap (eV) of the material and C is a constant [13]. The band gap energy of the compounds were estimated by plotting the modified Kubelka Munk function $(\alpha h\nu)^2$ against



$h\nu$ (eV) with and without the inclusion of Dy dopant, as shown in Fig: 3.6.

The absorption coefficient α is defined to be; $\alpha = (1-R)^2/2R$, where R is the diffused reflectance. The direct band gap is determined by extrapolating and intersecting the linear portion of $(\alpha h\nu)^2$ to energy axis ie; the extrapolation of absorption edge to zero absorption. Fig: 3.6 clearly pictures that the Dysprosium doping widens the band gap energy by an order of magnitude 0.03eV. Increment in the band gap energy can be ascertained due to the apparent shifting of Fermi level defined as Burstein Moss shift [13]. As obtained from the transport properties, Dy doped ZnO could be designated as degenerate and the Fermi level lies above the conduction band edge. The optical excitation of the electron takes place from the top most valence band to the Fermi level that lies above the conduction band results in the increment of apparent optical band gap energy.

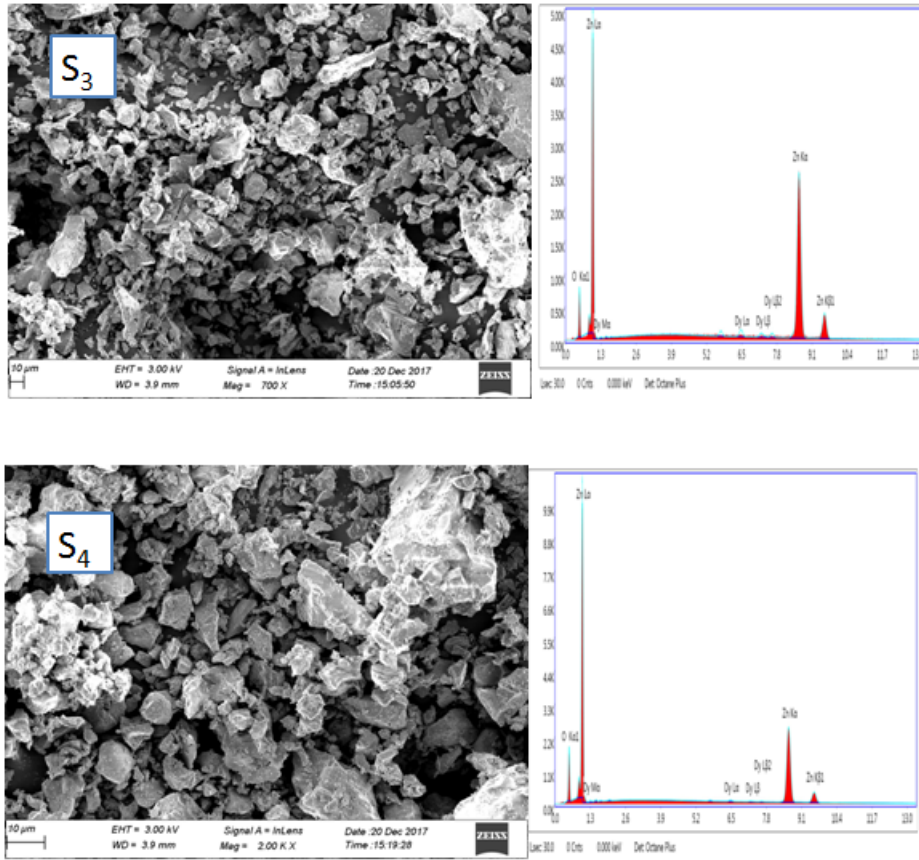


Figure 3.5: SEM and EDAX corresponding to pure and Dy doped ZnO.

3.3.5 Electrical properties

The carrier concentration n_e , hall mobility μ_H and conductivity of pure and Dy doped ZnO samples at 300 K under a magnetic field of 0.55 T and a current of 0.5 mA were shown in Table: 3.2.

Carrier concentration gets enhanced with Dy doping which having more valence electrons than zinc atom. Doping of Dy ions gets saturated at 0.2 atomic % and on further addition the electrical conductivity reduced drastically. The results illustrate that at 0.3 atomic % limited number of carriers contributes for the electrical conductivity and the mobility decreases significantly due to the formation of extra phases which act as electron scattering centers with Dy doping. Similar results for electrical conductivity and carrier

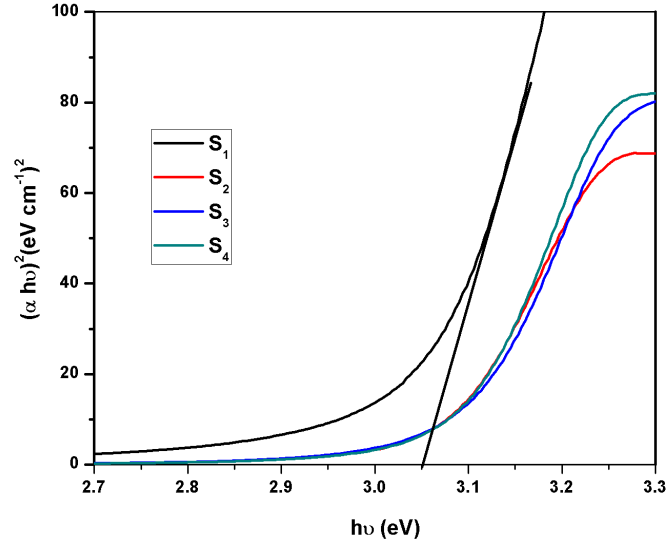


Figure 3.6: Kubelka Munk function Vs $h\nu$ for pure and Dy doped ZnO.

Table 3.2: Variation of electrical characteristics for pure and Dy doped ZnO

Sample	Concentration (cm^{-3})	Mobility (cm^2/Vs)	Conductivity ($\Omega^{-1}\text{cm}^{-1}$)
S ₁	-9.43×10^{10}	47.79	7.22×10^{-7}
S ₂	-2.65×10^{11}	41.53	1.76×10^{-6}
S ₃	-1.84×10^{12}	0.07	2.17×10^{-8}
S ₄	-1.79×10^{12}	0.03	8.66×10^{-9}

concentration were reported by Ajimsha et al. in which the carrier concentration for the Dy doped ZnO thin films increased drastically from $6 \times 10^{18} \text{cm}^{-3}$ to $3.1 \times 10^{20} \text{cm}^{-3}$ with increasing Dy concentration up to ≈ 0.45 atomic % and it reduced gradually to $3.6 \times 10^{19} \text{cm}^{-3}$ at higher Dy concentration due to the formation of acceptor defects [14].

3.3.6 Thermoelectric properties

Electrical conductivity

All the Dy doped samples demonstrate larger electrical conductivity compared to the undoped ZnO and it is plotted in Fig: 3.7. The largest electrical conductivity of about 2500 Sm^{-1} was reported for the S₂ sample at 373 K which is almost 1000 times larger than pristine ZnO. There occurs a hike in electrical conductivity at 373 K and drastically reduced above that particular temperature. Further increase in temperature cause increment in electrical conductivity to a constant value yet higher than pristine ZnO. K.Park et al. reported the increase in electrical conductivity for the Dy doped ZnO nano crystals due to the increment in electron concentration and the value ranges from 2040 to $9780 \text{ } \Omega^{-1}\text{m}^{-1}$ for the pure to 1 atomic % Dy doped ZnO at 800 °C [15]. According to Fermi Dirac statistics the electrical conductivity of a semiconductor material is defined as:

$$\sigma = ne\mu \quad (3.7)$$

where n is the density of electron in the conduction band of a semiconductor and μ gives the mobility. Carrier concentration depends on the density of states near the Fermi level ($g(\varepsilon)$) and the Fermi distribution function $f(\varepsilon)$ described as follows: $n(\varepsilon) = \int_0^{\varepsilon_f} g(\varepsilon)f(\varepsilon)d\varepsilon$. The Fermi energy level determines the charge carrier population over the density of states. For an extrinsic n type semiconductor material charge carrier concentration N_0 is as follows:

$$N_0 = \left(\frac{2\pi kTm_e^*}{\hbar}\right) \exp\left(\frac{-(E_c - E_F)}{kT}\right) \quad (3.8)$$

Where N_0 depends on effective mass m_e^* , temperature and the difference in energy between the Fermi level and the conduction band. In heavily doped semiconductors, the donor electrons occupy states at the bottom of the conduction band. As the electron density increases Fermi energy level get raised and go closer to the conduction band. As the Dysprosium ion get substituted instead of Zn^{2+} , free electrons from Dy will occupy the conduction

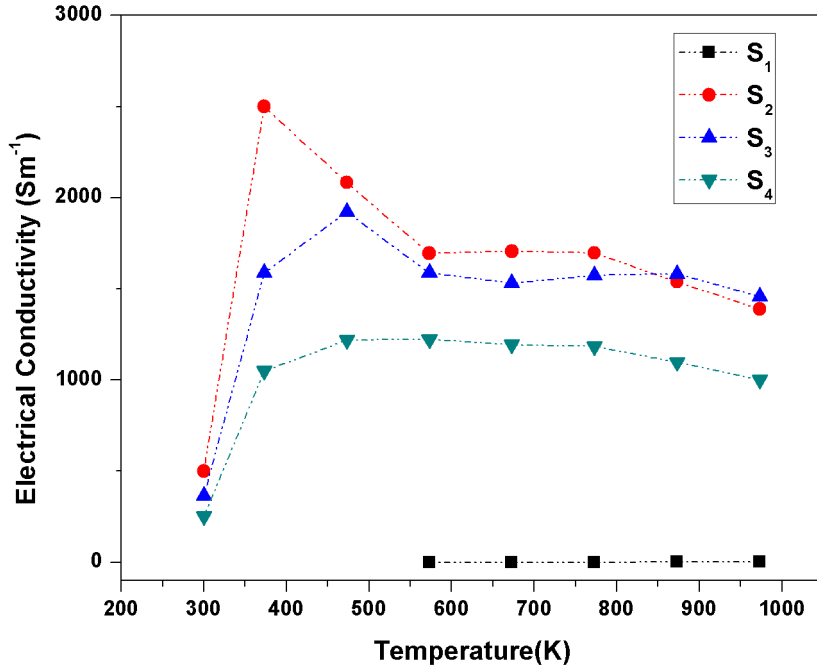


Figure 3.7: Variation of electrical conductivity with temperature for pure and Dy doped ZnO.

band and there causes an exchange potential between the carriers. Along with the doping induced charge carriers, thermally activated carriers also results in the change in chemical potential of the system and the Fermi level shifts towards the conduction band edge. Since the singly degenerate 4s and 2p shell are unoccupied, the mobility of the free charge carriers are much high and contributes towards the inflation of electrical conductivity. Above 373 K, the intrinsic minority carriers dominates and results in the obstruction in the electron free movement. The decrease in electrical conductivity for 0.2 and 0.3 atomic % of Dy doping was mainly due to the decrease in mobility caused by the increment in charge carrier concentration as per the Hall measurement data and the formation of Dy₂O₃ phase which is less electrically conducting.

Variation of Seebeck coefficient

The Seebeck coefficient(S) as a function of temperature for the different Dy concentration was shown in Fig: 3.8. The negative value of Seebeck coefficient over the whole temperature range ensured electrons as the majority charge carriers. The undoped ZnO has large negative Seebeck coefficient compared to the doped samples, due to the low carrier concentration. Seebeck coefficient is sensitive to the change in Fermi level and has been used to investigate the electron conduction process in semiconductor material. Fritsche derived a model depicting the correlation connecting Seebeck coefficient, energy difference between the conduction band and Fermi level [16]. For the n type semiconductor, Seebeck coefficient is defined as:

$$S = \frac{-k_B}{e} \left(\frac{E_c - E_F}{k_B T} + A_c \right) \quad (3.9)$$

The term A_c is given by:

$$A_c = \frac{\int_0^\infty \frac{\varepsilon}{kT} \sigma(\varepsilon) d\varepsilon}{\int_0^\infty \sigma(\varepsilon) d\varepsilon} \quad (3.10)$$

with $\varepsilon = E - E_c$ which is a temperature independent constant, accounting for the carriers that are distributed beyond the conduction band E_c . The slope of the graph plotted with $-S$ along the y axis and $1/T$ on the x axis gives the value of $E_c - E_f$ and the values are shown in Table: 3.3.

From the obtained results it was shown that the derived Fermi level as measured from the conduction band edge is positive for the pure ZnO and it shows a negative value for the doped samples. The negative value indicates that the Fermi level shifts above the conduction band edge for all the Dy doped ZnO samples and the material become degenerate.

For degenerate semiconductor the Seebeck coefficient is the measure of asymmetry in the electronic structure and it decreases with increase in carrier concentration. The Mott's relation substantiate this statement given by,

$$S = \frac{8\pi^2 k_B^2 m^* T}{3eh^2} \left(\frac{\pi}{3n} \right)^{2/3} \quad (3.11)$$

Table 3.3: Difference in Fermi energy with the conduction band edge

Sample	$E_c - E_f$ (eV)
S ₁	0.084± 0.002
S ₂	-0.023±0.005
S ₃	-0.009±0.001
S ₄	-0.03± 0.003

where k_B , h , m^* and n are Boltzmann constant, Planck constant, the effective mass of the carriers and the carrier concentration respectively. Increase in electron concentration of the doped sample results for the decrease in Seebeck coefficient. As the temperature increased above the energy cost of intrinsic excitation, the Seebeck coefficient decreases due to the cancellation of thermoelectric voltage by holes and electrons [17].

Power factor

Power factor which is a function of thermopower and electrical conductivity ($S^2\sigma$) substantiate the measure of energy stored in the material due to the asymmetry in the band structure near the Fermi level. The power factor for the pure and Dy doped ZnO samples were calculated for a temperature range 300-1000 K and it was shown in Fig: 3.9. Dy doped samples possess much higher power factor for the 0.1 and 0.2 doping % compared to pure and 0.3 atomic % of Dy doping.

Thermal conductivity measurement

An effective way of maximizing the figure of merit (ZT) is to modulate the lattice thermal conductivity in which the phonons are the energy carriers at higher temperature. C. Wood [18] first proposed the idea that a solid solution with a compound of similar electronic valence but different atomic mass resulted in the increased figure of merit. The reasoning was that a

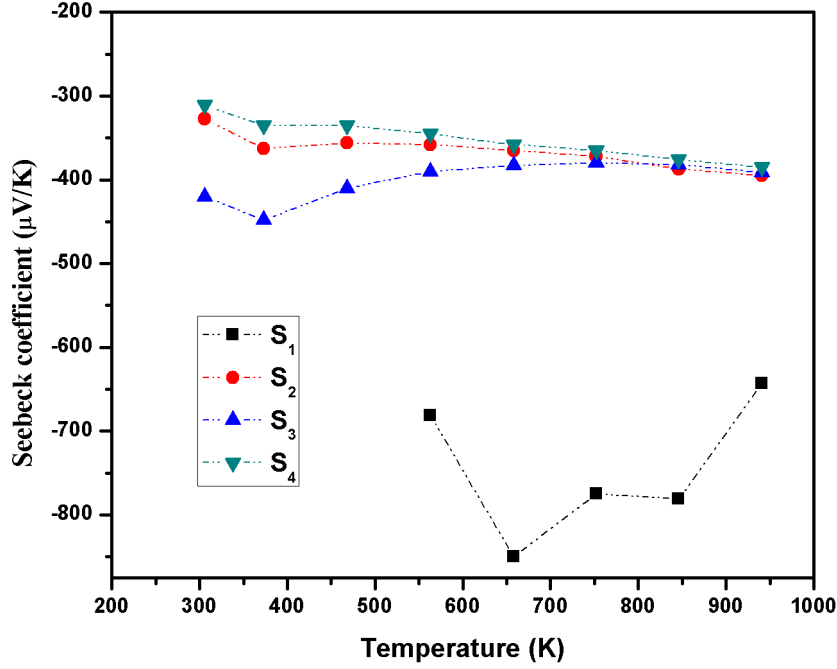


Figure 3.8: Variation of Seebeck coefficient with temperature for the pure and Dy doped ZnO.

foreign atom of similar valence will introduce local lattice distortion that does not appreciably scatter-free charge carriers (with their long wavelengths) but strongly scatters phonons. Thus, the thermal conductivity can be lowered without seriously affecting the electrical conductivity. The strategy that is adopted in this work for reducing the lattice thermal conductivity is mainly through the introduction of heavier Dy ion.

Massive Dy ions in the host mesh increases the scattering of phonons and its localized magnetic moment induce distortion in the lattice which results in reduction of phonon mean free path. Thermal conductivity for the pristine and Dy doped ZnO samples from a temperature range 300-1000 K were shown in Fig: 3.10. Thermal conductivity for all the samples exhibit an exponential decay at lower temperature and found to have an inverse temperature dependence when moving towards higher temperature. At lower temperature scattering contribution arose from induced and static charge

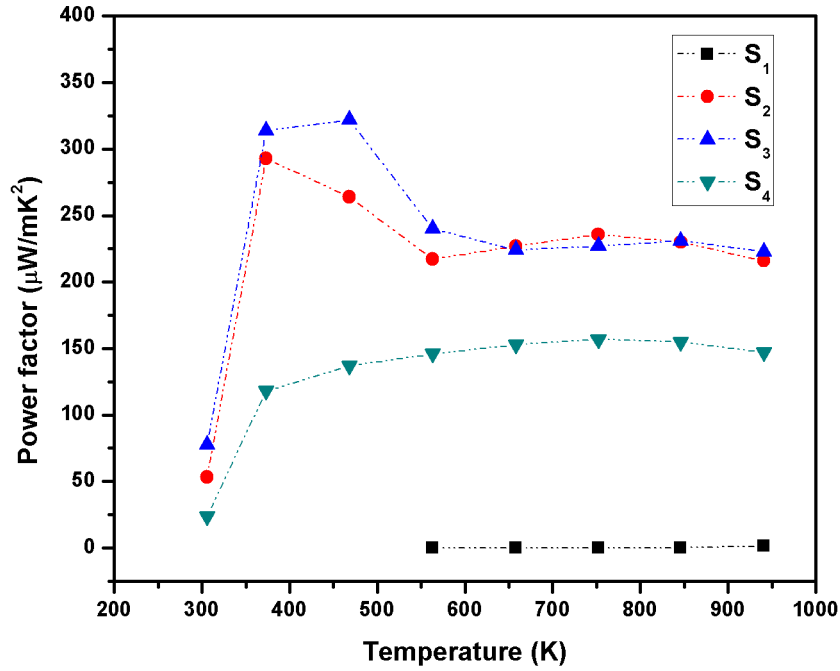


Figure 3.9: Variation in power factor with temperature for pure and Dy doped ZnO.

carriers but at high temperature mean free path of the phonons get deteriorated. Static imperfections in the lattice can be an important source of phonon scattering and it includes mass fluctuations, lattice disorder, dislocations and crystal grain boundaries [18]. Abeles proposed a model incorporating the size, inter atomic force difference and conclude that to maximize the phonon scattering, one should choose the atom that has the largest mass and size differences with the atom to be substituted [19]. The scattering of long wavelength phonons by electrons will be prominent whose wave numbers are comparable at high temperature. Dysprosium ions possess large localized magnetic moment among the lanthanide family due to their increased number of unpaired electrons and induce paramagnetic domains. As the temperature increases there occurs spin state transition and the lattice disorder increases. This lattice disorder will cause for reduced heat conductivity in the ZnO lattice which is diamagnetic [20]. Scattering of phonons at the

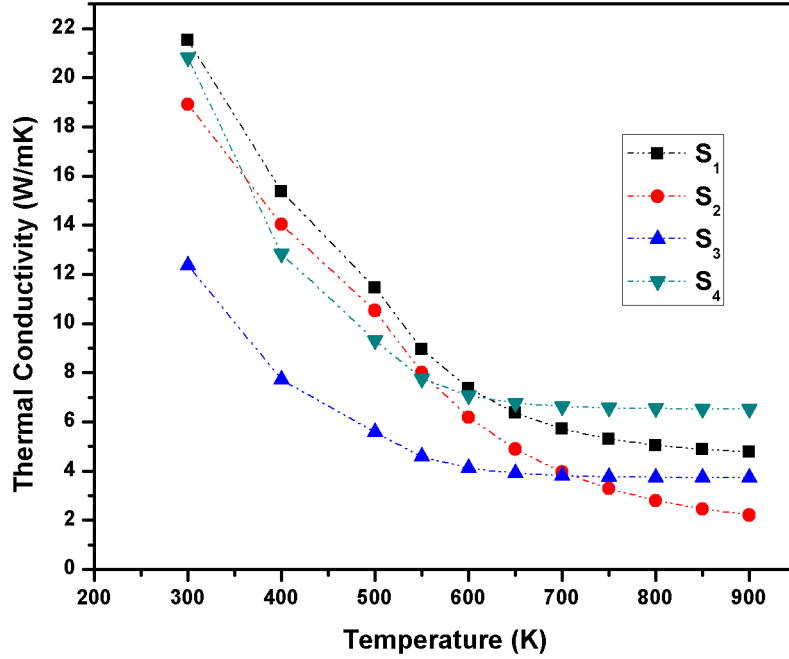


Figure 3.10: Variation of thermal conductivity with temperature for pure and Dy doped ZnO.

grain boundaries also contributes for reduction in thermal conductivity. As the phonons travel through the lattice the mean free path for the phonons get disturbed due to the formation of distorted lattice environment created by Dy ion and thus thermal conductivity reduced from 6W/mK to 2W/mK for the 0.1 atomic% of Dysprosium doping at 935 K. This reduced lattice thermal conductivity became responsible for the enhanced ZT value.

3.3.7 Figure of merit

Based on the measured electrical conductivity, thermal conductivity and Seebeck coefficient, the figure of merit ZT is readily obtained, and shown in Fig: 3.11. Dy-ZnO ceramic had present much improved thermoelectric performance over the pure ZnO. The 0.1 atomic % of Dy doping demonstrates a marked increment in the figure of merit about 0.11 at 935 K and arose as a potential candidate for thermoelectric applications.

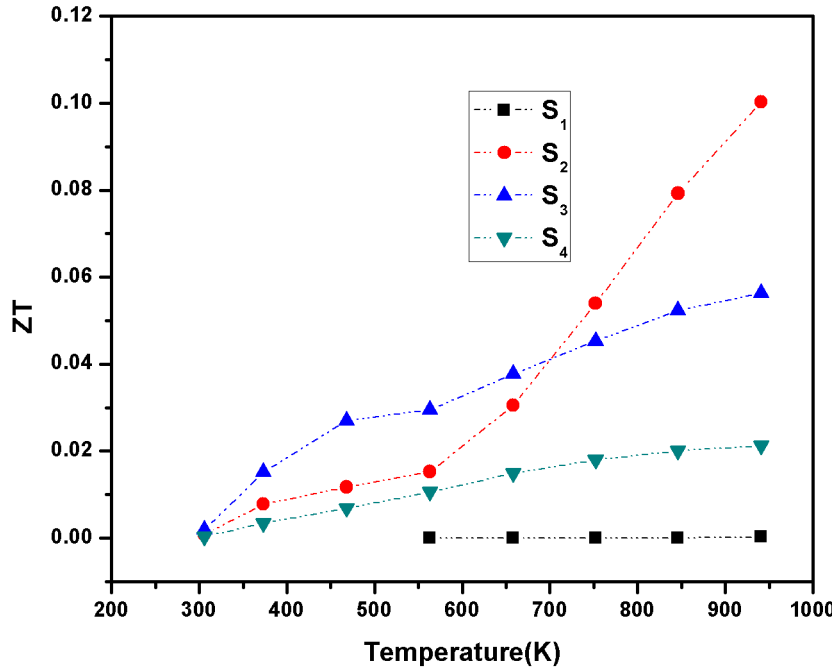


Figure 3.11: Variation of ZT value with temperature for pure and Dy doped ZnO.

3.4 Conclusions

Dy doped ZnO satisfy the decoupling of contradicting transport properties that are required for a highly efficient TE material at high temperature. In this chapter 0.1, 0.2, 0.3 atomic % of Dy doped ZnO samples were prepared by solid state reaction method. Structural detection and composition analysis were done using X-ray analysis. Residual strain induced in the hexagonal lattice was determined using the integral breadth of (101) plane. Raman spectroscopy revealed the distortion caused in the crystal lattice due to Dy incorporation. SEM micrographs represents that the heat waves can easily pass through the microstructure and the reduction in lattice thermal conductivity is mainly due to the impurity phonon scattering. EDAX confirmed the presence of Dy ion in the host ZnO matrix. All the Dy doped ZnO samples in the present work demonstrated an increase in electrical conductivity and a decrease in the Seebeck coefficient with temperature compared to the pure

ZnO. Room temperature UV absorption spectroscopy revealed the widening of optical band gap due to Dy incorporation and confirm the material to be degenerate. Increase in carrier concentration and thereby the upliftment of Fermi level towards the conduction band edge is the criteria applied behind the enhancement of power factor. Heavier Dy ion act as scattering center and the localized magnetic moment induce distortion in the plane resulted in the reduction in lattice thermal conductivity due to phonon electron and phonon-impurity scattering. In conclusion, the thermal transport property of Dy ion doped ZnO lattice was studied. 0.1 atomic % of Dy doping was found to possess a good performance having a ZT value of 0.11 at 935 K and can be chosen as promising material for energy harvesting.

References

- [1] J.R. Sootsman, D.Y. Chung, M.G. Kanatzidis, *Angew. Chem. Int.* 48 (2009) 8616-8639.
- [2] T.M. Tritt, M.A., *MRS Bull.* 31 (2006) 188-194.
- [3] M. Kahouli, A. Barhoumi, A. Bouzid, A. Al-Hajry, S. Guermazi, *method, Superlattice.Microstruct.* 85 (2015) 7-23.
- [4] P.P. Pradyumnan, A. Paulson, N.A. Muhammed Sabeer, N. Deepthy, *AIP Conf. Proc.* 1832 (2017) 1-4.
- [5] G. Tan, L.D. Zhao, M.G. Kanatzidis, *Chem. Rev.* 116 (2016) 12123-12149.
- [6] E.M. Levin, S.L. Bud'Ko, K. Schmidt-Rohr, *Adv. Funct. Mater.* 22 (2012) 2766-2774.
- [7] N.K. Divya, P.P. Pradyumnan, *J. Mater. Sci. Mater. Electron.* 28 (2017) 2147-2156.
- [8] S. Bhatia, N. Verma, R.K. Bedi, *Opt. Mater. (Amst).* 62 (2016) 392-398.
- [9] A.K. Zak, W.H.A. Majid, M.E. Abrishami, *Solid State Sci.* 13 (2013) 251-256.
- [10] A. You, M.A.Y. Be, I. In, *Micro-Raman investigation of optical phonons in ZnO nanocrystals*, (2005) 124313.

- [11] R. Cusco, E. Alarcon-Llado, J. Ibanez, L. Artus, J. Jimenez, B. Wang, and M. J. Callahan, *Phys. Rev. B.* 75 (2007) 165-202.
- [12] P. J. Colwell and M. V. Klein, *Phys. Rev. B.* 6 (1972) 498-515.
- [13] N.R. Yogamalar, A. Chandra Bose, *Appl. Phys. Mater.Sci. Process.* 103 (2011) 33-42.
- [14] R.S. Ajimsha, A.K. Das, B.N. Singh, P. Misra, L.M. Kukreja, *Phys. E Low-Dimens. Syst. Nanostruct.* 42 (2010) 1838-1843.
- [15] K. Park, H.K. Hwang, J.W. Seo, W.S. Seo, *Energy*, 54 (2013) 139-145.
- [16] H. Fritzsche, *Solid State Commun.* 9 (1971) 1813-1815.
- [17] Y. Liu, W. Xu, D. Liu, M. Yu, Y. Lin, C. Nan, *Phys. Chem. Chem. Phys.* 17 (2015) 11229-11233.
- [18] C. Wood, *Rep. Prog. Phys.* 51 (1988) 459-539.
- [19] B. Abeles, *Phys. Rev.* 131 (1963) 1906-1911.
- [20] P. Gorai, E.S. Toberer, V. Stevanović, *Phys. Chem. Chem. Phys.* 18 (2016) 31777–31786.

Chapter 4

Nanomaterials for Thermoelectricity

Objectives

This chapter presents a brief outline about the thermoelectric properties of bulk nanostructured material. Introduction of donor ion increases the carrier concentration and the presence of inhomogeneous micro, meso pores in the lattice reduce the lattice thermal conductivity. The combined effect of these mechanisms lead for the improved thermoelectric efficiency.

4.1 Introduction

In this chapter we are dealing with bulk nano thermoelectric materials and the factors responsible for the improvement in thermoelectric(TE) properties. Bulk nanostructured materials are defined as bulk solids with nanoscale or partly nanoscale microstructures. Low-dimensional thermoelectric materials are believed to have higher TE properties than their bulk counterparts, because the DOS near Fermi energy level can be enhanced through quantum confinement. Lattice thermal conductivity (LTC) can be reduced by the effective scattering of phonons at high density of interfaces, impurities and at the pore boundaries. Along with the enhancement in thermopower, LTC should be reduced for the optimization of dimensionless figure of merit.

Thermopower for the low dimensional materials can be defined using the Mott's relation:

$$S = \frac{-\pi^2 k_B^2 T}{3e} \left[\frac{1}{\mu} \frac{d\mu(E)}{dE} + \frac{1}{n} \frac{dg(E)f(E)}{dE} \right]_{E=E_f} \quad (4.1)$$

where $g(E)$ is the electronic density of states(DOS), $\mu(E)$ is the charge carrier mobility and $n(E)$ gives the charge carrier concentration. Seebeck coefficient is the measure of asymmetry in the electronic structure and scattering rates near the Fermi energy level. Quantum confinement in nanostructures increases the local carrier density of states near the Fermi energy and the Seebeck coefficient gets increased. A material with rapidly changing DOS near the Fermi level is expected to have larger Seebeck coefficient than with flatter DOS near E_f . The dependence of carrier mobility on energy of charge carriers increases with scattering mechanism. Scattering mechanism will be pronounced in nano grain samples due to the presence of nano grain boundaries, impurities and pores. As the scattering mechanism increases the mobility offered for the charge carriers get decreased and responsible for the increment in the thermopower.

For bulk nano structures the enhancement in figure of merit arise due to the reduction in lattice thermal conductivity rather than increase in density of

states. The reduction in lattice thermal conductivity mainly caused by the increased pore concentration and grain boundaries. Thermal conductivity had the combined contribution from electron (κ_{el}) and lattice phonons (κ_{ph}). According to Callaway model, the LTC κ_{ph} related to phonon relaxation time (τ) can be defined as [1]:

$$\kappa_{ph} = \frac{1}{3} \int_0^{\omega_{max}} c_s(\omega) v_g^2(\omega) \tau(\omega) d\omega \quad (4.2)$$

where c_s is the heat capacity, v_g is the phonon group velocity and τ defines the phonon relaxation time. Based on the Matthiessen rule the combination of different phonon scattering lead to lower τ value, which in turn reduces the κ_{ph} [2]. Self formed inhomogeneities in nanoscale caused by the phase segregation phenomenon during nucleation and growth in bulk nanostructured materials reduce the lattice thermal conductivity [3]. When the grain size become comparable to the critical mean free path of electrons and phonons, size dependent properties of nanomaterials has to be evident. Moreover grain size in nanoscale results for the drastic increase in density of grain boundaries reaching typical densities of 10^{19} interfaces per cubic centimeter [4]. Theoretical prediction shown that reduction in lattice thermal conductivity can be achieved by the scattering of phonons at the grain boundaries. A considerable reduction in LTC can also be achieved by the introduction of porosity in the material by nanostructuring. It was Goldsmid and Penn pointed out that the high frequency phonons get scattered by point imperfections where as the low frequency heat carryings phonons get scattered at the grain boundaries, at the interfaces and at the pores [5].

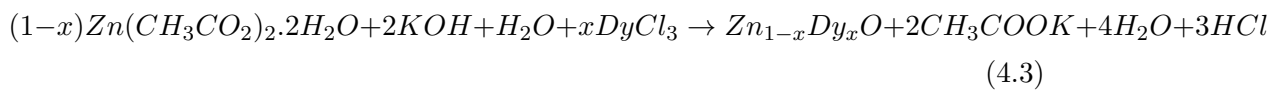
Xin Liang reported the enhancement in thermoelectric figure of merit with Fe content in nano ZnO lattice, due to the reduced thermal conductivity by point defect scattering of phonons and enhanced electrical transport via doping [6]. Luca Bertini proposed the reduction in lattice thermal conductivity and thereby enhancement of ZT value in nanostructured skutterudites (CoSb_3) due to the presence of grain boundaries [7]. Besides the grain boundary contribution R.H Tarkhanyan and D.G Niarchos proposed a physical model for the reduction in LTC based on the diffuse scattering of phonons at

the pore-medium interface and concluded that inhomogeneous pores in the medium emerged as an effective scattering center for the lattice phonons [8]. Jae-Yeol Hwang et al reported extremely low lattice thermal conductivity of 0.5 W/mK at 773 K in pore-embedded PbTe due to the enhanced phonon scattering by mismatched phonon modes in the presence of inhomogeneous pores [9].

This chapter deals with the synthesis and physical property studies of bulk nano materials with different Dy doping in ZnO. The major objective of this chapter is to understand the factors and ways by which thermoelectric efficiency get enhanced through nanostructuring. Structural, morphological and thermoelectric properties of synthesised nanopowder was studied. The surface porosity and the characteristics of the pores were analysed using the BJH analysis.

4.2 Synthesis of nanomaterials

Nano zinc oxide powder was prepared using hydrothermal synthesis. The reaction was carried out using the analytical reagent grade zinc acetate ($Zn(CH_3CO_2)_2 \cdot 2H_2O$) and KOH. For the synthesis mechanism, zinc acetate was taken in a beaker and made to dissolve in 160 mL of double distilled water. 1 molar KOH solution was added drop by drop until the pH of the resultant solution was 12. This mixture was stirred for one hour to obtain a homogeneous solution. The resulting solution was kept in teflon lined sealed autoclave and heated at $150^{\circ}C$ for 8 hours. The precipitate obtained from the reaction process were filtered out and centrifuged at a rpm of 1300 with double distilled water. The resultant slurry was allowed to dry in hot air oven at $130^{\circ}C$ for one hour. Different weight percentage of dysprosium chloride ($DyCl_3$) was added to the mixture for the formation of Dy doped ZnO and the reaction mechanism is followed in Equation:4.3.



The powder obtained from this synthesis mechanism were compacted in to disc shaped pellets of diameter 10 mm with 3 mm thickness. These pellets were sintered at 750⁰C for 6 hours and used for structural and TE characterization.

4.3 Results and discussion

4.3.1 XRD analysis

Fig: 4.1 shows the room temperature powder X-ray diffraction patterns of the nanopowder corresponding to pure ZnO, 0.5, 0.75 and 1 wt % DyCl₃ added ZnO named as H₁, H₂, H₃, H₄ respectively. The spectra was recorded for the 2 θ varying from 20-80⁰ with a scanning speed of 10⁰/min. XRD peaks pointed out the hexagonal wurtzite structure of ZnO with P6₃mc space group and the peaks were indexed according to the standard ICDD card no: 00-005-0664 [10]. The absence of extra peaks confirmed the purity and single phase of the compound formed. The highly intense peaks from the different lattice plane revealed the crystalline nature of the compound. The addition of DyCl₃ at different weight % resulted in the substitutional incorporation of trivalent Dy³⁺ ions in ZnO lattice. For the 1 wt % of DyCl₃ addition an extra peak at 28.91⁰ had been formed corresponding to Dy₂O₃ and this can be considered as the solubility limit of Dy under this preparation condition. Studies show that the lower solubility limit of dysprosium may be due to the higher ionic radii of Dy³⁺ ion compared to Zn²⁺.

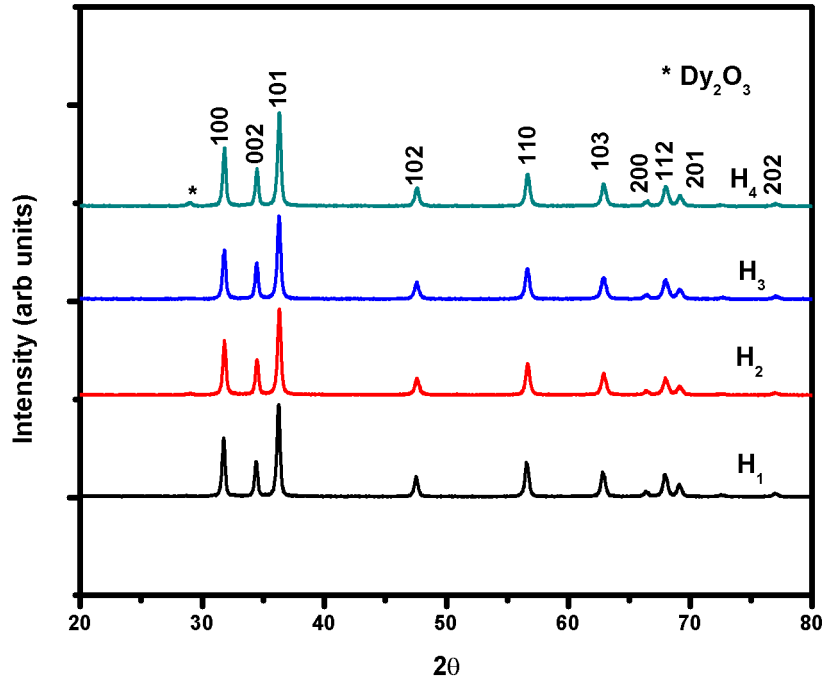


Figure 4.1: The XRD patterns corresponding to Dy doped ZnO samples.

As mentioned in chapter 3 crystallite size was calculated from the Scherrer formula and the determined lattice parameters were depicted in Table: 4.1. As the doping concentration increases the average crystallite size decreases due to the strain induced in the lattice up to the solubility limit of 1 wt % DyCl_3 addition.

4.3.2 Raman analysis

The Raman spectra analysis was performed in order to determine the vibrational modes corresponding to the constituent elements present and to confirm the presence of Dy ion. Fig: 4.2 represents the Raman spectrum of the prepared samples and data in Table: 4.2 depicts the peak position.

The Raman vibrational modes in the range $350\text{-}400\text{ cm}^{-1}$ corresponds to $A_1(\text{TO})$ and $E_1(\text{TO})$ modes. The shift of $A_1(\text{TO})$ peak (387 cm^{-1}) to lower wave number (382 cm^{-1}) with Dy doping attributed to the variation in the

Table 4.1: Variation of crystallite size and lattice parameters for different Dy concentration

Sample	Crystallite size(nm)	Lattice constant(a)(\AA)	Lattice constant(c)(\AA)
H ₁	29.9	3.257	5.209
H ₂	27.3	3.251	5.200
H ₃	26.3	3.252	5.202
H ₄	27.0	3.250	5.199

Table 4.2: Raman vibrational frequency for different symmetry elements

Sample	E ₂ (low) (cm ⁻¹)	A ₁ (TO) (cm ⁻¹)	E ₂ (high)(cm ⁻¹)	A ₁ (low) (cm ⁻¹)
Theory([13])	99	387	430	584
H ₁	98	387	437	581
H ₂	98	382	437	580
H ₃	98	384	437	581
H ₄	98	383	437	582

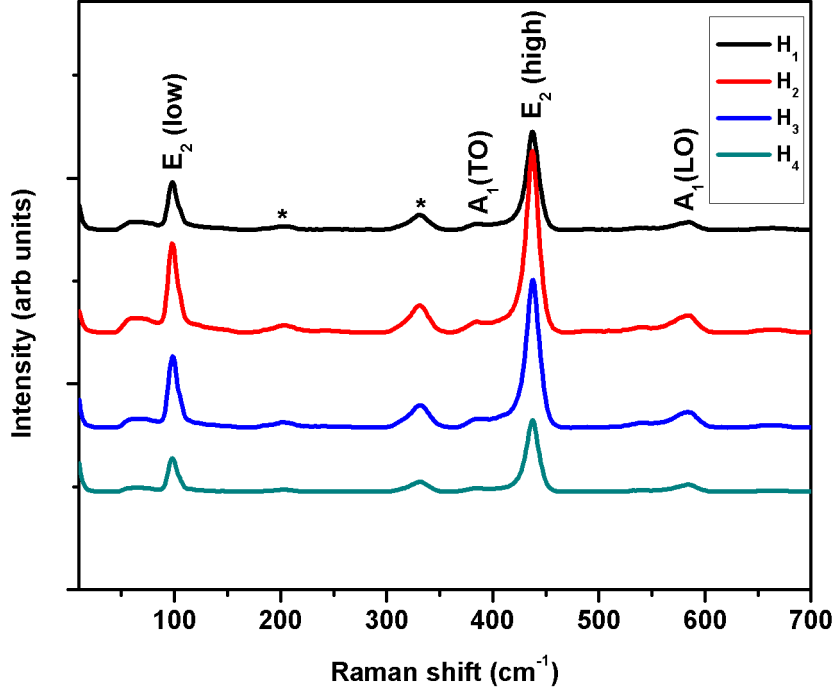


Figure 4.2: Room temperature micro Raman spectra for Dy doped ZnO samples.

ionic radii and structural deformation for the Zn-O bond. As the reduced mass increases with dysprosium doping, the frequency of Zn-O vibration get blue shifted as per the relation: $\nu = \frac{1}{2\pi c} \sqrt{\frac{K}{\mu}}$ where ν represents the wave number corresponds to $A_1(\text{TO})$ mode, c is the velocity of light and μ denotes the reduced mass. The broad peak at 330 and 202 cm^{-1} corresponds to the second order Raman process [12]. The disorder Raman band as explained in chapter 3 corresponding to $E_1(\text{LO})$ mode is absent for the bulk nano structured material. However, the intensity of Raman band for the $A_1(\text{LO})$ mode increases with increase in Dy concentration.

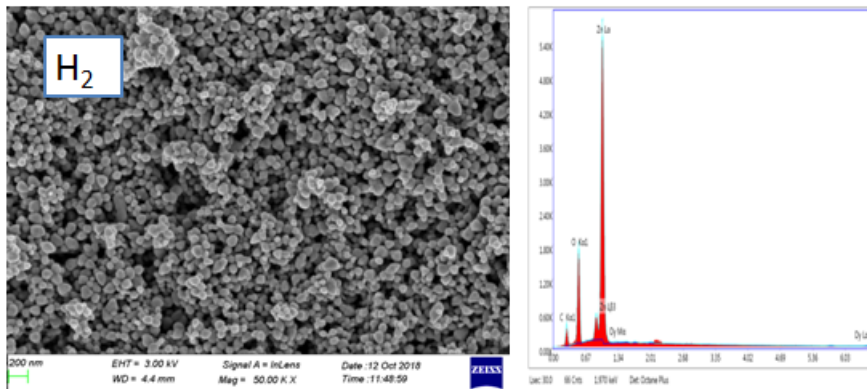
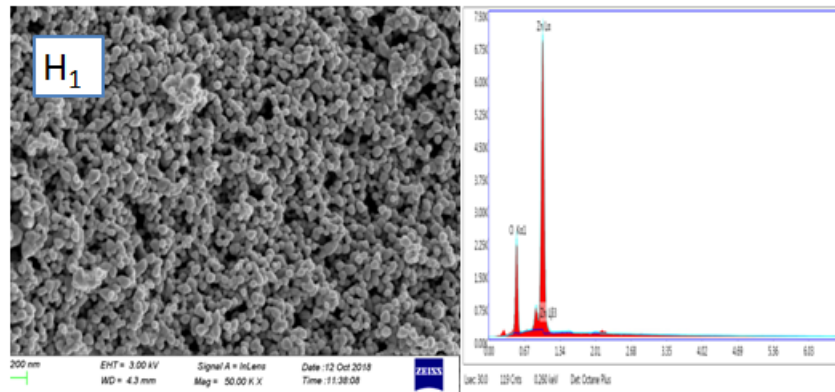
4.3.3 Morphological analysis

SEM and EDAX techniques were performed to analyze the surface morphology and chemical composition of the material synthesized. Fig: 4.3 shows the SEM micrographs of the prepared nano powder and the corresponding energy dispersive spectra. Uniform spherical nanospheres were formed with in a range of radius 60-80 nm. As the Dy doping increases the spherical nature of the crystallites get lost and the shape get distorted. The distortion is due to the strain induced by larger ionic radii Dy ion. EDS analysis confirms the presence of Dysprosium ion in the doped sample and the absence of other impurities. Uniform nano spheres will easily obstruct the mean free path for the long wave length phonons thereby reduce the lattice thermal conductivity. The mean free path for the electrons will not be much disturbed by grain boundaries where as for the phonons its direction of motion will be disrupted and thus scattered at the nanoscale. This scattering mechanism resulted in the decrease in lattice thermal conductivity.

4.3.4 Optical studies

UV-Visible spectroscopy

UV-Visible spectroscopy deal with the fundamental absorption of light energy that lead to the fact that minimum quantum of energy sufficient to excite electron from the valence band to the conduction band. The required amount of quantum energy for excitation termed to be the direct band gap energy and it can be determined from Tauc plot as shown in Fig: 4.4. The absorption coefficient α was determined using the Kubelka Munk function $\alpha = \frac{(1 - R)^2}{2R}$ where R is the diffused reflectance. As the particle moves towards the nano regime the energy levels becomes distinct and the band gap energy increases. The optical band gap energy for the microstructured ZnO is in the region of (3.1-3.2 eV) whereas for the nanograined boundaries it lies in the region of (3.2-3.3 eV). The optical band gap for the pure and Dy



doped ZnO nanostructures were given in table: 4.3. Although the carrier concentration increases for the doped sample the band gap energy decreases and the Burstein Moss shift is not observed for the samples. As evident from the Hall measurement data the formation of donor level near the conduction band edge results in the decrement in band gap energy.

Table 4.3: Bandgap energy for different Dy concentration in ZnO

Sample	Band gap energy(eV)
H ₁	3.221
H ₂	3.213
H ₃	3.217
H ₄	3.214

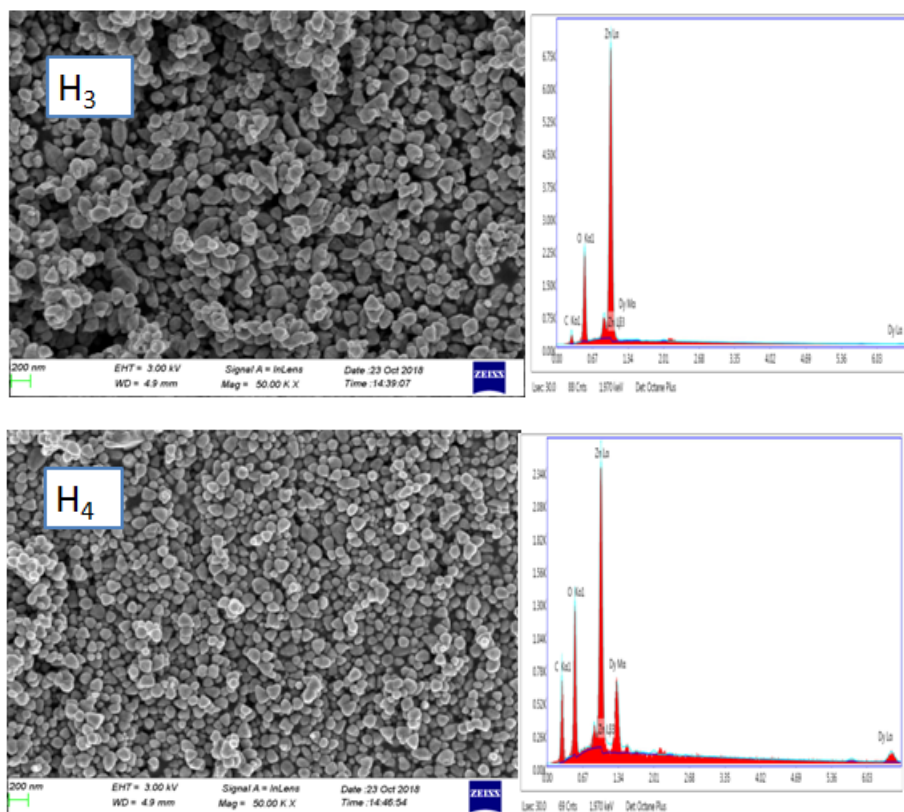


Figure 4.3: SEM and EDAX corresponding to different Dy concentration in ZnO.

4.3.5 Electrical properties

The carrier concentration, mobility and electrical conductivity was determined using the Hall measurement data at room temperature by the applying a magnetic field of 0.55 Tesla perpendicular to an electric field of 0.5 mA. The electrical characteristics of the bulk nano structured materials were measured using Van der paw method. In this method four contacts were taken from the corners of smooth polished surfaces of the square pellets and conducting silver paste was used as the adhesive for making electrical contact with the measuring tips. Table: 4.4 depicts the measured electrical characteristics determined from the Hall voltage by four terminal method. As from the Hall measurement data it is evident that for the H₂ sample there occurs an increased carrier concentration which results in the increment in electrical

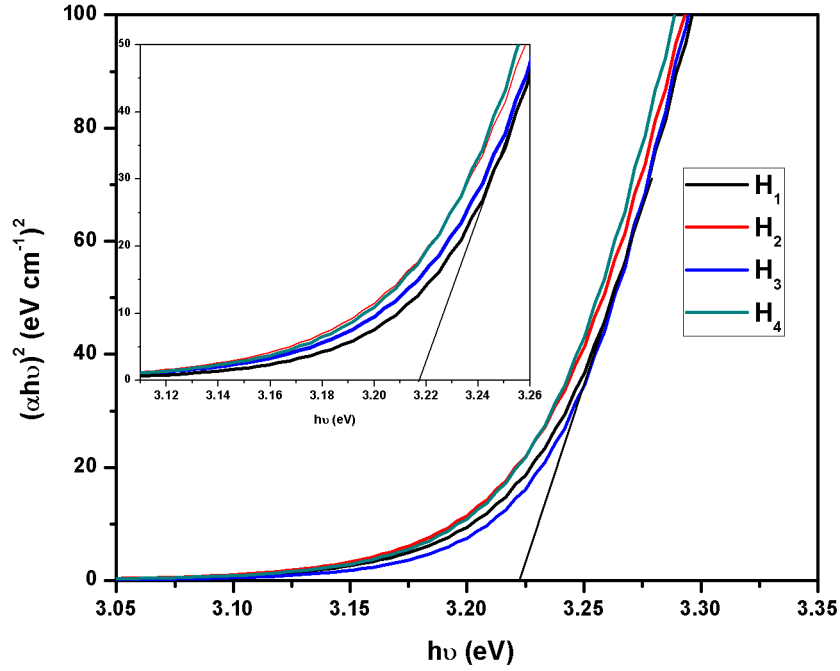


Figure 4.4: Kubelka Munk function Vs $h\nu$ for different Dy concentration in ZnO.

conductivity. For the higher doping percentage of Dy ion the carrier concentration decreases and the increased mobility become responsible for the enhancement of electrical conductivity. The negative Hall coefficient, shows the samples are of n-type semiconductors. For the H₃ and H₄ sample the Dy³⁺ ions could not completely contribute its free electron to the ZnO lattice thereby reduce the amount of free charge carriers. Decrement in carrier concentration imparts mobility due to the reduced scattering.

Table 4.4: Electrical characteristics of Dy doped ZnO samples

Sample	Concentration (cm ⁻³)	Mobility (cm ² /Vs)	Conductivity (Ω ⁻¹ cm ⁻¹)
H ₁	-1.32*10 ¹⁰	2.15*10 ²	4.55*10 ⁻⁷
H ₂	-6.98*10 ¹²	1.76*10 ¹	1.96*10 ⁻⁵
H ₃	-1.11*10 ¹¹	1.02*10 ²	1.79*10 ⁻⁶
H ₄	-1.36*10 ¹⁰	5.86*10 ²	6.30*10 ⁻⁶

4.3.6 Porosity analysis

Gas adsorption is an important technique for the characterization of porous solids and fine powders. Adsorption is defined as the enrichment of molecules, atoms or ions in the vicinity of an interface. Adsorption can be physical or chemical. In physisorption the adsorbable gas (the adsorptive) is brought in to contact with the surface of a solid (adsorbent). Short range repulsive force, attractive dispersion force and specific molecular interaction (polarisation, field dipole) etc... are the features of physisorption. The term desorption denotes the converse process, in which the amount of gas adsorbed will be progressively decreases. Adsorption hysteresis arises when the adsorption and desorption curves do not coincide. Physical adsorption of gas molecules used to determine the presence of porosity and surface area of the adsorbent. Porosity is defined as the ratio of total pore volume to the volume of the particle or agglomerate. In the context of physisorption, pores can be classified according to the size (IUPAC recommendation, 1985) [14]

1. Pores with width exceeding about 50 nm is termed to be macropores.
2. Pores with width between 2 nm and 50 nm is termed to be mesopores.
3. Pore width not exceeding about 2 nm are called micropores.

The term nanopore embrace the above 3 categories of pores, with an upper limit ≈ 100 nm. The decrease in lattice thermal conductivity for the nanostructured sample can be attributed to the presence of higher porosity in the material. The analysis was done using the Barrer-Joyner-Halenda (BJH) techniques. The technique helps to substantiate the reduction in LTC arose due to the increased surface area and porosity for the nanostructured material.

Experimental procedure

Determination of physisorption isotherm is mainly based on two methods

1. Manometric method

2. Gravimetric method

Manometric method deals with the measurement of amount of gas removed from the gas phase based on the direct measurement of the uptake of gas whereas, the gravimetric measurement deals with the change in the mass of the adsorbent [15]. In this chapter the porosity and types of pores were determined using the static manometric method in which the measurement of changes in pressure of calibrated gas volumes was employed. A known amount of nitrogen gas is admitted to a confined calibrated volume containing the adsorbent, which is maintained at constant temperature (77K). As the adsorption take place, the pressure in the confined volume falls until equilibrium is established. The amount of gas adsorbed at the equilibrium pressure is given as the difference between the amount of gas required to fill the space around adsorbent [16]. The adsorption isotherm is usually constructed point-by-point admission of successive charges of gas to the adsorbent with the aid of dosing technique. In this work we mainly focus the decrease in lattice thermal conductivity for the nanostructured samples due to the presence of inhomogeneous pores in the material. The presence of higher porosity results in the increased scattering of phonons at the pore interface. Reduction in the LTC by diffused scattering of acoustic phonons at the pore-medium interface is much pronounced for the compound with inhomogeneous porosity than that in the case of homogeneous pores. The estimated surface area, pore diameter and pore volume of all samples are summarized in table: 4.5

BJH pore size distribution plot for the prepared samples were shown in Fig: 4.5. From the BJH pore size distribution plot it was found that all the prepared samples contain inhomogeneous pores. Most of the pores are in the range of pore radius 2-20 nm. As the number of inhomogeneous pores increases enhanced phonon scattering took place by mismatched phonon modes and leads to the reduction in LTC. As a consequence of phonon ballistic effect the LTC is lower for the materials having higher porosity with smaller pore radius [17]. The generation of mono dispersed nanoscale pores with

Table 4.5: Surface parameter for Dy doped ZnO samples

Sample	Pore diameter (nm)	Surface area (m^2/g)	Pore Volume (cm^3/g)
H ₁	15.59	1.80	0.41
H ₂	9.76	7.79	1.78
H ₃	8.91	9.60	2.21
H ₄	3.03	3.38	0.77

width less than 50 nm highly required to realize both strong scattering of heat carrying phonon and maintaining electronic transport properties [18]. It can be conclude that the presence of micro pores and the increased density of mesopores in doped and pristine nano sample responsible for the reduction in LTC. Energy filtering would take place at pores of smaller pore radius. Thus Dy doped samples are found to have smaller pore radius compared to pristine ZnO. The reduction of lattice thermal conductivity is the main criteria behind the enhancement of ZT value. The drastic reduction in LTC is found for the Dy doped samples due to the smaller average pore radius and increased pore volume compared to pristine nano ZnO.

4.3.7 Thermoelectric properties

Thermopower

Thermoelectric transport property the Seebeck coefficient was determined for the nanograined sample from room temperature to 900 K using ULVAC ZEM3 M8 under helium atmosphere. Fig: 4.6 represents the induced voltage developed as a result of temperature gradient at each base temperature for the pure and Dy doped ZnO samples. The negative thermopower points out electrons as the majority charge carriers. From Mott's relation it was evident that thermopower depends on the density of states at the Fermi energy level and inversely proportional to the mobility of free charge carriers. From the experimental result it was clear that nano grained samples have higher

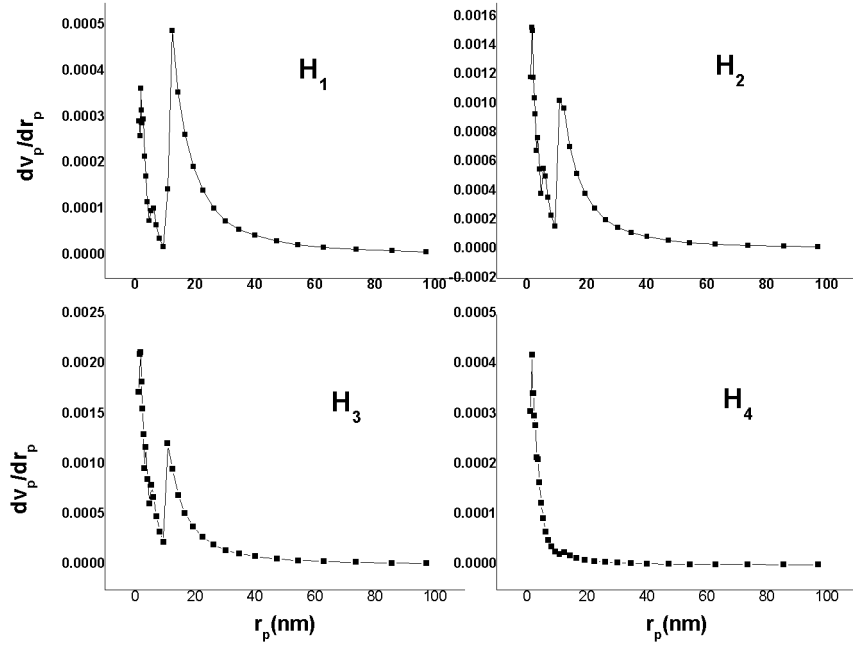


Figure 4.5: BJH pore size distribution.

density of states due to the defects at the grain boundaries and responsible for the increment in thermopower. From SEM micrographs, the presence of nano grain boundaries were evident and the acoustic phonons get scattered for the nano structured samples with higher carrier concentration. This increased rate of scattering causes the decrement in mobility and thus lead to higher thermopower. For the H₂ sample the increased carrier concentration along with reduced mobility resulted in the net thermopower to increase.

Fig: 4.7 depicts the variation of electrical conductivity with temperature and found to be low for the samples with lower carrier concentration. The electrical conductivity was found to be high for the H₂ sample up to 650 K. After that the electrical conductivity decreases and the H₃ and H₄ samples get dominated. After 650 K the scattering at the grain boundaries, impurity ions and at the pores became dominant and the mobility decreases which results in the reduction in electrical conductivity for the H₂ sample. The energy stored in a material due to the asymmetry in the band structure and

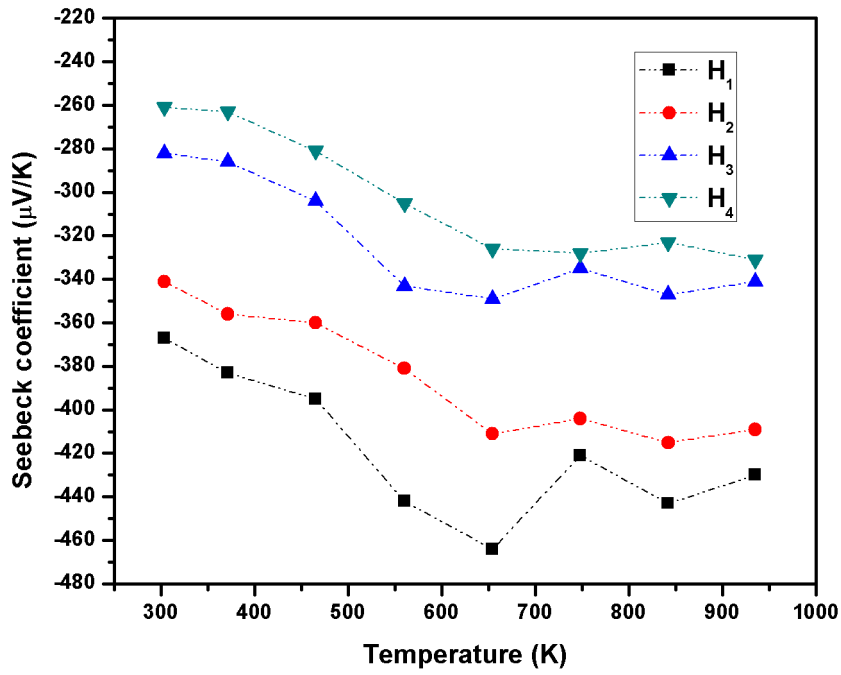


Figure 4.6: Variation of Seebeck coefficient with temperature for Dy doped ZnO samples.

carrier concentration was obtained by determining the power factor of the material and it was found to be high for the Dy doped sample as shown in Fig: 4.8.

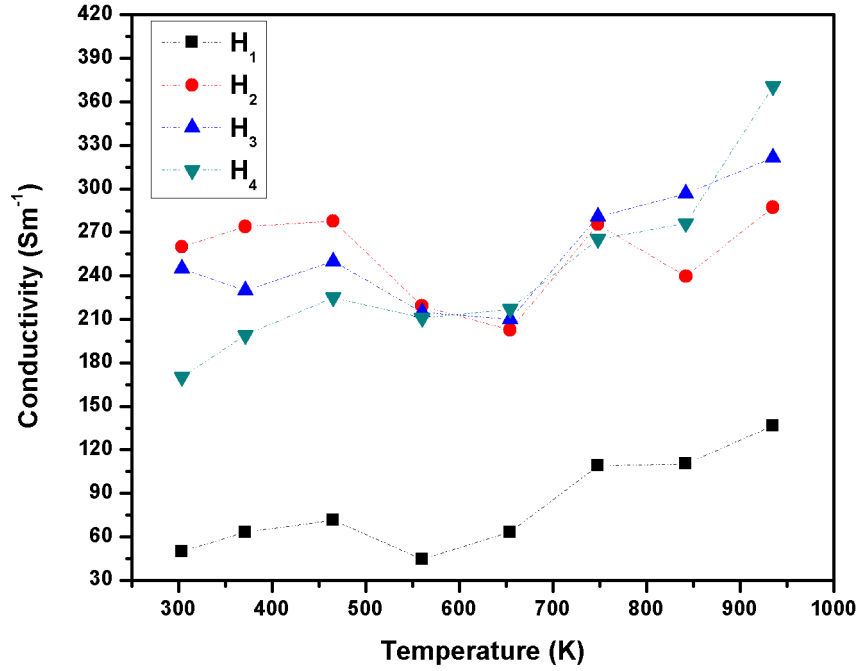


Figure 4.7: Variation of electrical conductivity for the Dy doped ZnO samples.

Thermal conductivity

Fig: 4.9 represents the decrease in thermal conductivity with increase in temperature and it had contribution from lattice phonons and electrons. Breaking the trade of between σ and κ by reducing the lattice thermal conductivity (κ_{ph}) is one of the most effective approaches for the enhancement of figure of merit. The contribution of electronic thermal conductivity due to charge carriers towards the total thermal conductivity is negligible and the main contribution arose from the lattice part. The LTC mainly depends on the phonon mean free path. Since the mean free path (mfp) of phonons is limited by scattering, long wave length phonons were suppressed. Phonon scattering mechanism usually originates from lattice defects and scattering by other phonons. One of the promising approaches is the formation of nanoscale pore structure and nano grain boundaries since such defects can be effective phonon scattering centers without sacrificing electronic transport properties (S and σ). More over this methodology cannot alter crystal struc-

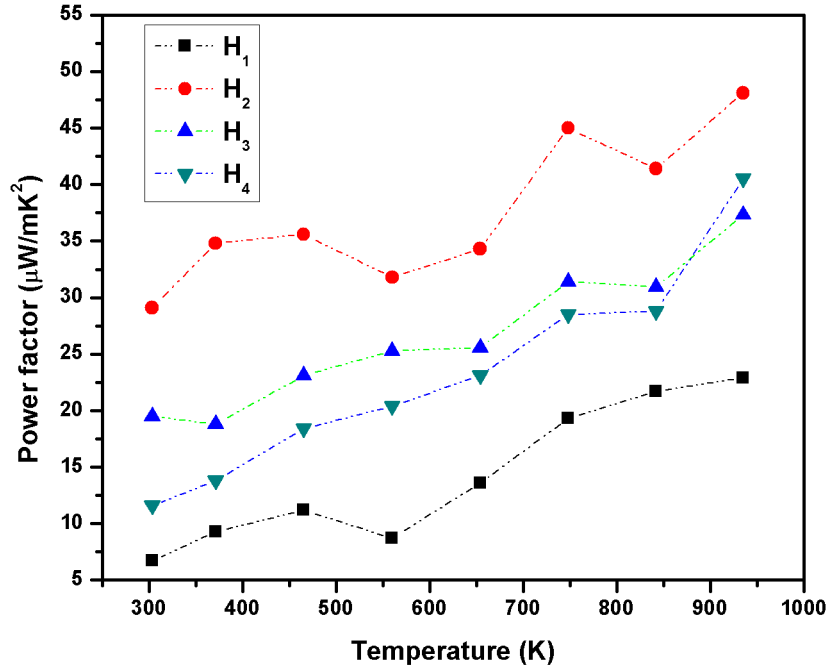


Figure 4.8: Variation of power factor with temperature for Dy doped ZnO samples.

ture and chemical composition of the host thermoelectric material. From the figure it is clear that along with the presence of inhomogeneous pores, impurity sites also act as suitable center for phonon scattering and thereby to reduce the lattice thermal conductivity. As shown in Fig: 4.9 thermal conductivity for the H₂ sample is found to be 0.95 W/mK at 935 K which is 6 times lower than the pristine ZnO. This decrease in lattice thermal conductivity arose due to the increase in pore volume and the presence of smaller pore radius. Phonons get easily scattered at the enhanced surface area. The decrease in thermal conductivity for the H₄ sample can be attributed due to the phonon scattering at the extra impurity phase along with scattering at the meso – macro pores.

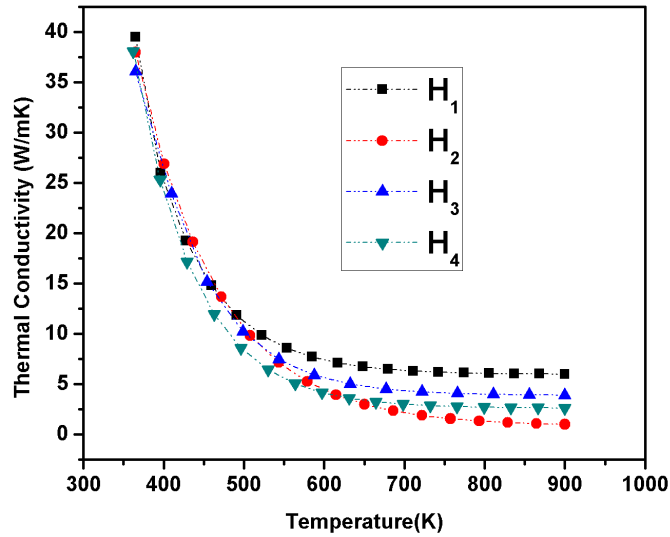


Figure 4.9: Variation of thermal conductivity with temperature for Dy doped ZnO samples.

4.3.8 Figure of merit

Variation of ZT value with temperature for different Dy concentration were shown in Fig: 4.10. 0.5 wt % DyCl₃ added bulk nanostructured ZnO possess the greatest figure of merit of 0.046 at 935 K due to the increment in the charge carrier concentration and reduced lattice thermal conductivity due to the presence of increased density of micro-meso pores.

4.4 Conclusions

Nanostructuring along with doping considered to be an efficient way for the enhancement of figure of merit. Hydrothermal synthesis was performed to obtain nano powder at elevated temperature and pressure. 0.5, 0.75, 1 wt% DyCl₃ doped ZnO was prepared by hydrothermal route respectively. Structural studies were performed using X-ray and Raman analysis. XRD results confirmed the strain induced in the lattice and the Raman analysis ensured the presence of Dy incorporation. Spherical morphology of the pre-

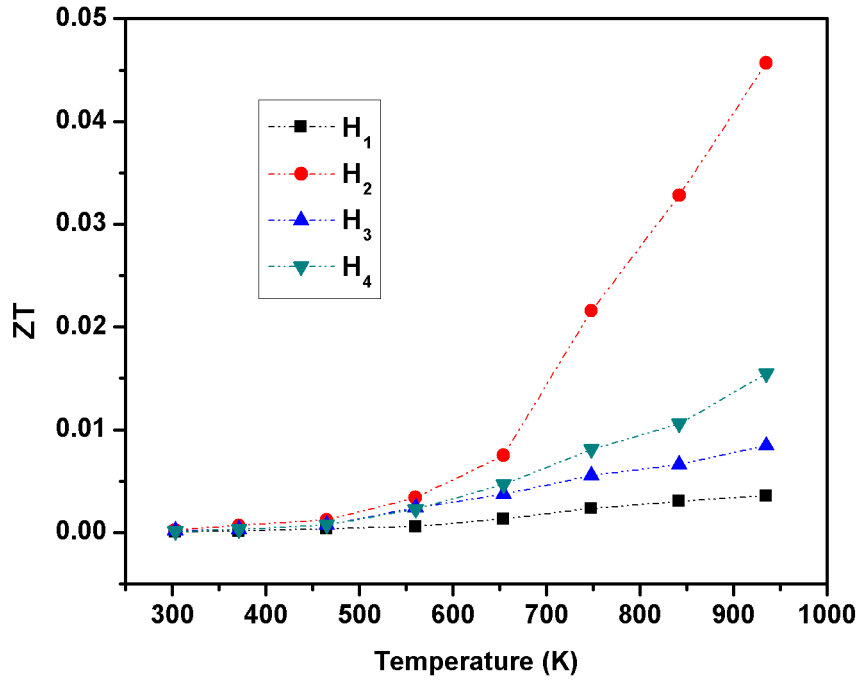


Figure 4.10: Variation of ZT with temperature for Dy doped ZnO samples.

pared samples were obtained using scanning electron microscopy. Nanostructuring increases the density of states and thereby lead to the thermopower enhancement. Main mechanism for improvement in the ZT value for the nanomaterials lies on the fact of porosity which causes reduction in lattice thermal conductivity. Pore boundaries act as effective phonon scattering centers at the presence of size effect. The increased concentration of micro meso pores in nanostructures act as obstacles for the transport of thermal energy. The 0.5 wt % DyCl_3 added ZnO was found to possess a ZT value of 0.05 at 935 K due to increment in carrier concentration and the reduced LTC by the increased concentration of micro-meso pores. The decrease in lattice thermal conductivity due to inhomogeneous pores and the increased grain boundaries as a result of nanostructuring emerged as an optimum criteria for the enhancement in ZT value.

References

- [1] E.S. Toberer, A. Zevalkink, G.J. Snyder, *J. Mater. Chem*, 21 (2011) 15843–15852.
- [2] M. Aldegunde, A. Martinez, J.R. Barker, *J. Appl. Phys*, 113 (2013).
- [3] M.G. Kanatzidis, *Chem. Mater.* 22 (2010) 648–659.
- [4] L. Edison Pizarro, G.R.B. Zoot, Z. José Echeverry, B.Í. Rojano, *Rev. MVZ Cordoba*. 18 (2013) 3672–3680.
- [5] K. Kishimoto, T. Koyanagi, *J. Appl. Phys.* 92 (2002) 2544–2549.
- [6] X. Liang, *Thermoelectric Transport Properties of Fe-Enriched ZnO with High- Temperature Nanostructure Refinement*, (2015).
- [7] L. Bertini, C. Stiewe, M. Toprak, S. Williams, D. Platzek, A. Mrotzek, Y. Zhang, C. Gatti, E. Müller, M. Muhammed, M. Rowe, *J. Appl. Phys.* 93 (2003) 438–447.
- [8] R.H. Tarkhanyan, D.G. Niarchos, *Int. J. Therm. Sci.* 67 (2013) 107–112.
- [9] J.Y. Hwang, E.S. Kim, S.W. Hasan, S.M. Choi, K.H. Lee, S.W. Kim, *Adv. Condens. Matter Phys.* (2015).

- [10] Hong, J. H.; Li, L. L.; Chen, D. Q.; Liu, H. Z.; Zheng, Li. Y.; Ding, J., *Powder Technology*, 189(3) (2009) 426-432.
- [11] I. Review, *E e, .*, 181 (1969).
- [12] E.D.M. Rowe, D. Ph, D. Sc, F. Group, *HANDBOOK*, 2006.
- [13] A. You, M.A.Y. Be, I. In, *Micro-Raman investigation of optical phonons in ZnO nanocrystals*, 124313 (2005).
- [14] K. S. W. Sing, D. H. Everett, R. A. W. Haul, L. Moscou, R. A. Pieroti, J. Rouquerol, T. Siemieniewska. *Pure Appl. Chem.* 57 (1985).
- [15] F. Schüth, K.S.W. Sing, J. Weitkamp (Eds.), *Handbook of Porous Solids*, Vol. 1, Wiley-VCH, Weinheim 2002.
- [16] S. Lowell, J. Shields, M. A. Thomas, M. Thommes, *Characterization of Porous Solids and Powders: Surface Area. Porosity and Density*, Springer, 2004.
- [17] J. Silvestre-Albero, A. M. Silvestre-Albero, P. L. Llewellyn, F. Rodriguez-Reinoso. *J. Phys. Chem. C* 117, 16885 (2013).
- [18] A. V. Neimark, F. Coudert, A. Boutin, A. Fuchs. *JPC Lett.* 1, 445 (2010).

Chapter 5

Studies on Dy Doped ZnO Thin Films for Thermoelectric Application

Objectives

Multifunctionality of oxide thin films as transparent conducting along with thermoelectric nature can be obtained through band filling. Band filling lead to the widening of optical band gap and the heavier effective mass for the improved thermoelectric properties.



5.1 Introduction

Wide band gap semiconductor metal oxides were frequently used for transparent applications such as light emitting diodes [1], solar cells [2], photo detectors [3] etc..Despite of this novel application they can contribute to the field of energy harvesting techniques such as thermoelectricity [4]. Thermoelectric materials are the emerging class of energy conversion process which can renovate waste heat in to electric energy as a promising technology for future power generation [5]. TE modules fabricated by sandwiching a n and p type TE materials can be formed either as bulk [6], bulk nanostructured [7] and even flexible class of thin films [8]. Thus TE modules were capable of converting a temperature gradient in to induce voltage without the requirement of any moving components and green house gas emission [9]. Generally thin film materials can be used for TE application due to its 2D confinement with increased density of states, along with enhanced carrier concentration and mobility. A TE material demands to be optically opaque due to their small band gap ($E_g \ll 2$ eV) which lead to higher electrical conductivity as by the conversion efficiency and as observed in $(\text{Bi,Sb})_2\text{Te}_3$ family [10], [11]. Non transparent TE materials such as telluride [12], half -heuslers [13] and silicides [14] possess attractive thermoelectric properties for renewable power generation application. A few optically transparent ($E_g > 3$ eV) TE materials are known to exist which opens a new fields in a range of novel applications such as smart windows and flat panel displays [15]. Optically transparent oxides tend to be electrical insulators, by their large electronic band gap due to the ionic character to the chemical bond and offers slighter electrical conductivity which leads to smaller value of ZT. Despite of this, TCOs are not only thermo chemically stable in air at high temperatures, their wide band gap hinders the transport of minority charge carriers thereby increasing the figure of merit (ZT) with increasing temperature up to the upper use temperature of each oxide [16]. Introducing impurities and dopants in the lattice, donor states can be positioned in the forbidden energy gap for modulating the electrical conductivity thereby able to withstand optical transparency for

its multifunctionality. The conversion efficiency of a TE material is defined to be

$$ZT = \frac{S^2\sigma}{\kappa}T \quad (5.1)$$

The transport parameters Seebeck coefficient (S), electrical conductivity (σ) and thermal conductivity (κ) for conventional crystalline systems are inter-related as they are strongly coupled through carrier concentration, scattering and band structure [17]. Thus it become difficult to control these variables independently for the enhancement of figure of merit. However, if the dimensionality of the material decreases, new variable of length scale become available to control their transport properties. Electronic structure modification through doping or manipulating nanostructures for larger density of states can be considered as a route for the enhancement of thermoelectric property. M.S Dresselhaus point out the enhancement of Seebeck coefficient by increased density of states while introducing low dimensional super lattices [18]. When bands are progressively filled with charge carriers through doping or increasing the temperature the band curvature get distorted and the corresponding effective mass increases. Due to the increment in effective mass band flattening will took place which further leads for the increased density of states [19]. The transport parameters S, σ and κ change independently with variation in density of state. However, it is well known that the optimal electronic performance of a thermoelectric semiconductor depends primarily on the weighted mobility which includes band effective mass. According to Bardeen-Shockly deformation potential theory [20] an increase of m^* due to band flattening at Fermi energy level lead to significant decrease in carrier mobility. Effective mass can be related to mobility through the relation $\mu = \frac{e\tau}{m^*}$ where m^* gives the effective mass and τ gives the scattering time which decreases with increase in effective mass [21]. As a result the optimal ZT value that depends on μ decreases the power factor in spite of the enhancement of Seebeck coefficient. Huiming Huang et.al reported the optical and electrical properties of nanocrystalline Dy doped ZnO thin films which were prepared by pulsed laser deposition. The decrease in resistivity

and enhancement of optical band gap due to Dy incorporation from 0.5 to 1 at% were reported [22]. In this chapter we report the multifunctionality of Dysprosium doped ZnO thin films as transparent conducting and as good TE material. Moreover we demonstrate the increased effective mass due to band flattening as a good criterion for improved thermopower along with optical enhancement.

5.2 Thin film fabrication

Crystalline Dysprosium doped Zinc oxide thin films were deposited on 10x10 mm glass substrate by RF magnetron sputtering. Before the deposition begins, the glass substrates were cleaned using distilled water followed by ultrasonic cleaning in acetone and finally dried in an oven. Micro powder with nominal composition was prepared by adding 0.5, 1 and 2 wt% Dy₂O₃ in single oxide powder of ZnO (Sigma Aldrich: 99.9% purity) by solid state reaction. The mixture was ball milled for 1 hour at a rpm of 350 to obtain a homogeneous mixture. The resultant mixture was pressed in to circular pellets of 50 mm diameter and 3 mm thickness using a hydraulic pelletizer with a pressure of 100 bar. The pellets were placed in an aluminum plate and used as sputtering cathode. The effects of sputtering power, pressure and substrate temperature were investigated and we optimized the sputtering conditions. Argon with 99.9% pure was used as the sputtering gas and the substrate to target distance was optimized to be 80 mm. The base pressure was maintained at 6×10^{-6} mbar before the entry of sputtering gas in to the chamber. All the films were sputtered at a power of 120 W with a substrate temperature of 200°C for 1 hour. To obtain a uniform film thickness a constant sputtering pressure of 3×10^{-2} mbar was maintained inside the chamber. The thickness of the sputtered film was determined using the quartz crystal monitor and it was found to be in the range of 600 nm. The films thus obtained by adding 0, 0.5, 1, 2 wt % of Dy₂O₃ in ZnO was named as F₁, F₂, F₃, F₄ thin films respectively. Table: 5.1 shows the optimized

Table 5.1: Optimized deposition parameters for pure and doped ZnO thin films

Sputtering Parameters	Specification
Fabrication technique	RF magnetron sputtering
Target	Dy doped ZnO powder target with 50 diameter and 3 mm thick
Substrate	Glass with dimension 10x10 mm
Sputtering gas	Argon having 99.9% purity
Target substrate distance	80 mm
Sputtering power	120 W
Substrate temperature	200 ⁰ C
Ultimate Vacuum	6x10 ⁻⁶ mbar
Working pressure	3x10 ⁻² mbar
Film thickness	≈ 600 nm

deposition parameter for the RF sputtering.

5.3 Results and discussion

5.3.1 XPS analysis

XPS analysis was done using Kratos AXIS ULTRA spectrometer which employs a monochromatic Al-K α X-ray source ($h\nu=1486.58$ eV) which was used at 150W (10 mA,15 KV). Fig: 5.1 shows the wide scan spectrum of elements present in the F₄ sample corresponding to their different binding energies. The energy of the photoelectrons excited from the sample is determined and this gives a spectrum with a series of photoelectron peaks of elements such as Dy, Zn and O. The numerical data (position, atomic concentration) obtained for the F₄ sample is given in Table: 5.2. XPS spectra was calibrated by taking the binding energy corresponding to C 1s peak at 285 eV. Atomic concentration of elements present in F₄ sample matches with the elemental composition determined from EDAX measurement.

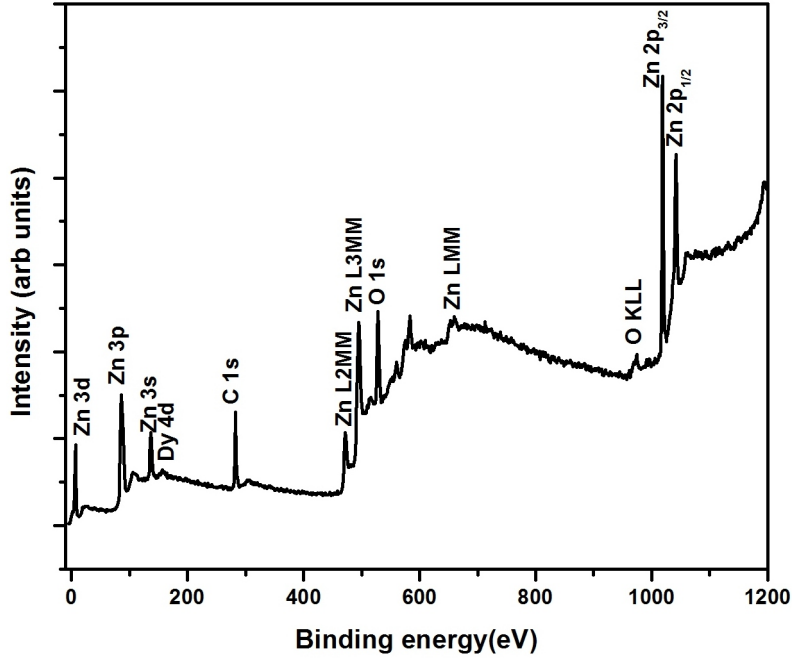


Figure 5.1: XPS full scan spectrum of F_4 sample.

The peaks corresponding to different binding energy were deconvoluted using the Gaussian-Lorentzian curve fitting method. The photoelectrons emitted from different atomic shell positions corresponding to each elements were determined. Table: 5.3 represents the high resolution deconvoluted peak position and the FWHM of the peaks corresponding to F_4 sample.

The deconvoluted peak for the zinc atom in F_4 sample was shown in Fig: 5.2. Differences in binding energy for the $2p_{3/2}$ and $2p_{1/2}$ peak of the zinc atom was found to be 23 eV irrespective of various doping elements.

The peak corresponding to O 1s can be deconvoluted to 3 peaks centered at 528.1 eV, 529.8 eV and 531.9 eV. The peak centered at 528.1 eV can be assigned to the presence of lattice oxygen in the wurtzite structure of hexagonal ZnO phase [24]. Depending on the higher doping level of Dy atom the intensity of peak centered at 529.8 eV increases which is associated with the O^{2-} ions in the oxygen deficient regions of the ZnO matrix. As the concentration of oxygen vacancy increases they act as electron donors in the conduction

Table 5.2: Data obtained from XPS spectrum for the F₄ sample

Elements	Binding energy (eV)	Atomic concentration(%)
Zn 2p	1019	77.96
O 1s	527	11.24
Dy 4d	156	0.65
C 1s	285	10.13

Table 5.3: Deconvoluted peak position corresponding to Zn, O and Dy

Peak	Binding energy(eV)	FWHM
Zn 2p _{3/2}	1019.07	2.91
Zn 2p _{1/2}	1042.03	3.3
Zn 3d	7.02	2.91
Zn 3p	86.05	5.23
Zn 3s	136.9	3.42
O I 1s	528.1	1.09
O II 1s	529.8	1.93
O III 1s	53.19	1.08
Dy 4d _{5/2}	154.8	10.4

band and contribute for the conduction mechanism. Along with additional free charge carriers that originate from the Dy³⁺ cation, these oxygen vacancies can enhance the electrical conductivity. This enhancement took place without any deterioration in the band structure there by maintaining an optimum thermopower. The presence of lowest intensity peak at 531.9 eV for the F₄ sample can be explained due to the formation of chemisorbed oxygen impurity such as adsorbed O²⁻ [25]. The evolution of peak at 154.8 eV points out the presence of Dy ion and the photoemission took place from 4d_{5/2} core shell. This is in complete agreement with the trivalent oxidation state of Dysprosium ion [26].

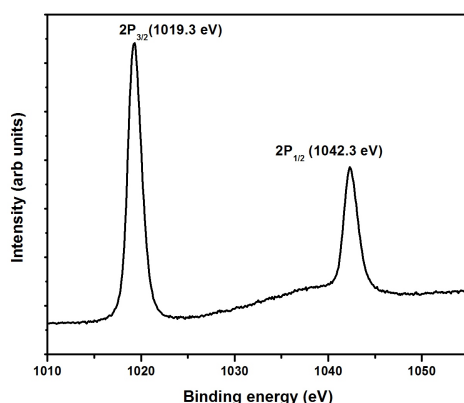


Figure 5.2: Deconvoluted XPS peak corresponding to Zn 2p for the F₄ sample.

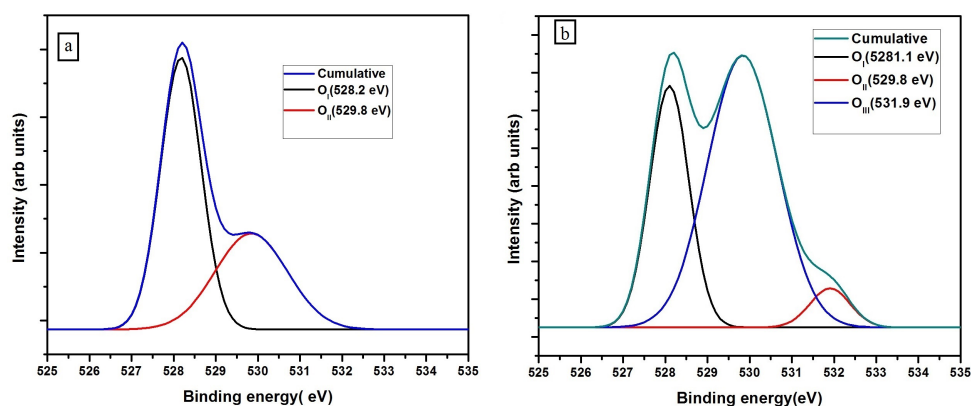


Figure 5.3: XPS spectrum corresponding to O 1s peak for a) F₁ b) F₄ sample.

5.3.2 EDAX analysis

The elemental compositions of the prepared thin film samples were determined using the EDAX spectrum. EDAX spectrum reveals the presence of Dy ion in the doped samples. Table: 5.4 depicts the atomic and weight % of each element corresponding to different composition of Dy doping in ZnO.

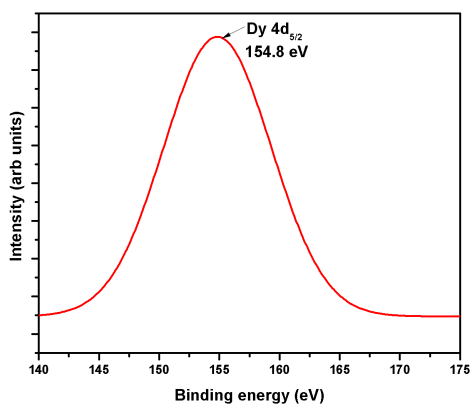


Figure 5.4: XPS spectrum of $4d_{5/2}$ peak corresponding to F_4 sample.

5.3.3 XRD analysis

The XRD pattern for the pure and doped ZnO thin films are depicted in Fig: 5.5. The crystal structure and growth orientation of the films were obtained by Rigaku Miniflex 600 having Cu-K α spectral line (1.54\AA) with $\theta - 2\theta$ geometry. The films were rastered with a scanning speed of $10^0/\text{min}$ having a step size of 0.02^0 collected in a range 20 to 80^0 at 2θ angle. The diffracted X-ray peaks are well matching with the ICDD card no: 00-005-0664 and substantiate the formation of ZnO with $P6_3mc$ space group [24]. A strong peak at 34^0 for all the prepared samples corresponds to the (002) plane of the hexagonal wurtzite structure. As shown in the Fig: 5.5 the number of diffraction peak and peak intensity of (002) plane varies depending on the concentration of dopant element. The XRD pattern for the pure ZnO film possess additional 3 peaks at $2\theta = 36.08^0$, 62.55^0 and 72.24^0 corresponding to (101), (103) and (004) plane. These peaks can also be indexed to the hexagonal wurtzite structure of ZnO and the formation of multiple peaks show the polycrystalline nature of the films. Randomly oriented grains in F_1 , F_2 , F_3 seize lower peak intensity corresponding to (002) plane. For the F_4 sample the growth mainly took place along the c axis and thus the major electron density contribution arise from (002) and (004) plane. No additional peaks corresponding to Dy_2O_3 were present in the coated samples. Change

Table 5.4: Elemental composition for Dy doped ZnO

Sample	Element	Weight (%)	Atomic (%)
F ₁	Zn K	76.71	44.63
	O K	23.29	55.37
F ₂	Zn K	75.15	42.65
	O K	24.69	57.27
	Dy L	0.16	0.08
F ₃	Zn K	74.29	42.32
	O K	24.68	57.45
	Dy L	1.03	0.24
F ₄	Zn K	73.96	42.74
	O K	24.05	56.80
	Dy L	1.99	0.46

in the lattice parameter can be depicted from the shift in 2θ value to higher angles as shown in Fig: 5.6. Moreover the peaks get preferred oriented along c axis. This shows that dopants induce strain in the lattice.

Grain growth kinetics of thin film depends on interfacial, surface and stress energies [27]. Once the film was deposited the interfacial energy barrier will be crossed and the entire energy of the film predominates by the surface energy. In pure ZnO, the growth took place along different plane and it is randomly oriented. At elevated deposition temperatures where low-strain growth occurs, surface and interfacial-energy minimization dominates grain growth. When the adatom corresponding to Dy^{3+} ion reach the island, the surface energy decreases and the strain energy dominates over the film growth. There occur a competition between the surface and strain energy during the growth of the film. As the doping % increases the strain energy predominates and the growth took place in a plane with lowest strain energy to minimize the energy of the film. For the F₄ film the growth took place

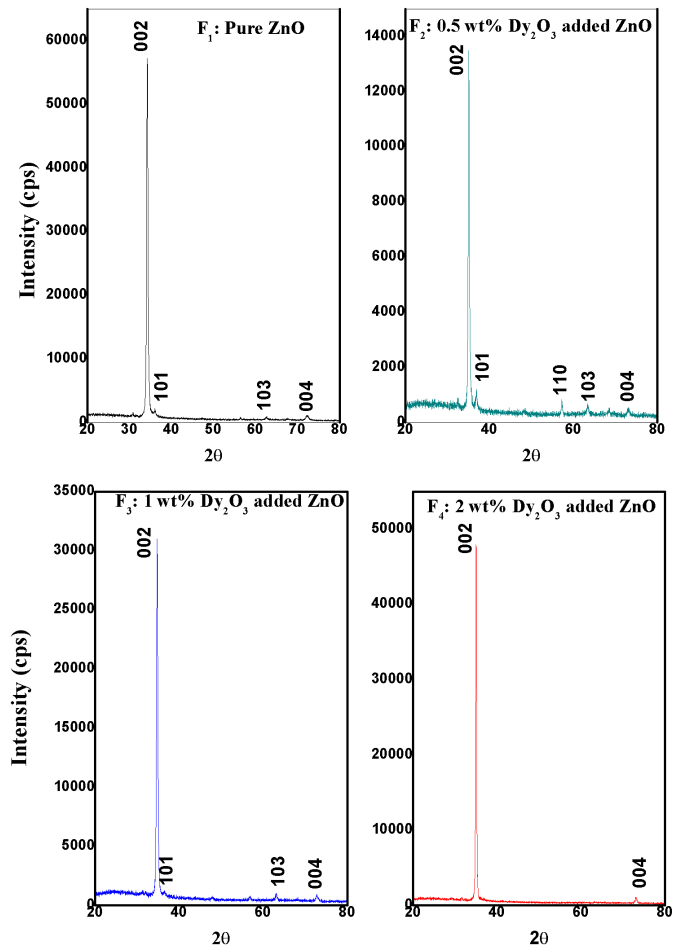


Figure 5.5: XRD pattern for the pure and Dy doped ZnO.

along the (002) and (004) plane which is considered to have lower strain energy.

5.3.4 SEM analysis

The surface morphology of the deposited films was obtained using field emission spectroscopy (FESEM) Carl Zeiss Supara 55. The thin films were Au sputtered to obtain proper electrical conduction. The films consist of polygonal grains that are densely packed and randomly oriented normal to the substrate plane. Apart from the interfacial energy the surface energy

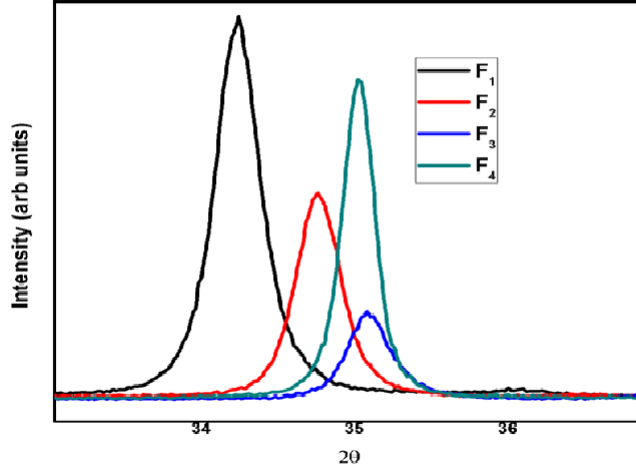


Figure 5.6: Shift observed for the peak corresponding to (002) plane.

for the pure ZnO imparts growth along different planes. As the Dy doping increases the radius of curvature for the grain boundary segment get deteriorated due to the strain energy and the particle size get decreased. The average particle size decreases from 300 nm to 100 nm. The driving force for grain growth is the reduction for Gibbs free energy (ΔG) per unit motion of a unit area of grain boundary. Migration forces can be exerted by reduction in interfacial area by changing the grain boundaries. The motion of grain boundary is driven by reduction of its own curvature with a driving force F , defined as:

$$F = -\gamma\left(\frac{1}{r_1} + \frac{1}{r_2}\right) \quad (5.2)$$

where γ is the specific energy of the boundary and r_1 , r_2 represents the radii of curvature of the grain boundary. For the F_4 sample along with surface energy the strain energy predominated and the radius of curvature for the grain boundary decreases as depicted in Fig: 5.7. The unwilling competition between the surface and strain energy contribute towards the observed change in the texture as the exposed surface try to minimize the overall strain energy of the lattice. The average particle size determined from SEM and AFM analysis complement with each other.

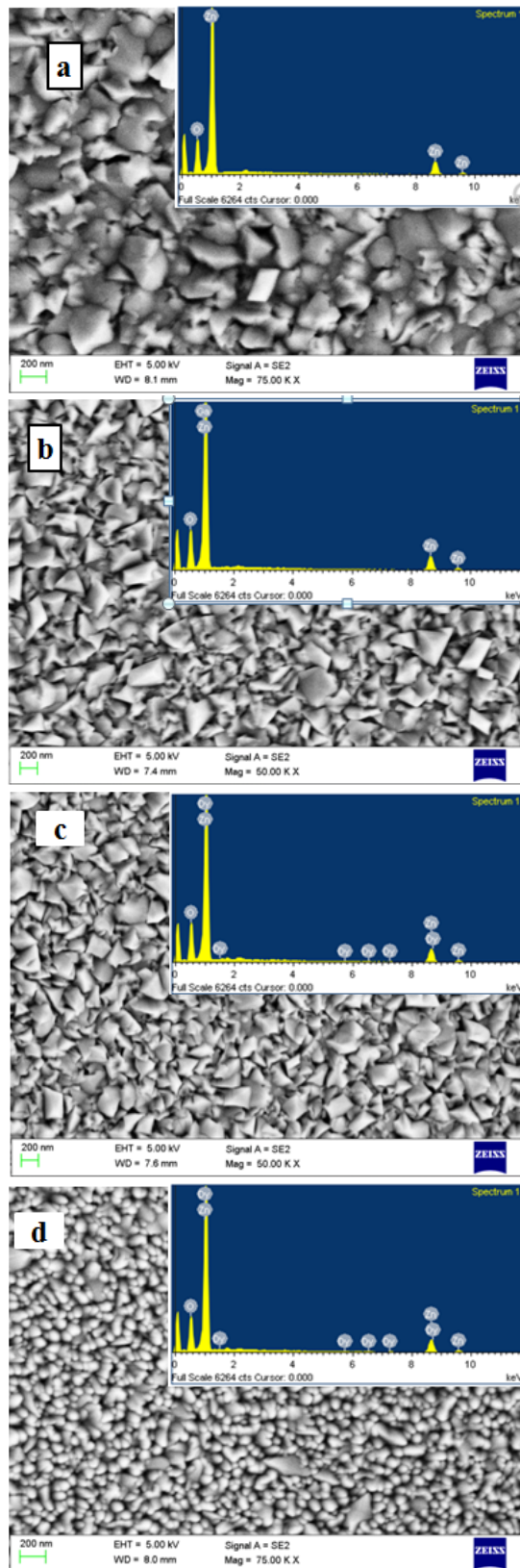


Figure 5.7: SEM micrographs of a) F₁, b) F₂, c) F₃, d) F₄.

5.3.5 AFM analysis

The surface topography and texture of the film can be examined using Atomic force microscopy. It measures the surface irregularities or non uniformity of the planes in the surface. Highly doped single crystal silicon probes were used as the tip of cantilever with a force constant of 42 N/m and resonant frequency of 310 kHz . The scans were performed in an area of $3 \mu\text{m} \times 3 \mu\text{m}$ with a scanning rate of 1 Hz. The AFM images were analyzed by image processing tool to obtain the surface and textural features. The average roughness R_a measures the vertical deviation of surface points from an average plane [28]. Fig: 5.8 represents the topography and Table: 5.8 depicts the particle size and the average roughness (R_a) of the sputtered thin film.

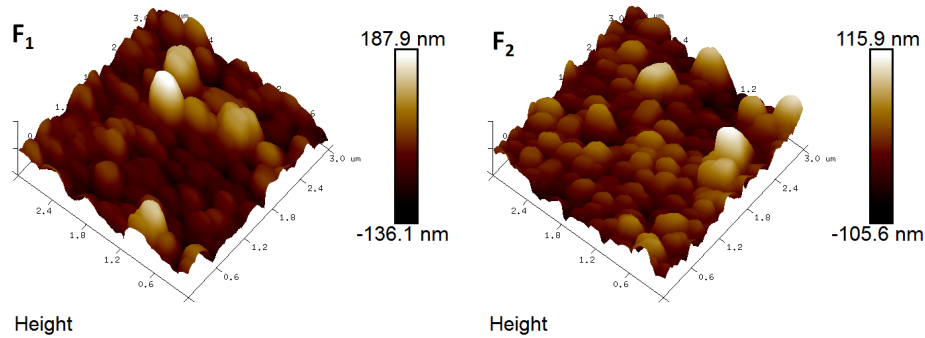


Table 5.5: Determination of particle size and roughness of the coated thin film

Sample	Particle size (nm)	Roughness (nm)
F ₁	314	33.70
F ₂	241	23.00
F ₃	160	8.30
F ₄	98	6.88

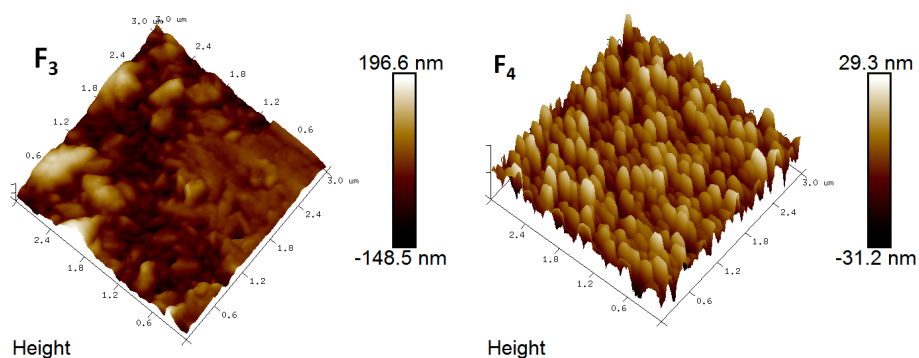


Figure 5.8: 3D AFM images of a) F_1 , b) F_2 , c) F_3 , d) F_4 sample.

The scattering sites and traps in the surface determine the transport properties of charge carriers. The surface roughness of the pure and Dy doped ZnO thin films decreases from 25.87 nm to 3.12 nm. The decrease in roughness caused by the decrement in particle size. The surface of pure ZnO found to possess broadened hills and valleys. As the doping % increases the increased stress in the lattice reduce the radius of curvature of the grain boundaries and the surface roughness gets reduced. The grain boundary does not diffuse each other which resulted in the formation of densely packed grains with definite boundaries. The increased number of grain boundaries results in the scattering of charge carriers and thus mobility decreases. The growth mechanism in F_4 sample causes the decrement in the mobility of free charge carriers due to grain boundary scattering and lead to the decline of electrical conductivity.

5.3.6 Optical properties

UV-Visible spectroscopy

ZnO being a wide band gap semiconductor its show a good light transmission property. By attributing the host ZnO matrix with Dy ion the spectral distribution of transmission in the visible region get enhanced. Optical transmittance spectra in Fig: 5.9 clearly show that doping can enhance the

transmittance of ZnO. The F₄ thin film posses a maximum transmittance of 97% and exhibit interference fringe patterns in the visible region. The reason

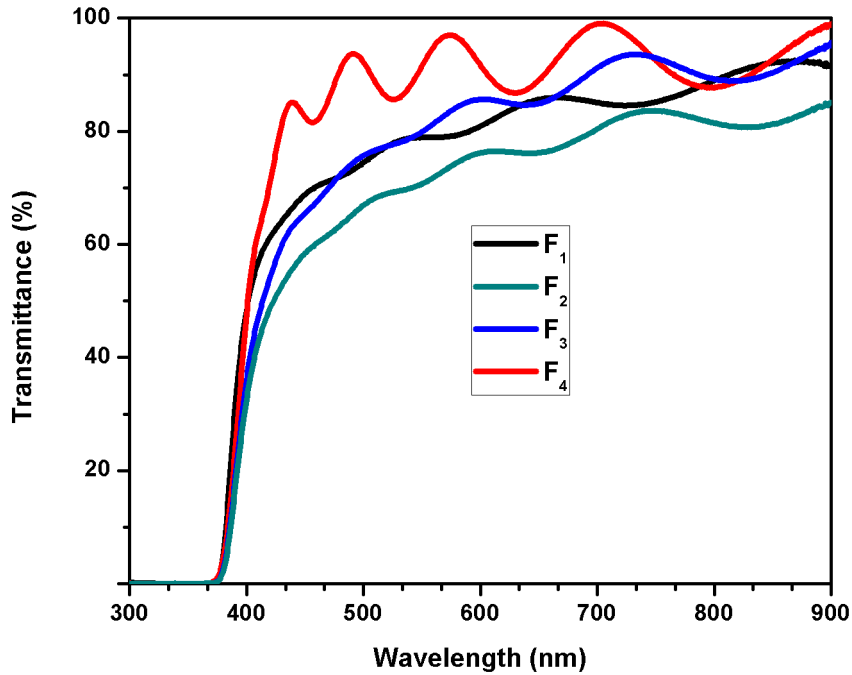


Figure 5.9: Transmission spectrum for Dy doped ZnO thin films.

for enhanced optical transmission property in doped semiconductor can be explained by determining the band gap energy using the Tau'c plot relation. The optical direct band gap energy was determined using the absorption coefficient α defined as

$$\alpha h\nu = A(h\nu - E_g)^{1/2} \quad (5.3)$$

where A is the proportionality constant ; $h\nu$ is the photon energy calculated in eV and E_g refers to the direct band gap of the material [29]. The linear region of the graph is extrapolated to the photon energy axis which defines the optical band gap of the material at which absorption becomes zero and it is shown in Fig: 5.10. The reason for widening of optical band gap was due to the band filling model proposed by Burstein and Moss. The apparent optical band gap E_g due to Burstein Moss effect will have contribution from

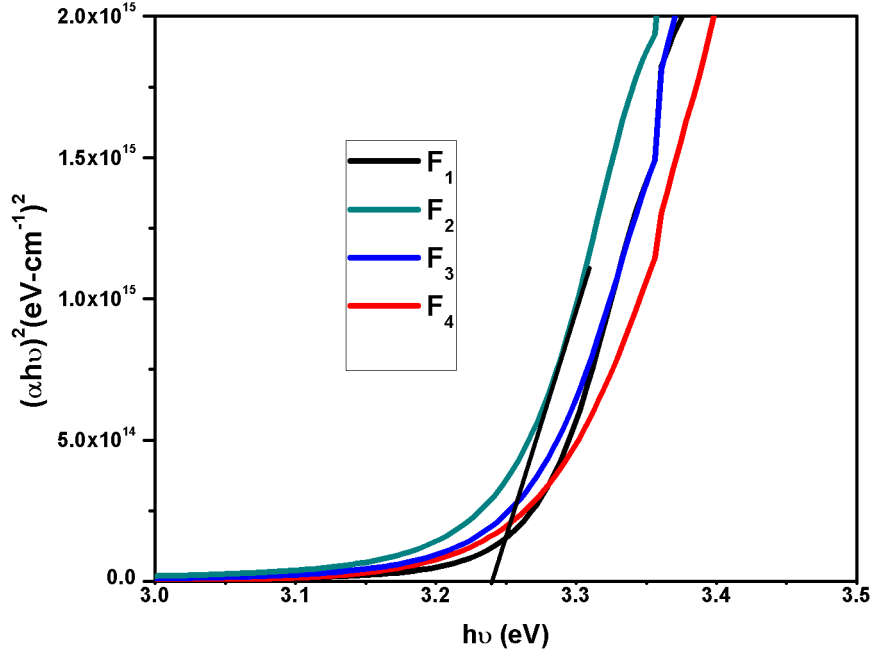


Figure 5.10: Variation of optical band gap for Dy doped ZnO thin films.

the inherent free charge carriers (E_0) and due to the donor atoms (ΔE_{BM}) which are responsible for the band filling [30].

$$E_g = E_0 + \Delta E_{BM} \quad (5.4)$$

In ZnO, considering the single parabolic band model the energy shift due to carrier concentration 'n' can be defined according to the relation:

$$\Delta E_{BM} = \frac{\hbar^2}{8m^*} \left(\frac{3n}{\pi} \right)^{2/3} \quad (5.5)$$

For heavier doped materials there occurs a discrepancy in the calculated optical band gap with the experimentally observed and this can be explained due to the variation in effective mass. For semiconductors with low carrier concentration the dispersion of Eigen states close to the conduction and valence band possess a single parabolic band model with energy

$$E = \frac{\hbar^2 k^2}{2m_c} \quad (5.6)$$

with m_c defines curvature effective mass of conduction band and k defines the wave vector. In materials with high carrier concentration (greater than band carrier density) or at high temperature the dispersion of eigen states at the band extrema will be larger and the effective mass has to incorporate the non parabolic effects with non linear dependence on energy as

$$\frac{\hbar^2 k^2}{2m} = E + \alpha E^2 + \beta E^3 \quad (5.7)$$

where m is the transport effective mass at the band edge. Keeping the first non linear term gives the single Kane Band dispersion relation

$$\frac{\hbar^2 k^2}{2m} = E + \alpha E^2 \quad (5.8)$$

The term α defines the non parabolicity of bands due to band flattening as the eigen state energy deviates from the band edge energy [31]. When bands are gradually filled with charge carriers through doping, photo excitation or increasing the temperature, corresponding effective mass varies and this changes the electron and hole mobility [32]. This variation in transport properties are in contradictory with the parabolic band model where effective mass is a constant and independent of carrier concentration. The extent to which the effective mass increases with carrier concentration depends on the band filling or the non parabolicity of bands. From the shift of optical absorption band edge the effective mass and non parabolicity can be determined. Band filling can be measured experimentally via Burstein Moss shift when the carrier concentration of electrons exceeds the band carrier density and occupy the lowest states in the conduction band. The conduction band carrier density for the pure ZnO can be defined by the Fermi Dirac distribution function $N_c = 2 \left(\frac{2\pi m^* k_B T}{h^2} \right)^{3/2}$ where m^* defines the effective mass of conduction band. For an effective mass of $0.25m_e$ the conduction band carrier density was found to be $5.6 \cdot 10^{18} \text{cm}^{-3}$ [33]. Carrier density beyond this concentration non parabolicity of bands became significant and Fermi level moves above the conduction band edge termed to be the Burstein Moss shift [34]. As a result the interband transitions corresponds to the excitation

of valence band electrons in to the empty states above the minimum of the conduction band causes widening of band. Optical transparency was retained and enhanced, throughout the material due to the non parabolicity of bands caused by the increase in effective mass above a critical carrier concentration.

5.3.7 Electrical properties

Hall measurement

Room temperature electrical properties of ZnO and Dy doped ZnO thin films were measured using Hall measurement and the results were listed in Table: 5.6. Electron concentration increased from $3.69 \times 10^{18} \text{cm}^{-3}$ in pure ZnO to $1.43 \times 10^{20} \text{cm}^{-3}$ corresponding to Dy doped ZnO sample. The increase in carrier concentration is due to substitution of excess free electron from the Dy^{3+} ion. Due to the variation in ionic radii of Dy and Zn ion, incorporation of the dopant also lead to the formation of interstitial Dy ion contributing 3 electrons in to the host lattice which cause drastic increment in carrier concentration for the F_4 sample. Moreover the increment in carrier concentration lead to the reduction in mobility and cause deterioration in electrical conductivity. The negative Hall coefficient depicts electrons are the majority charge carriers.

Table 5.6: Electrical properties for different Dy concentration in ZnO

Sample	Hall concentration (cm^{-3})	Carrier mobility (cm^2/Vs)	Conductivity (Scm^{-1})
T1	-5.35×10^{17}	2.058	0.18
T2	-5.83×10^{18}	2.38	2.22
T3	-8.82×10^{18}	1.20	1.70
T4	-1.43×10^{20}	0.07	1.64

5.3.8 Thermoelectric measurement

Thermopower

The measured Seebeck coefficient, electrical conductivity and the calculated power factor as a function of temperature were plotted. From the optical studies it was found that the doped ZnO samples are degenerate, their band structure found to be non-parabolic and it can be described by the SKB model. For degenerate semiconductors the Seebeck coefficient can be defined by the Mott's relation:

$$S = -\frac{8\pi^2 k_B^2 m^* T}{3eh^2} \left(\frac{\pi}{3n}\right)^{2/3} \quad (5.9)$$

where k_B is the Boltzmann constant, e is the charge of electron, m^* gives the effective mass, h is the Planck constant and n defines the charge carrier concentration. The effective mass m^* of the band is related to the curvature of bands and can be modified by distorting the band [41]. Due to the increased carrier concentration through doping the band filling in the conduction band will occur and resulted in heavier effective mass. This can increase the density of states at the Fermi level and thereby increase the thermopower. The value of Seebeck coefficient compete between the increased density of state and decrement in mobility due to the heavier effective mass caused by the non-parabolicity of band structure. The negative Seebeck coefficient ensured that electrons are the majority free charge carriers. As shown in Fig: 5.11 for the Dy doped samples the thermopower decreases due to the increased carrier concentration. The F_4 film possess the higher thermopower among the doped samples due to the heavier effective mass as per the Mott's relation.

Heavier effective mass lead to the enhanced scattering of charge carriers by phonons and electrons. The decrement in mobility due to higher scattering rates resulted in the deterioration in electrical conductivity although it possess higher carrier concentration. As observed in Fig: 5.12 the electrical conductivity is much low for the F_4 sample as though it possess the higher carrier concentration. From the morphological analysis it was evident

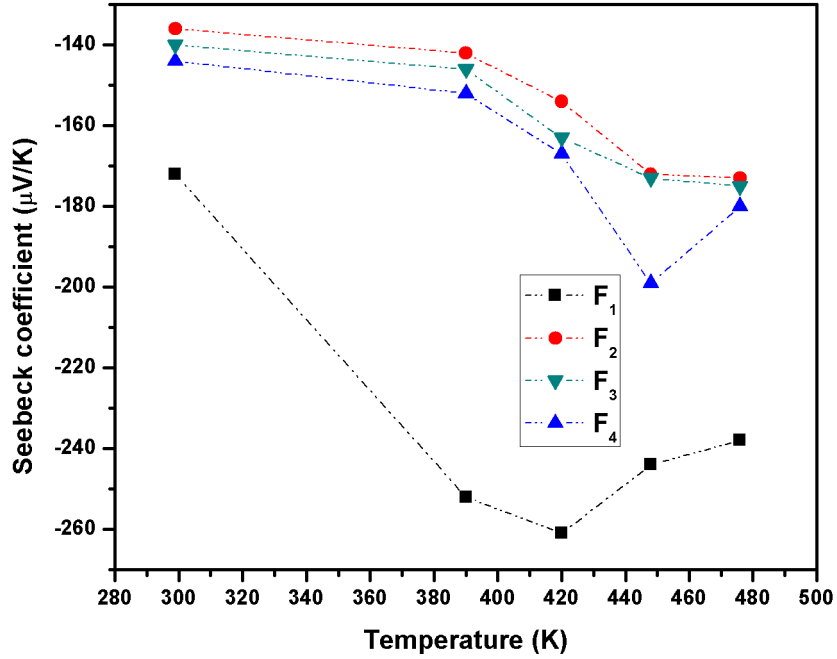


Figure 5.11: Variation of Seebeck coefficient with temperature for Dy doped ZnO.

that as the grain size decreases the scattering rates at the grain boundary increases and resulted in pronounced scattering mechanism. The power factor (PF), which depicts the energy stored for the thermoelectric performance was calculated and shown in Fig: 5.13. Despite the larger m^* and higher Seebeck coefficient, there is a decline of μ leading to a net decrease of power factor which was observed for the F₃ and F₄ samples while retaining a transparency around 97%. F₂ sample was found to possess much higher power factor compared to other doped films. All the Dy doped ZnO thin films possess increased power factor at higher temperature than pristine ZnO. Hence it was experimentally proven that the TE properties can be enhanced at higher temperature without deterioration in the optical properties due to the non-parabolicity of band structure through doping.

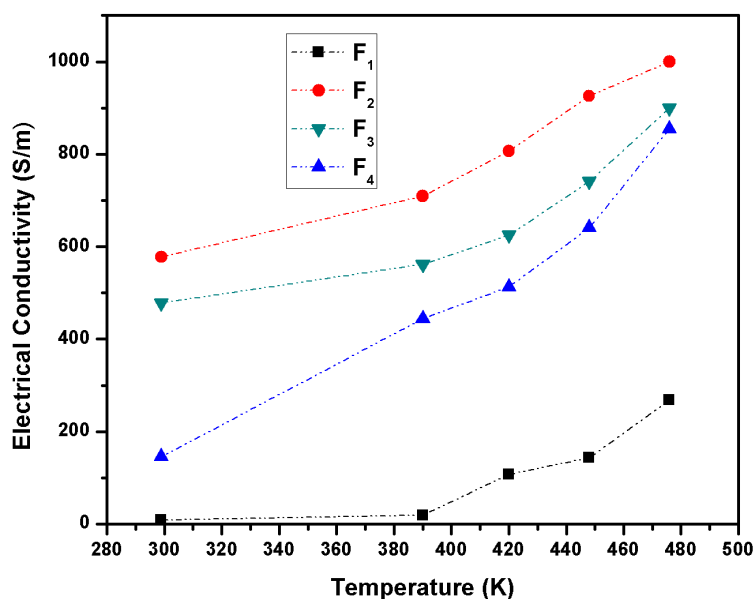


Figure 5.12: Variation of electrical conductivity with temperature for Dy doped ZnO.

5.4 Conclusions

Dysprosium doped Zinc oxide thin films with optimized band gap and enhanced power factor can be used as a potential candidate for both transparent conducting and thermoelectric application at moderate temperatures. Multifunctionality of the thin films can be achieved by the non parabolicity of band structure due to heavier effective. The modified band structure results in the apparent widening of the optical band gap and improved the transmittance in the visible region. The increased strain energy in the lattice due to Dy incorporation results in the orientation of planes along low strain energy and it was confirmed by the XRD analysis. SEM microscopy substantiates the decrement in particle size with doping and the shift of grain growth from randomly oriented planes to the growth along *c* axis. AFM analysis determines the surface roughness and it decreases with increase in doping. The decrease in roughness will reduce the mobility of charge carriers across the grain boundaries due to the enlarged scattering mechanism. XPS and EDAX

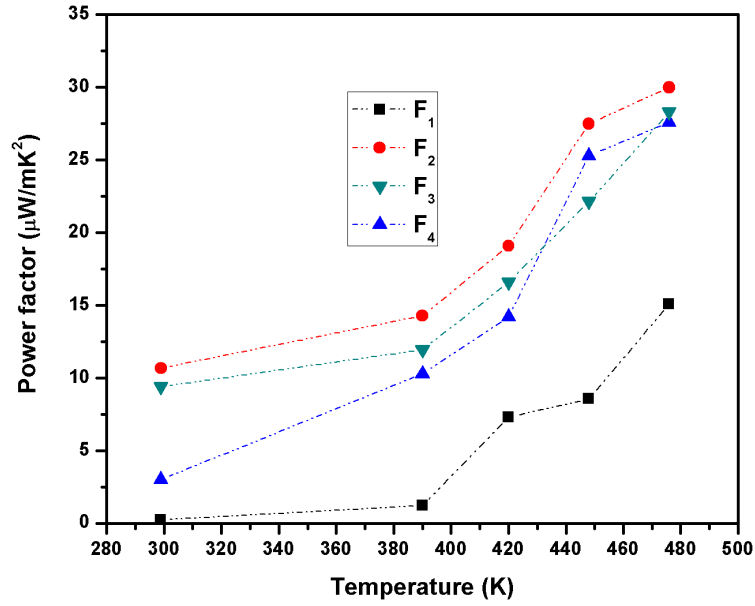


Figure 5.13: Variation of power factor with temperature for Dy doped ZnO.

analysis ensured the presence of Dy ion in the doped sample and the presence of peak at 154.8 eV confirmed the trivalent oxidation state of Dysprosium. This work explored the use of non-parabolic band structure in wide band gap oxide materials for its multifunctionality. The heavier effective mass at the conduction band edge results for the enlarged thermopower as it is directly related for the degenerate semiconductor. Improvement in the effective mass deteriorated the mobility and cause reduction in the electrical conductivity although it had large carrier concentration. However, the multifunctionality of the Dy doped ZnO thin films shows higher power factor compared to pristine ZnO. Among the doped samples 0.16 wt% Dy doped ZnO sample posses the good light transmittance with the highest power factor and it is considered to be suitable for optoelectronic as well as thermoelectric applications.

References

- [1] Y. Nagasawa, A. Hirano, *Appl. Sci.* 8 (2018) 1264.
- [2] M. Grätzel, *J. Sol-Gel Sci. Technol.* 22 (2001) 7–13.
- [3] H. Xue, X. Kong, Z. Liu, C. Liu, J. Zhou, W. Chen, S. Ruan, Q. Xu, *Appl. Phys. Lett.* 90 (2007) 8–11.
- [4] E.N. Hurwitz, M. Asghar, A. Melton, B. Kucukgok, L. Su, M. Oroc, M. Jamil, N. Lu, I.T. Ferguson, *J. Electron. Mater.* 40 (2011) 513–517.
- [5] S. LeBlanc, *Sustain. Mater. Technol.* 1 (2014) 26–35.
- [6] M. Sondergaard, E.D. Bøjesen, K.A. Borup, S. Christensen, M. Christensen, B.B., *Acta Mater.* 61 (2013) 3314–3323.
- [7] P. Jood, R.J. Mehta, Y. Zhang, T. Borca-Tasciuc, S.X. Dou, D.J. Singh, G. Ramanath, *RSC Adv.* 4 (2014) 6363–6368.
- [8] X. Chen, W. Dai, T. Wu, W. Luo, J. Yang, W. Jiang, L. Wang, *Coatings.* 8 (2018) 244.
- [9] P.P. Pradyumnan, A. Paulson, N.A. Muhammed Sabeer, N. Deepthy, *AIP Conf. Proc.* 1832 (2017) 2–5.
- [10] H. Zou, D.M. Rowe, G. Min, *J. Cryst. Growth.* 222 (2001) 82–87.

- [11] G. Thankamma, A.G. Kunjomana, *Cryst. Res. Technol.* 49 (2014) 212–219.
- [12] H. Bark, J.-S. Kim, H. Kim, J.-H. Yim, H. Lee, *Curr. Appl. Phys.* 13 (2013) S111–S114.
- [13] H. Compounds, *Recent Advances in Nanostructured Thermoelectric Half-Heusler Compounds*, (2012) 379–412.
- [14] M.I. Fedorov, G.N. Isachenko, *Jpn. J. Appl. Phys.* 54 (2015).
- [15] C. Yang, D. Souchay, M. Kneiß, M. Bogner, H.M. Wei, M. Lorenz, O. Oeckler, G. Benstetter, Y.Q. Fu, M. Grundmann, *Nat. Commun.* 8 (2017) 4–10.
- [16] M. M A, I. Sudin, A. Mohd Noor, S. Rajoo, U. M B, N. H. Obayes, M. Firdaus Omar, *Int. J. Eng. Technol.* 7 (2018) 27.
- [17] A.F. Ioffe, *Semiconductor thermoelements and thermoelec*, *Phys. Today.* 12 (1959) 42.
- [18] M.S. Dresselhaus, G. Chen, M.Y. Tang, R. Yang, H. Lee, D. Wang, Z. Ren, J.P. Fleurial, P. Gogna, *Adv. Mater.* 19 (2007) 1043–1053.
- [19] L.D. Whalley, J.M. Frost, B.J. Morgan, A. Walsh, *Phys. Rev. B.* 99 (2019).
- [20] J. Bardeen, W. Shockley, *Phys. Rev.* 80 (1950) 72–80.
- [21] Y. Pei, A.D. Lalonde, H. Wang, G.J. Snyder, *Energy Environ. Sci.* 5 (2012) 7963–7969.
- [22] H. Huang, Y. Ou, S. Xu, G. Fang, *Properties of Dy-doped ZnO nanocrystalline thin films prepared by pulsed laser deposition*, 254 (2016) 2013–2016.

- [23] N.A.M. Sabeer, A. Paulson, P.P. Pradyumnan, *J. Appl. Phys.* 124 (2018).
- [24] N.K. Divya, P.P. Pradyumnan, *Mater. Sci. Semicond. Process.* 41 (2016) 428–435.
- [25] G.A.S. Josephine, A. Sivasamy, *Environ. Sci. Technol. Lett.* 1 (2014) 172–178.
- [26] R. Al-Gaashani, S. Radiman, A.R. Daud, N. Tabet, Y., *Ceram. Int.* 39 (2013) 2283–2292.
- [27] K. Barmak, J. Kim, C.S. Kim, W.E. Archibald, G.S. Rohrer, A.D. Rollett, D. Kinderlehrer, S. Ta’Asan, H. Zhang, D.J. Srolovitz, *Scr. Mater.* 54 (2006) 1059–1063.
- [28] B. Rajesh Kumar, T. Subba Rao, *Dig. J. Nanomater. Biostructures.* 7 (2012) 1881–1889.
- [29] J. Hays, K.M. Reddy, N.Y. Graces, M.H. Engelhard, V. Shutthanandan, M. Luo, C. Xu, N.C. Giles, C. Wang, S. Thevuthasan, A. Punnoose, *Journal of Physics: Condensed Matter* 19 (2007) 266203.
- [30] Z.M. Gibbs, A. Lalonde, G.J. Snyder, *New Journal of Physics* 15 (2013) 075020.
- [31] L.D. Whalley, J.M. Frost, B.J. Morgan, *A. Phys. Rev. B.* 99 (2019) 085207.
- [32] D.C. Reynolds, C.W. Litton, and T.C. Collins, *Phys. Star. Solidi* 12 (1965) 3.
- [33] J.O. Barnes, D.J. Leafy and A.G. Jordan, *J. Electrochem. Soc.*, 7 (1980) 1636.

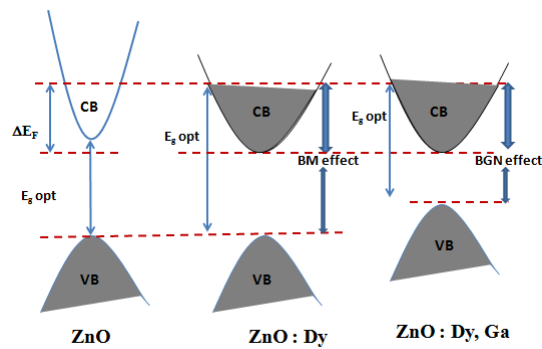
- [34] H.Odaka, Y. Shigesato, T. Murakami, and S.Iwata, Japanese Journal of Applied Physics, 40 (2001) 3231.
- [35] S. Sagadevan, J. Podder, Soft Nanosci. Lett. 5 (2015) 55–64.
- [36] N.R. Yogamalar, A. Chandra Bose, Appl. Phys. A Mater. Sci. Process. 103 (2011) 33–42.
- [37] K.G. Saw, N.M. Aznan, F.K. Yam, S.S. Ng, S.Y. Pung, PLoS One. 10 (2015) 1–17.
- [38] A.P. Roth, J.B. Webb, D.F. Williams, Solid State Commun. 39 (1981) 1269–1271.
- [39] C.I. Bright, Review of Transparent Conductive Oxides (TCO), 50 Years Vac. Coat. Technol. (2007) 38.
- [40] I. Review, E e, ., 181 (1969).
- [41] A. Paulson, N.A. Muhammed Sabeer, P.P. Pradyumnan, J. Alloys Compd. 786 (2019) 581–587.

Chapter 6

Studies on Dual Doped (Dy,Ga) ZnO for Thermoelectric Applications

Objectives

Dy and Ga dual doped ZnO thin films were fabricated by RF magnetron sputtering. Reconstruction of bands due to the increased carrier concentration lead to the enhancement in TE properties.



6.1 Introduction

The quest on efficient TE materials lead us to fabricate dual doped thin films for thermoelectric application. Over the last decade the researches were primarily focus on the decreases in lattice thermal conductivity by nano structuring for the enhancement of thermoelectric figure of merit [1]. Nanostructured grain boundaries scatter phonons without disturbing the power factor ($S^2\sigma$) of the thermoelectric materials. This chapter focus on the enhancement in power factor of the TE material which is also important for maximizing the ZT. The tradeoff between Seebeck coefficient and electrical conductivity depends on carrier concentration, band structure and scattering [3]. As the carrier concentration increases the heavier effective mass lead to the increased density of states at the Fermi level which will enhance the thermopower. At the same time increased carrier concentration reduce the mobility of charge carriers which results in decrement in electrical conductivity. The state of the art lies on the independent enhancement method of Seebeck coefficient without deteriorating the electrical conductivity contribution. Reconstruction of band structure will lead to the formation of multivalley bands with independent Seebeck coefficient and preserving the mobility of charge carriers along the band.

Harmonic control in TE properties in favour of high figure of merit through single doping found to be difficult due to the low solubility limit of the dopant. Moreover the excessive dopant content creates secondary phases which lead to the deterioration of carrier transport properties. It was found that dual doping makes significant improvement in the thermoelectric properties. The use of dual dopants, one ion of which has smaller size than Zn^{2+} ion (0.074 nm) while the other one have higher size than Zinc ion . Most of the published literatures regarding thermoelectricity include the use of dual dopants for the enhancement of thermoelectric figure of merit. The work include Al^{3+} - Mg^{3+} doped bulk ZnO [3], Al^{3+} - Ga^{3+} doped bulk ZnO [4] and Ga^{3+} - In^{3+} doped ZnO superlattices [5]. In this work we choose Ga (0.064 nm) and Dy (0.08 nm) ions to be doped in the ZnO lattice to obtain a harmonic

control in crystal quality for good electrical and transport properties. The increased carrier concentration due to dual doping lead to a band gap shift expected from the free electron model. This lead to the apparent widening of the optical band gap termed to be the Burstein Moss shift (BM effect) [6]. Band filling resulted in heavier effective mass which cause a non parabolicity in the band structure. Discrepancy in band gap after the Mott's critical concentration can be explained by renormalization model where the band gap narrowing (BGN effect) will occur [7]. BGN is considered as a result of mutual exchange and coulomb interaction between the added free electrons in the conduction band [8]. This lead to the upliftment of valence band maximum (VBM) and decrement in conduction band minimum (CBM). The net change in E_g due to these two contribution can be represented as

$$\Delta E_g = \Delta E_{BM} - \Delta E_{RN} \quad (6.1)$$

As discussed in the previous chapter the non parabolicity in the band structure can be achieved through the incorporation of 1 and 2 wt% of Dy in ZnO lattice. Although the carrier concentration found to be high for 2 wt % of Dy doping, the highest power factor is for the 1 wt % Dy doping in ZnO. In this chapter we are discussing about the structural and thermoelectric properties of Ga ions added in to 1 wt % Dy doped ZnO sample. Moreover the renormalization of the band structure was also discussed.

6.2 Thin film fabrication

Crystalline Dysprosium and Gallium doped Zinc oxide thin films were deposited on 10x10 mm glass substrate by RF magnetron sputtering. Before the deposition begins, the glass substrates were cleaned using distilled water followed by ultrasonic cleaning in acetone and finally dried in an oven. As an extension of our previous work 1, 3 and 5 wt % of Ga_2O_3 was added to 1 wt % Dy doped ZnO powder. The resultant powder was ball milled for 1 hour at an rpm of 350 to obtain a homogeneous solid solution. Uniform powder

Table 6.1: Optimized deposition parameters for the RF sputtering

Sputtering Parameters	Specification
Fabrication technique	RF magnetron sputtering
Target	Dy and Ga doped ZnO powder target with 50x3 mm size
Substrate	Glass with dimension 10x10 mm
Sputtering gas	Argon with 99.9% purity
Target substrate distance	80 mm
Sputtering power	120 W
Substrate temperature	250 ⁰ C
Ultimate Vacuum	6x10 ⁻⁶ mbar
Working pressure	2.5x10 ⁻² mbar
Film thickness	≈400 nm

was pressed in to circular pellets of 50 mm diameter and 3 mm thickness using a hydraulic pelletizer with a pressure of 100 bar. The pellets are to be placed in an aluminum plate and used as sputtering cathode. The effects of sputtering power, pressure and substrate temperature for the thermoelectric analysis were investigated and we optimized the sputtering conditions. Argon with 99.9% pure was used as the sputtering gas and the substrate to target distance was optimized to be 80 mm. The vacuum chamber was initially evacuated to a base pressure of 6x10⁻⁶ mbar before the entry of Argon gas in to the chamber. All the films were sputtered at a power of 120 W, substrate temperature of 250⁰C for 45 min to obtain a film thickness of 400 nm at a constant sputtering pressure of 2.5x10⁻² mbar. The pressure was made to be kept constant throughout the sputtering and the quartz crystal monitor provides an situ monitoring of growing thickness of the sputtered film. Table:6.1 shows the optimized deposition parameter for the RF sputtering.

6.3 Results and discussion

6.3.1 EDAX analysis

The EDAX spectrum reveals the composition of each elements present in the sample depending on the energy of X-rays emitted from different shell position. Table: 6.2 represents the atomic, weight % of elements present in the Dy and Ga doped ZnO samples.

As the incorporation of Ga ions in the host lattice increases the diffusion of

Table 6.2: Elemental composition for Dy and Ga doped ZnO

Sample	Element	Weight (%)	Atomic (%)
TF ₁	Zn L	69.03	35.91
	O K	21.38	41.7
TF ₂	Zn L	64.7	30.71
	O K	22.47	43.59
	Dy L	1.02	0.19
TF ₃	Zn L	68.03	33.98
	O K	21.2	43.28
	Dy L	0.802	0.16
	Ga L	1.99	0.93
TF ₄	Zn L	57.81	26.14
	O K	23.78	43.95
	Dy L	0.32	0.06
	Ga L	2.8	1.19
TF ₅	Zn L	49.28	20.15
	O K	26.3	44.79
	Dy L	0.34	0.06
	Ga L	2.52	0.98

Dy ions in the Zn²⁺ site gets reduced since the Ga ion has the smaller ionic

radii compared to Dy ion.

6.3.2 XRD analysis

Fig: 6.1 and Fig: 6.2 represents the X-ray diffraction patterns of the coated thin film. The films corresponding to pure ZnO, 1 wt % Dy doped ZnO and 1,3,5 wt % Ga₂O₃ co doped ZnO was designated as TF₁, TF₂, TF₃, TF₄, TF₅ respectively. The crystalline structure of the films were determined from the X-ray pattern and it possess hexagonal wurtzite structure with P6₃mc space group. It is well matching with that of ICDD card no: 00-005-0664 and ensured the purity of the films formed. The effect of co-doping results for the substitution of tetrahedrally bonded Zn²⁺ cation sites with Dy³⁺ and Ga³⁺ ions. This substitutional replacement induce stress in the lattice and results for a preferred orientation. The peaks corresponding to (002) and (004) plane substantiates the preferred orientation along c axis.

In Fig: 6.3, the shift in (002) plane for the dual doped thin film samples were shown. The shift along the (002) plane ensured the lattice compression along c axis. The lattice parameter c gradually decreases with increasing the Ga content. An enhancement of Seebeck coefficient was expected through lattice compression by the means of modification of DOS.

From the lattice constant, the outplane strain(ϵ) can be determined by the biaxial stress model [9] based on the relation $\epsilon = \frac{c - c_0}{c_0}$ where the c and c₀ represents the lattice constant along the c axis for doped and pure ZnO sample respectively [10]. Table: 6.3 represents the effects of chemical compression along the plane.

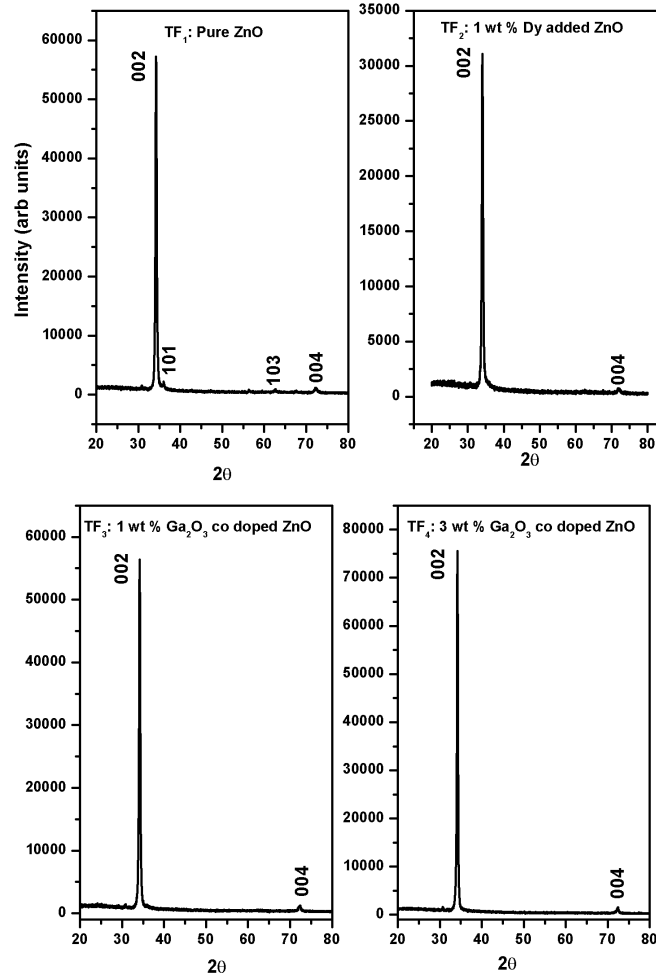


Figure 6.1: X-ray diffraction corresponding to dual doped ZnO thin films.

6.3.3 SEM analysis

SEM technique was employed to analyze the surface morphology of the material synthesized. Fig: 6.4 and 6.5 shows the SEM micrographs corresponding to pure and Dy, Ga doped ZnO samples. The shape of the crystallites changes from polygonal to spherical as we move from pure ZnO to doped samples. The change in the morphology can be explained on the basis of induced strain in the lattice caused by the incorporation of Dy and Ga ion. As the doping concentration increases the size of the crystallites get decrease to form smaller grain boundaries. Size get reduced from 150 nm to

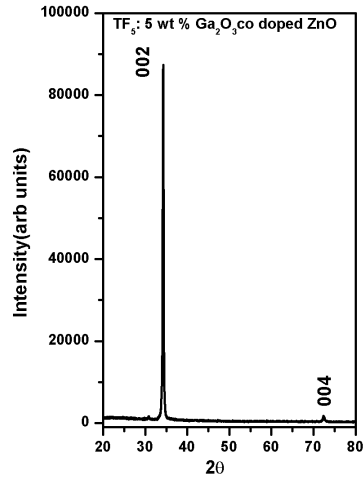


Figure 6.2: X-ray diffraction corresponding to dual doped ZnO thin films.

Table 6.3: Variation of lattice parameter and strain in the lattice by dual doping in ZnO thin films

Sample	Lattice parameter c (\AA)	Strain (%)
TF ₁	5.250	-
TF ₂	5.261	0.29
TF ₃	5.234	0.22
TF ₄	5.243	0.30
TF ₅	5.235	2.30

40 nm. As the particle size gets reduced the grain boundary scattering will be enhanced and results in the deterioration in mobility.

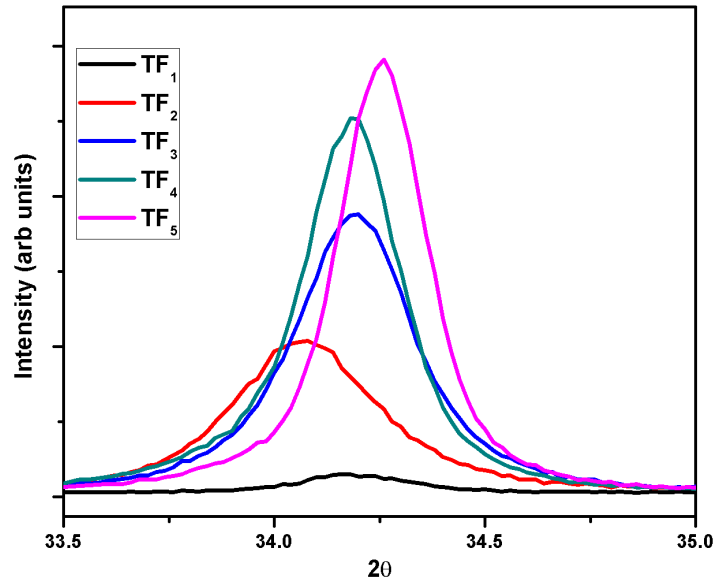


Figure 6.3: Shift in (002) plane for the dual doped ZnO thin films.

6.3.4 AFM analysis

Fig: 6.6 and Fig: 6.7 shows the 3D image of the surface of coated thin film samples. As the doping concentration increases the carrier concentration found to increase which reduces the surface roughness of the thin films. As the stress induced in the lattice increases, the chemical compression causes the polygonal grains to form spherical sized crystallites with a reduction in particle size. The particle size of the crystallites found to decrease from 110 nm to 35 nm which is in agreement with the SEM images. Table: 6.4 depicts the variation in particle size and roughness of the thin films. It was evident that the surface roughness is low for the TF₃ sample compared to TF₄ and TF₅. The decrease in roughness resulted in higher mobility of free charge carriers.

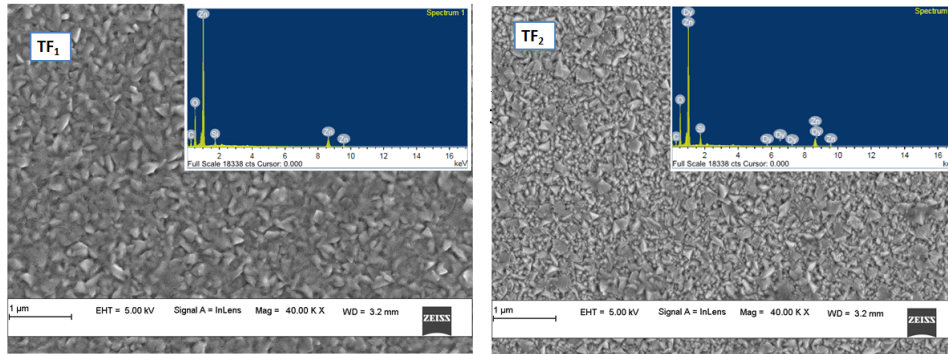


Figure 6.4: SEM micrographs corresponding to pure and Dy doped ZnO samples.

Table 6.4: Determination of particle size and roughness of the coated thin film

Sample	Particle size (nm)	Roughness (nm)
TF ₁	150	80.6
TF ₂	80	42
TF ₃	25	14.9
TF ₄	22	19.1
TF ₅	20	5.98

6.3.5 Optical properties

UV-Visible spectroscopy

Optical transmittance spectra revealed that all the dual doped films exhibited high transmittance above 80% in the visible region as shown in Fig: 6.8.

The band gap determined from Tauc plot corresponding to the doped samples shows a red shift in comparison with the undoped ZnO thin films. The band gap shift can be explained due to the increase in carrier concentration as a result of introduction of Ga and Dy ions. The BM and BGN effects play a crucial role in determining the band gap shift of the doped samples. Fig: 6.9 and 6.10 represent the band gap analysis for the pure and doped ZnO

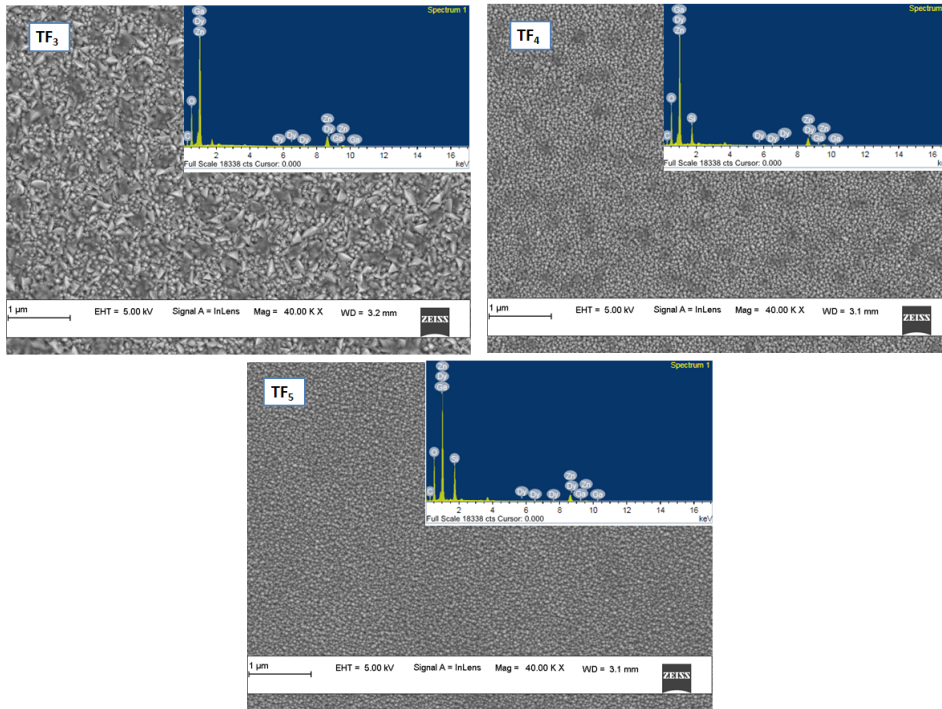


Figure 6.5: SEM micrographs corresponding to Dy and Ga doped ZnO samples.

samples. The optical band gap energy was determined using the Kubelka Munk function [11]. The optical band gap (E_g) is defined as the minimum energy needed to excite an electron from the valence band to the conduction band. In the pure, undoped crystal the optical gap is equal to the energy separation (E_{g0}) between the top of the valence band to the lowest conduction band edge. In a heavily doped n-type semiconductor, the donor electrons occupy states at the bottom of the conduction band. Due to the Fermi exclusion principle, optical transitions can only occur for higher photon energies to make vertical transitions from valence band up to the state with Fermi momentum in the conduction band [12]. This band gap widening due to the blocking of low energy transition can be termed as Burstein-Moss band filling effect. As the electron concentration is above the Mott's critical value [13], the electronic states get modified due to the correlated motion of the charge carriers and their scattering mechanism against ionized impurities. Thus the

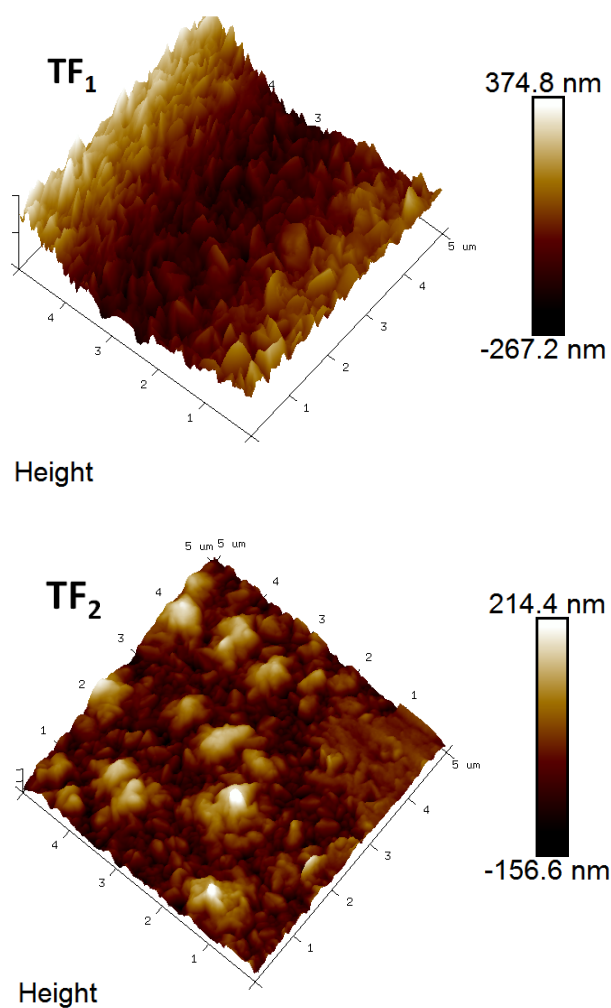


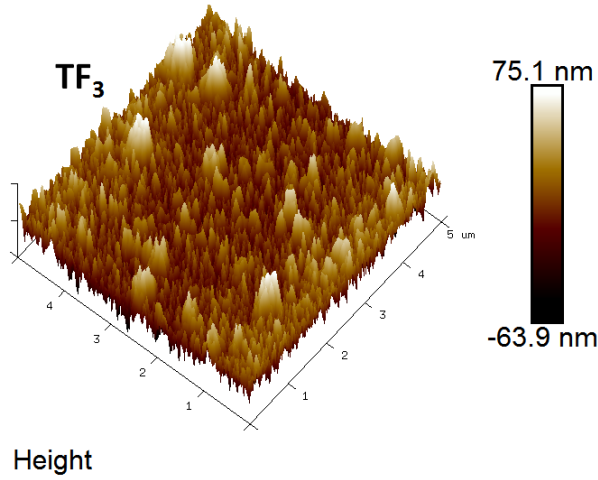
Figure 6.6: AFM 3D images of the pure and Dy doped ZnO thin films.

optical band gap shrinkage occur due to the reconstruction of bands.

6.3.6 Electrical properties

Hall measurement

Room temperature Hall measurement data for the prepared samples were measured and tabulated in table: 6.5. As the doping percentage increases



the carrier concentration found to increase. In doped n-type semiconductor, the lowest state in the conduction band are filled with electron. When the carrier concentration increases above the conduction band density (N_c) the band filling took place. For pure ZnO the conduction band carrier density was found to be $3.68 \times 10^{18} \text{ cm}^{-3}$ [14]. For the doped samples the carrier concentration is found to be greater than N_c and thus BM and BGN effect took place. Due to the band gap shrinkage a pronounced decrement in mobility was not observed which results in the increased electrical conductivity.

Table 6.5: Electrical properties for different Dy and Ga concentration

Sample	Hall concentration (cm^{-3})	Carrier mobility (cm^2/Vs)	Conductivity (S cm^{-1})
T1	-5.22×10^{16}	17.21	0.14
T2	-1.143×10^{20}	2.63	48.06
T3	-1.469×10^{20}	4.02	94.51
T4	-2.64×10^{20}	2.93	123.91
T5	-2.37×10^{20}	4.86	185.01

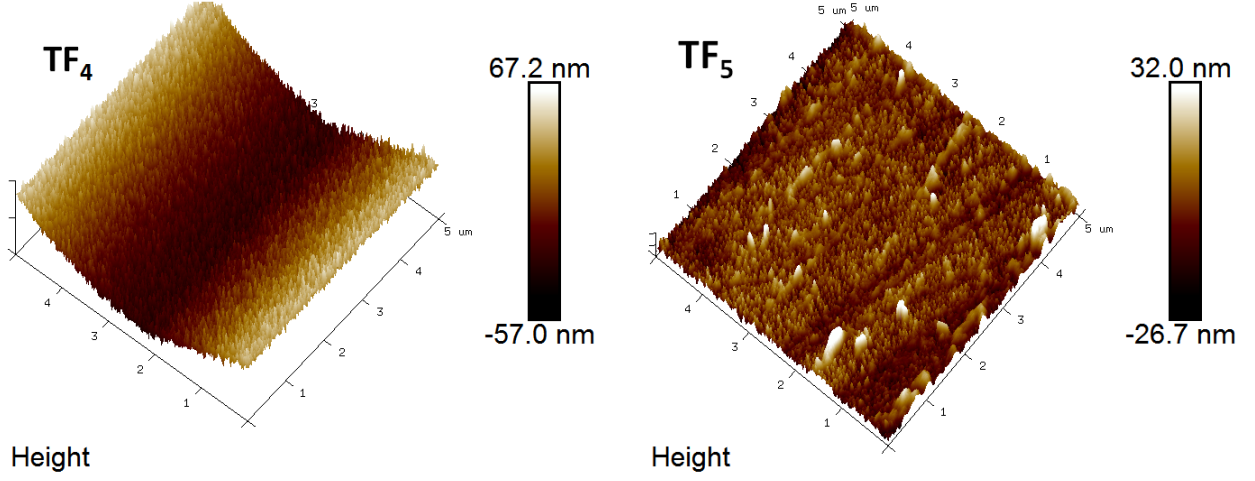


Figure 6.7: AFM 3D images of the dual doped ZnO thin films.

6.3.7 Thermoelectric properties

Thermopower

The measured thermopower, electrical conductivity and the calculated power factor as a function of temperature were plotted and shown in Fig: 6.11, Fig: 6.12, Fig: 6.13. From the optical studies it was found that the doped ZnO samples are degenerate, their band structure get reconstructed. For degenerate semiconductors the Seebeck coefficient can be defined by the Mott's relation:

$$S = \frac{8\pi^2 k_B^2 m^* T}{3eh^2} \left(\frac{\pi}{3n}\right)^{2/3} \quad (6.2)$$

where k_B is the Boltzmann constant, e is the charge of electron, m^* gives the effective mass, h is the Planck constant and n defines the charge carrier concentration. The effective mass m^* in a band is related to the curvature of bands and can be modified by distorting the band. During the BGN effect the inter bands get converge. Each band has its own multivalley and the effective mass for the density of states can be defined as $N_v^{2/3}(m_1 m_2 m_3)^{1/3}$, where N_v is the number of equivalent valley and m_1, m_2, m_3 are inertial masses at each direction. During BGN effect chemical compression took place, which modify

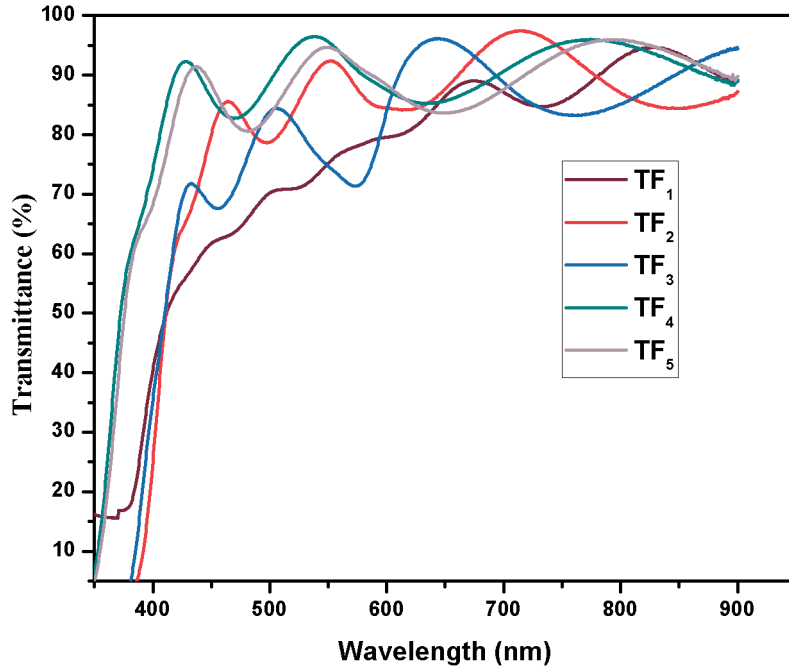


Figure 6.8: Transmittance spectrum of dual doped ZnO.

the density of states and thus interbands having multivalley get converged to form single band. For fixed E_F , multivalley band structure yields the same Fermi velocities with higher density of states. This lead to larger carrier density $n(E)$, along with the same Seebeck coefficient. Thus the thermoelectric power factor gets maximize through the optimization of Seebeck coefficient over the single valley counterpart.

The inter band scattering mechanism will be lower which helps to retain the mobility without much and thereby able to enhance the electrical conductivity. Thus power factor was found to be high for 1 wt% Ga_2O_3 dual doped sample and it was found to be $336\mu\text{W}/\text{mK}^2$ at 423 K.

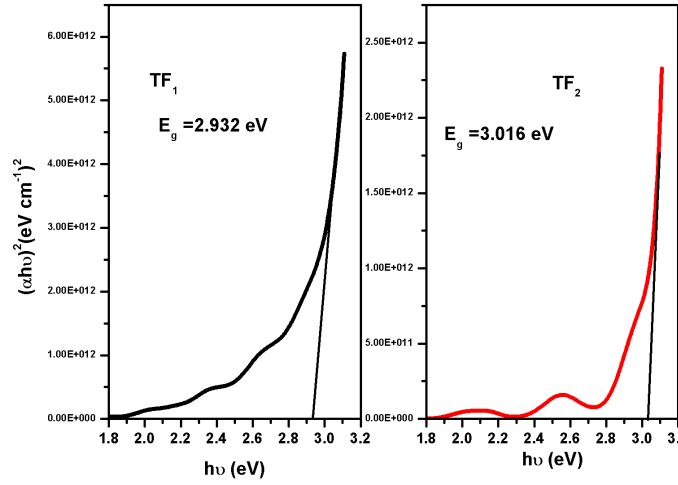


Figure 6.9: Band gap energy for the pure and Dy doped ZnO.

6.4 Conclusions

Co - doping can be considered to be a good criterion for the enhancement of TE properties due to the lower miscibility of ions in the ZnO lattice. XRD results confirms the hexagonal wurtzite structure of the coated thin films using RF magnetron sputtering. Induced strain due to doping causes preferred orientation and a chemical compression along the lattice parameter. Chemical compression of the lattice can be ensured from the shift of (002) plane to higher 2θ . The stress in lattice was determined using the biaxial model. The SEM micrographs substantiates the increased stress in the lattice by the decrement in particle size. The particle size decreases with dual doping and found to be much low for the TF₅ sample. AFM provides the roughness of the sample and substantiate the variation of mobility with roughness. Increased carrier concentration leads to BGN effect and resulted in the convergence of bands. Convergence of bands helps to retain the value of Seebeck coefficient without deteriorating the mobility in the material. Thus TF₃ thin film was found to have a power factor of $336 \mu \text{ W/mK}^2$ at 423 K.

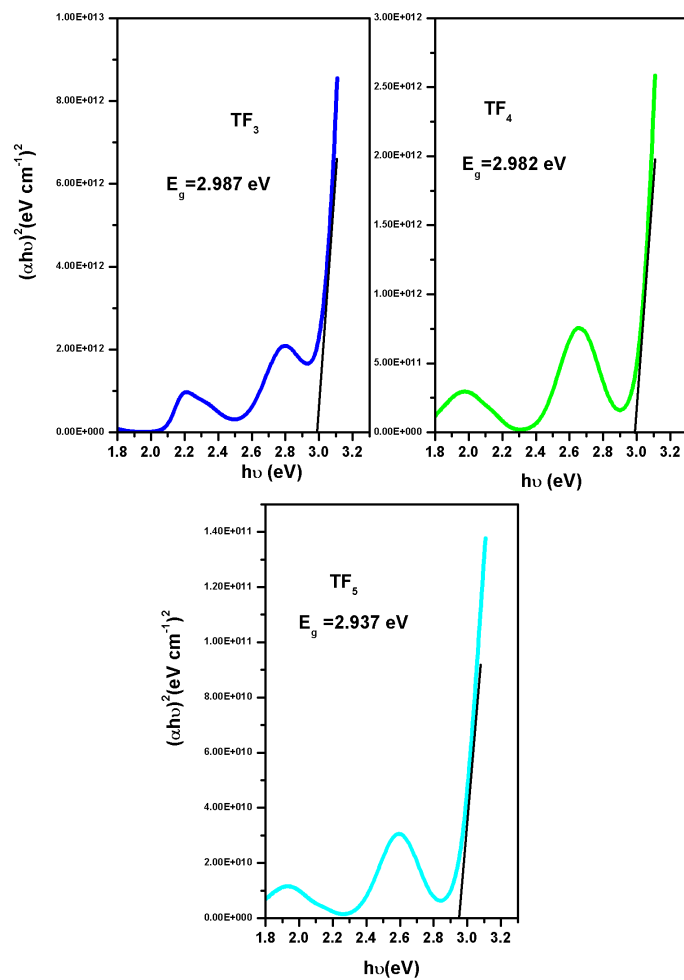


Figure 6.10: Band gap energy for the dual doped ZnO samples.

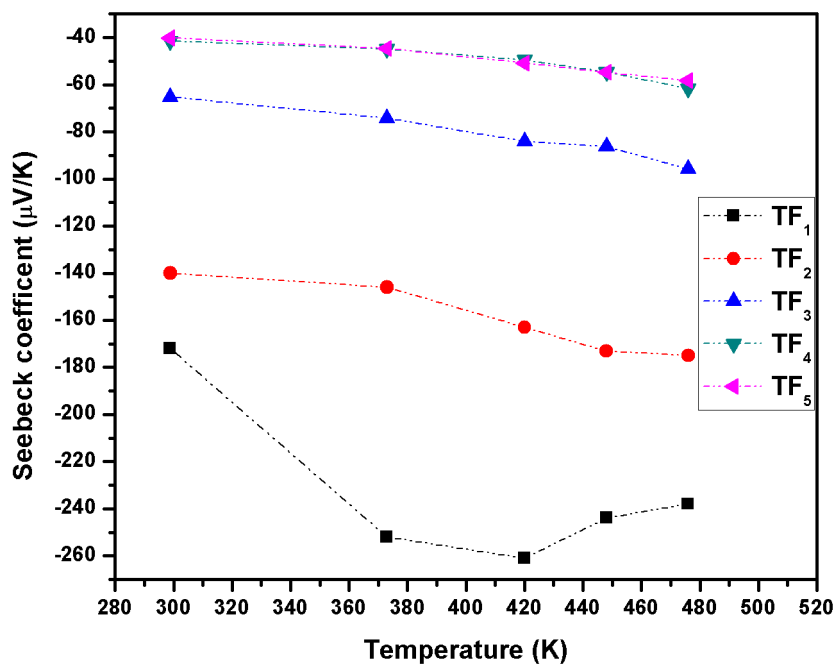


Figure 6.11: Variation of Seebeck coefficient with temperature for the dual doped ZnO.

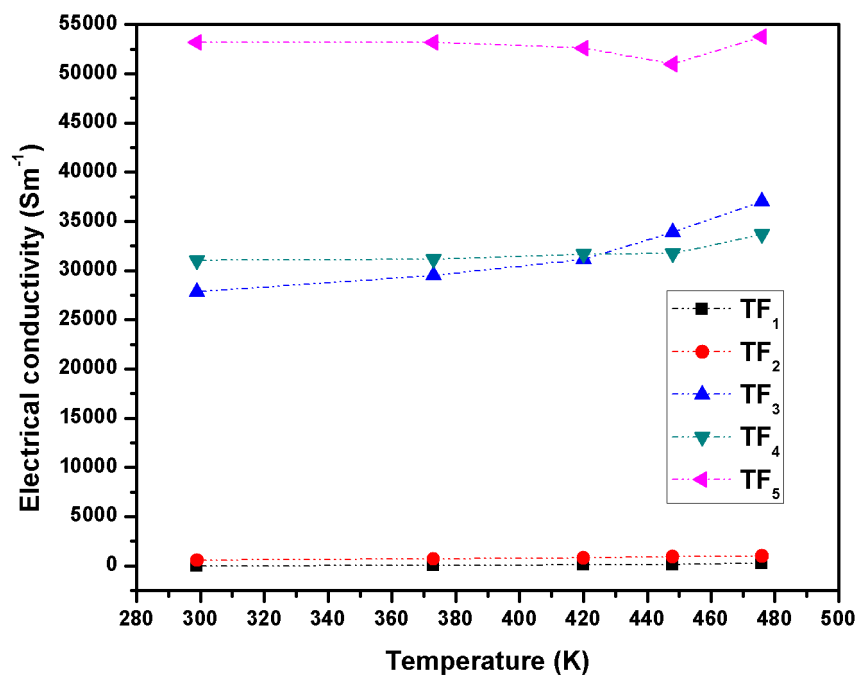


Figure 6.12: Variation of Electrical conductivity with temperature for the dual doped ZnO.

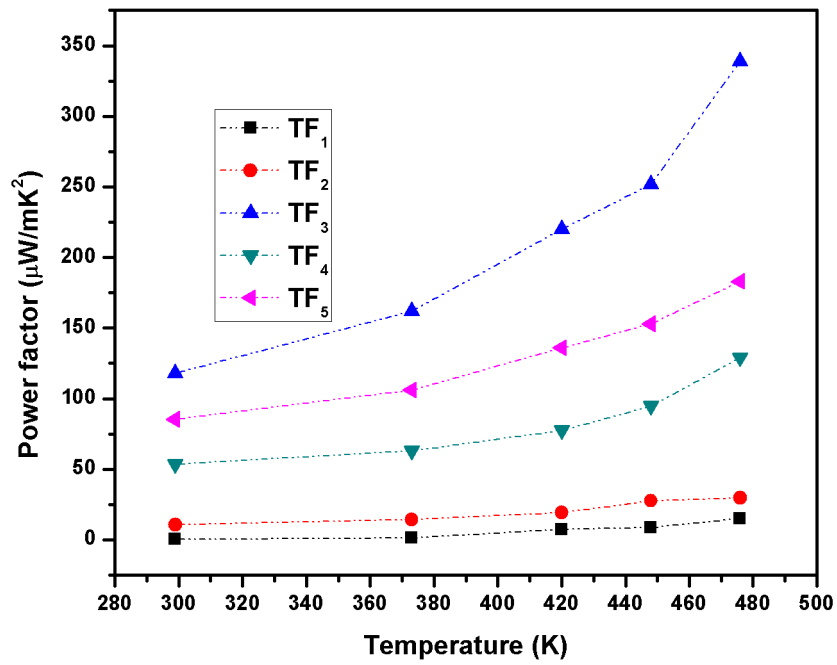


Figure 6.13: Variation of thermoelectric power factor with temperature for the dual doped ZnO.

References

- [1] Y. Nagasawa, A. Hirano, *Appl. Sci.* 8 (2018) 1264.
- [2] M. Grätzel, *J. Sol-Gel Sci. Technol.* 22 (2001) 7–13.
- [3] H. Xue, X. Kong, Z. Liu, C. Liu, J. Zhou, W. Chen, S. Ruan, Q. Xu, *Appl. Phys. Lett.* 90 (2007) 8–11.
- [4] E.N. Hurwitz, M. Asghar, A. Melton, B. Kucukgok, L. Su, M. Oroc, M. Jamil, N. Lu, I.T. Ferguson, *J. Electron. Mater.* 40 (2011) 513–517.
- [5] S. LeBlanc, *Sustain. Mater. Technol.* 1 (2014) 26–35.
- [6] M. Sondergaard, E.D. Bøjesen, K.A. Borup, S. Christensen, M. Christensen, B.B., *Acta Mater.* 61 (2013) 3314–3323.
- [7] P. Jood, R.J. Mehta, Y. Zhang, T. Borca-Tasciuc, S.X. Dou, D.J. Singh, G. Ramanath, *RSC Adv.* 4 (2014) 6363–6368.
- [8] X. Chen, W. Dai, T. Wu, W. Luo, J. Yang, W. Jiang, L. Wang, *Coatings.* 8 (2018) 244.
- [9] H. Hung-Chun Lai, T. Basheer, V. L. Kuznetsov, R. G. Egdell, R. M. Jacobs, M. Pepper, and P. P. Edwards, *Journal of Applied Physics*, 112(2012) 083708.
- [10] B. K. Sharma and N. Khare, *Journal of Physics D: Applied Physics*, 43 (2010) 465402.

- [11] Kubelka P and Munk F 1931 Ein Beitrag zur Optik der Farbanstriche Z. Tech. Phys. 12 1931 593–601.
- [12] J.G. Lu, S. Fujita, T. Kawaharamura, H. Nishinaka, Y. Kamada, Journal of Applied Physics, 101 (2007) 083705.
- [13] P. A. Wolff, Phys. Rev. 126 (1962) 405.
- [14] B. K. Meyer et al., Physica Status Solidi B, 241 (2004) 231.

Chapter 7

General conclusion and Future scope

7.1 Summary of the thesis

Thermoelectric materials are promising candidates for future power generation. As the traditional energy resources are in the path of extinction new energy sources such as TE materials are required for suitable energy management. Along with energy production TE materials are able to manage and conserve energy that are wasted in the form of heat. The waste heat released from automotive exhaust, machinery can be effectively and efficiently used by TE materials for power generation.

Apart from the conventional TE materials, oxide TE materials are quiet important due to its application at high temperature. Oxide TE generators are used in space crafts and satellites where solar energy is inadequate to power the control and communication. Although the conventional TE materials such as Bi_2Te_3 and PbTe possess a ZT value of 1 for application purpose, the efficiency of oxide materials are yet to be increased for practical applications.

The thesis mainly focused on the fabrication of high temperature oxide TE material and different strategies for the enhancement of thermoelectric

figure of merit. Zinc oxide was chosen as the base compound and Dy ions were incorporated in the host lattice and its thermoelectric properties were studied. Strategies such as doping and nanostructuring was done in order to enhance the TE efficiency.

7.1.1 Doping

Doping imparts to be a good criteria for ZT enhancement. Dy^{3+} ions were introduced into the host ZnO lattice with an aim of increasing the carrier concentration and to reduce the lattice thermal conductivity. Solid state reaction method was employed for the study of doping mechanism in microstructures. Atomic concentration of 0.1, 0.2, 0.3 % of Dy ions were incorporated in to the ZnO lattice for the TE enhancement. Structural and TE properties were determined and the results were summarized as:

- * XRD patterns of pure and doped ZnO samples revealed the synthesized samples are single phase and posses a polycrystalline nature. The average crystallite size found to decrease with increase in Dy doping concentration due to the micro strain in the lattice by Dy addition.
- * Raman spectroscopy ensured the Zn-O and O-O bond in the lattice. Presence of $E_1(\text{LO})$ bond ensured the distortion created in the lattice by doping.
- * Microstructure morphology of the samples were revealed by SEM analysis. The powder consist of densely grown crystallites in micron size which offers easy heat conduction through the lattice.
- * Carrier concentration found to increase with doping mechanism. However, the increment of carriers after 0.1 at % of Dy incorporation lead to drastic decrement in mobility which reduce the electrical conductivity.
- * Optical band gap analysis confirmed the doped samples are degenerate by analyzing the widening of optical band gap. Plotting the graph using

the Fritsche model helps to determine the position of Fermi energy level in the conduction band.

- * Transport properties Seebeck coefficient and electrical conductivity were determined from room temperature to 700°C. Thermal conductivity was found to be low for 0.1 at% Dy incorporated sample due to the scattering of electrons at the impurity site (Dy ion) which creates distortion in the lattice.
- * Through doping mechanism we are able to enhance the TE properties of pure ZnO and 0.1 at % Dy incorporated ZnO was found to be a good candidate for TE application since it posses a ZT value of 0.11 at 923 K.

7.1.2 Nanostructuring and Quantum confinement effect

Nanostructured materials are suitable candidates for TE application due to the reduced thermal conductivity. Inhomogeneity and irregularities in nanostructure during its nucleation and growth offers higher tunability to enhance the TE properties. Dy doped nanostructures were fabricated by hydrothermal synthesis which includes the addition of different wt % of DyCl₃(0.5, 0.75, 1) to zinc acetate solution for the reaction to occur. Structural and TE characterisations were performed and thus summarized as:

- * XRD revealed the synthesized Dy doped ZnO samples are phase pure. The shift in peak position confirmed the presence of Dy ion in the sample.
- * Micro Raman analysis confirmed the vibrational modes present. The shift of A₁(TO) mode to lower Raman frequency ensured the incorporation of Dy ion in the host lattice.

- * SEM micrographs revealed the formation of nano grain structure in the host sample which will hinder the easy heat transfer and thereby reduce the lattice thermal conductivity.
- * The presence of porosity and nanograin boundaries in the nanostructured samples act as good scattering sites for phonons. Energy filtering took place at smaller pore radius and the presence of inhomogeneous pores act as suitable scattering sites.
- * Thermal conductivity was found to be low for the Dy doped ZnO nanostructures by the energy filtering mechanism at the pores and at the grain boundaries. 0.5 wt % of Dy doped samples are found to have a highest ZT of 0.048 at 923 K.

Quantum confinement can be achieved by converting the bulk nanostructures in to thin films. The films were fabricated by RF magnetron sputtering with an aim of increasing the power factor to enhance the efficiency of TE materials. As we move from bulk to 2D, the density of states at the Fermi level increases and results in higher power factor as per the Mott's relation. 0.5, 1, 2 wt % of Dy₂O₃ was added to ZnO and the powder was homogenized using ball milling and the home made targets were used as the sputtering cathode. Structural and TE characterisation of these sputtered films were done.

- * XRD peaks revealed the hexagonal wurtzite structure for the thin films. As the Dy concentration increases the planes get preferred oriented along the c axis.
- * SEM micrographs substantiates this preferred orientation with increasing Dy content. As the strain energy increases the crystallite size decreases due to the force in the lattice. Thus the polygonal grains become spherical.
- * AFM analysis points out the increased roughness due to the decrement

in particle size. The electrons or phonons get easily scattered at the smaller grain boundaries and resulted in reduction in mobility.

- * Hall measurements substantiates the decrement in mobility due to the increased carrier concentration
- * The non parabolicity in the band structure can be achieved by band filling which lead to heavier effective mass. Increased effective mass and reduction in mobility lead for the reconstruction of valence band and conduction band.

Reconstruction of the band can be achieved by dual doping in which Ga ions where introduced in to the host Dy doped ZnO matrix. 1,3,5 wt % of Ga₂O₃ was added to 1 wt % Dy doped ZnO sample for the renormalization of bands.

- * XRD results confirmed the phase purity and crystallinity of the films sputtered by RF magnetron sputtering. Along with surface energy, strain energy imparts the plane to preferred orient along c-axis.
- * Chemical compression due to the lattice contraction substantiates the increased density of states and lead for the thermopower enhancement.
- * Due to band reconstruction along with increase in carrier concentration the mobility get preserved along the band. Multibands get converge to form single band without effecting the thermopower over the single valley counter part. Mobility can be preserved by reducing the scattering across inter bands.
- * Enhanced power factor can be obtained for Dy and Ga co-doped samples with a power factor of $336\mu\text{W}/\text{mK}^2$ at 423 K.

In short Dy incorporated ZnO bulk microstructures, bulk nanomaterials and thin films were fabricated and their TE properties were studied. For 0.1 atomic % of Dy addition in micro ZnO the thermoelectric figure of merit was found to be 0.11 at 935 K which is much higher compared to pristine

ZnO. For the 0.5 wt% of Dy addition in nanostructured ZnO a ZT value of 0.05 at 935 K was obtained due to the increment in carrier concentration and reduced thermal conductivity. The lattice thermal conductivity for the doped sample was found to be 6 times lower than pristine ZnO. The decrease in LTC is mainly due to the energy filtering mechanism at the pores. The ZT value for the doped sample was found to be 14 times greater than pure ZnO. The single Kane band model was able to explain the non-parabolicity in band structure due to the increased carrier concentration and the power factor for 0.06 atomic % Dy incorporation was found to be $30\mu\text{ W/mK}^2$. The power factor get doubles when compared with pristine ZnO thin films. As a result of decoupling the effective mass and mobility, bands were reconstructed by doping Ga and Dy ions in host ZnO lattice. The power factor for 0.16 atomic % of Dy and 0.93 atomic % of Ga doped ZnO was found to be $336\mu\text{ W/mK}^2$ which is 23 times greater than pristine ZnO thin films. Thus doping, nanostructuring along with quantum confinement can be adopted for the enhancement of thermoelectric figure of merit. Renormalization of bands also helps to achieve good TE properties at moderate temperature.

7.2 Future scopes

Thermoelectric (TE) materials are the primary requirements for power generation and conservation. Considering the requirement of energy conservation and management TE modules are required for future power generation. Future scope of this work includes:

1. The spin Seebeck effect of the Dy incorporated ZnO materials has to be explored. Since the Dy ion possesses a localized magnetic moment due to the presence of unpaired electrons these materials can be subjected to study spin Seebeck effect.
2. A suitable p type thermoelectric material should be fabricated for the construction of TE modules for device application.

3. Apart from the room temperature Hall measurement, temperature dependent carrier concentration measurements were to be carried out to obtain an idea about the Fermi level changes with temperature.
4. Thermal conductivity of the thin films samples should be done using advanced techniques to determine the figure of merit at higher temperature.
5. Quartz substrates can be used for sputtering oxide materials for the fabrication of TE modules working at higher temperature.